Institute of Thermoelectricity, Academy of Sciences and Ministry of Education and Science of Ukraine

Journal of THERMOELECTRICITY

International Research

Founded in December, 1993

published 6 times a year

No. 6 *2013*

Editorial Board

International Editorial Board

Founders - National Academy of Sciences, Ukraine
Institute of Thermoelectricity of National Academy of Sciences and Ministry of Education and Science of Ukraine

Certificate of state registration № КВ 15496-4068 ПР

Editorial office manager D. Taschuk

Approved for printing by the Academic Council of Institute of Thermoelectricity of the National Academy of Sciences and Ministry of Education and Science, Ukraine

Address of editorial office:
Ukraine, 58002, Chernivtsi, General Post Office, P.O. Box 86.
Phone: +(380-372) 90 31 65.
Fax: +(380-3722) 4 19 17.
E-mail: jt@inst.cv.ua
http://www.jt.inst.cv.ua

Signed for publication 25.12.13. Format 70×108/16. Offset paper №1. Offset printing.
Printer's sheet 11.1. Publisher's signature 9.2. Circulation 400 copies. Order 6.

Printed from the layout original made by "Journal of Thermoelectricity" editorial board
in the printing house of "Bukrek" publishers,
10, Radischev Str., Chernivtsi, 58000, Ukraine

Dear readers of the “Journal of Thermoelectricity”!

Editorial Board is happy to congratulate you on the occasion of the New Year – 2014!

CONTENTS

P.V. Gorsky, S.V. Melnychuk

P.V. Gorsky

Institute of Thermoelectricity of the NAS and MES
Ukraine, 1, Nauky Str., Chernivtsi, 58029, Ukraine

IMPACT OF LAYERED STRUCTURE EFFECTS AND CHARGE ORDERING ON THERMOEMF OF THERMOELECTRIC MATERIALS IN A QUANTIZING MAGNETIC FIELD

S.V. Melnychuk

For the most part, the band structure of materials, thermoelectric included, and the mechanisms of charge carrier scattering in them are studied using de Haas-van Alphen and Shubnikov-de Haas effects. However, it is difficult to separate the oscillations of magnetic susceptibility, the more so, conductivity, from their total magnetic field dependence. At the same time, thermoEMF oscillations can be observed directly. By virtue of this, thermoEMF oscillations in a quantizing magnetic field can be regarded as a complementary measuring tool for the study of the band structure of materials, thermoelectric included, and the mechanisms of charge carrier scattering in them. This paper is concerned with the impact of layered structure effects and charge ordering on thermoEMF of thermoelectric materials in a quantizing magnetic field. Layered structure effects are taken into account in that the energy band spectrum of material is described by the effective mass approximation in layer plane and tight-binding approximation in a direction normal to layers. Quantizing magnetic field and temperature gradient are assumed to be normal to layers. Charge ordering is thought to be interlayer and is regarded as a simple alternation of layers with different electron density. Calculations are based on the Boltzmann kinetic equation in the approximation of constant relaxation time. In the course of calculations it has been shown that the layered structure even in the case of closed Fermi surfaces (FS) results in amplitude increase of thermoEMF oscillations and their phase delay as compared to the effective mass approximation. At the same time, the layered structure effects with closed FS affect scarcely the thermoEMF maximum in a quantizing magnetic field and cause only a slight displacement of this maximum towards weaker magnetic fields. The impact of interlayer charge ordering is manifested in a biperiodic structure of thermoEMF oscillations in quasi-classical magnetic fields and multiple reversal of their polarity in stronger fields. These reversals are synchronized with changes in chemical potential of charge carrier gas in a quantizing magnetic field. When passing into the charge-ordered state with selected parameters of a model of band spectrum of a layered crystal, thermoEMF increases as compared to the disordered state by a factor of 5.9 to 13.5 in quasi-classical magnetic fields and by a factor of 7.6 to 18.4 in stronger quantizing magnetic fields.

Key words: thermoelectric material, thermoEMF, layered structure effects, charge ordering, quantizing magnetic field, chemical potential, relaxation time, oscillations, polarity, reversal.

Introduction

A model of band spectrum of a layered crystal was proposed by R. Fivaz in 1967 [1]. In the framework of this model, the energy levels of a layered crystal in a quantizing magnetic field with induction B normal to layers are determined as:

$$\varepsilon\left(n,k_z\right)=\mu^*B\left(2n+1\right)+\Delta\left(1-\cos ak_z\right). \tag{1}$$

In this formula, n is the Landau level number, k_z is component of quasi-momentum in a direction normal to layers, $\mu^* = \mu_B m_0/m^*$, μ_B is the Bohr magneton, m_0 is free electron mass, m^* is the effective mass of electron in layer plane, Δ is half-width of a miniband describing interlayer motion of electrons, a is the distance between translation-equivalent layers. It is assumed that the layered structure effects manifest themselves only in the case of open Fermi surfaces (FS), i.e. chemical potential of the system ζ referred to the bottom of conduction band meets the condition $\zeta > 2\Delta$, i.e. when the FS is open. However, the purpose of this paper is to demonstrate manifestation of layered structure effects at $\zeta > 2\Delta$ and charge ordering effects by the examples of dependence of thermoEMF of a layered crystal on quantizing magnetic field induction at helium temperatures. The applied significance of this work is that thermoEMF oscillations in a quantizing magnetic field can be used to study the band structure of materials, thermoelectric included, and the mechanisms of charge carrier scattering in them.

Calculation and analysis of the field dependence of thermoEMF of a layered crystal without charge ordering

The use of kinetic Boltzmann equation yields the following general formula for thermoEMF of a layered crystal:

$$\alpha_{zz}\equiv\alpha=\frac{\sum\limits_{\beta}\tau_\beta v_{z\beta}^2\dfrac{\partial f^0\left(\varepsilon_\beta\right)}{\partial T}}{e\sum\limits_{\beta}\tau_\beta v_{z\beta}^2\dfrac{\partial f^0\left(\varepsilon_\beta\right)}{\partial\zeta}}. \tag{2}$$

In this formula, $\beta\equiv(n, k_z)$, T is the absolute temperature, f^0 is Fermi-Dirac distribution, e is electron charge modulus, τ_β is relaxation time, $v_{z\beta}$ is longitudinal electron velocity, the rest of notation has been explained above.

Calculation of thermoEMF of a layered crystal with a band spectrum (1) and constant relaxation time yields the following formula:

$$\alpha_{zz}=\frac{\pi\alpha_0 A}{B+C}. \tag{3}$$

In this formula, $\alpha_0 = k/e$, k is the Boltzmann constant, and the dimensionless coefficients A, B, C are determined as below:

$$\begin{aligned}A=\sum_{l=1}^{\infty}(-1)^{l-1}f_l^{th}\Bigg\{\sin\left(\pi l\frac{\zeta-\Delta}{\mu^*B}\right)\Bigg[\left(C_0-C_2\right)J_0\left(\frac{\pi l\Delta}{\mu^*B}\right)+\\ +\sum_{r=1}^{\infty}(-1)^r\left(2C_{2r}-C_{2r+2}-C_{2r-2}\right)J_{2r}\left(\frac{\pi l\Delta}{\mu^*B}\right)\Bigg]+\cos\left(\pi l\frac{\zeta-\Delta}{\mu^*B}\right)\times\\ \times\sum_{r=0}^{\infty}(-1)^r\left(2C_{2r+1}-C_{2r+3}-C_{|2r-1|}\right)J_{2r+1}\left(\frac{\pi l\Delta}{\mu^*B}\right)\Bigg\}.\end{aligned} \tag{4}$$

$$B=0.5\left(C_0-C_2\right). \tag{5}$$

$$C=\sum_{l=1}^{\infty}(-1)^l f_l^{\sigma}\left\{\cos\left(\pi l\frac{\zeta-\Delta}{\mu^* B}\right)\left[(C_0-C_2)J_0\left(\frac{\pi l\Delta}{\mu^* B}\right)+\right.\right.$$
$$+\sum_{r=1}^{\infty}(-1)^r\left(2C_{2r}-C_{2r+2}-C_{2r-2}\right)J_{2r}\left(\frac{\pi l\Delta}{\mu^* B}\right)\Big]-\sin\left(\pi l\frac{\zeta-\Delta}{\mu^* B}\right)\times \tag{6}$$
$$\left.\left.\times\sum_{r=0}^{\infty}(-1)^r\left(2C_{2r+1}-C_{2r+3}-C_{|2r-1|}\right)J_{2r+1}\left(\frac{\pi l\Delta}{\mu^* B}\right)\right\}.$$

In these formulae, $J_n(x)$ are the Bessel functions of the 1-st kind, n-th order and real argument and modulating coefficients are determined as:

$$C_0=\arccos\left(1-\frac{\zeta-\mu^* B}{\Delta}\right), \tag{7}$$

$$C_m=\frac{\sin mC_0}{m}\ \text{at}\ m\neq 0. \tag{8}$$

Subtraction of $\mu^* B$ from ζ explicitly takes into account the fact of charge carrier condensation at the bottom of a subband with the number $n = 0$ in the ultraquantum limit.

Besides:

$$f_l^{th}=\left[\mathrm{sh}\left(\pi^2 lkT/\mu^* B\right)\right]^{-1}\left[1-\left(\pi^2 lkT/\mu^* B\right)\mathrm{cth}\left(\pi^2 lkT/\mu^* B\right)\right]. \tag{9}$$

$$f_l^{\sigma}=\left(\pi^2 lkT/\mu^* B\right)\left[\mathrm{sh}\left(\pi^2 lkT/\mu^* B\right)\right]^{-1}. \tag{10}$$

In these formulae, sh(x) and cth(x) are hyperbolic sinus and cotangent, respectively. In the effective mass approximation the coefficients A, B, C are determined as follows:

$$A=\sum_{l=1}^{\infty}(-1)^{l-1} f_l^{th}\left\{\frac{\mu^* B}{\pi l\Delta}\sqrt{\frac{2\left(\zeta-\mu^* B\right)}{\Delta}}-\frac{1}{\pi}\left(\frac{\mu^* B}{l\Delta}\right)^{3/2}\left[\cos\left(\frac{\pi l\zeta}{\mu^* B}\right)\times\right.\right.$$
$$\left.\left.\times C\left(\sqrt{2l\left(\frac{\zeta}{\mu^* B}-1\right)}\right)+\sin\left(\frac{\pi l\zeta}{\mu^* B}\right)S\left(\sqrt{2l\left(\frac{\zeta}{\mu^* B}-1\right)}\right)\right]\right\}. \tag{11}$$

$$B=\frac{1}{6}\left[2\left(\frac{\zeta-\mu^* B}{\Delta}\right)\right]^{3/2}. \tag{12}$$

$$C=\sum_{l=1}^{\infty}(-1)^l\frac{f_l^{\sigma}}{\pi}\left(\frac{\mu^* B}{l\Delta}\right)^{3/2}\left[\sin\left(\frac{\pi l\zeta}{\mu^* B}\right)\times C\left(\sqrt{2l\left(\frac{\zeta}{\mu^* B}-1\right)}\right)-\cos\left(\frac{\pi l\zeta}{\mu^* B}\right)S\left(\sqrt{2l\left(\frac{\zeta}{\mu^* B}-1\right)}\right)\right]. \tag{13}$$

In formulas (11) and (13) $C(x)$ and $S(x)$ – cosine- and sine- Fresnel integrals, respectively.

Equations defining the chemical potential of electron gas in a quantizing magnetic field for a real layered crystal and in the effective mass approximation are given in [2]. The results of calculation of thermoEMF of a layered crystal in a quantizing magnetic field are presented in Figs. 1 and 2.

From the plots it is apparent that in quasi-classical magnetic fields the layered structure effects are manifested in phase delay and increase of a relative contribution of thermoEMF oscillations with a

reduction of its value as a whole. In stronger magnetic fields there is an optimal range of these fields wherein the layered structure effects are most pronounced, but thermoEMF maximum is affected scarcely by these effects that only cause its slight displacement towards weaker magnetic fields.

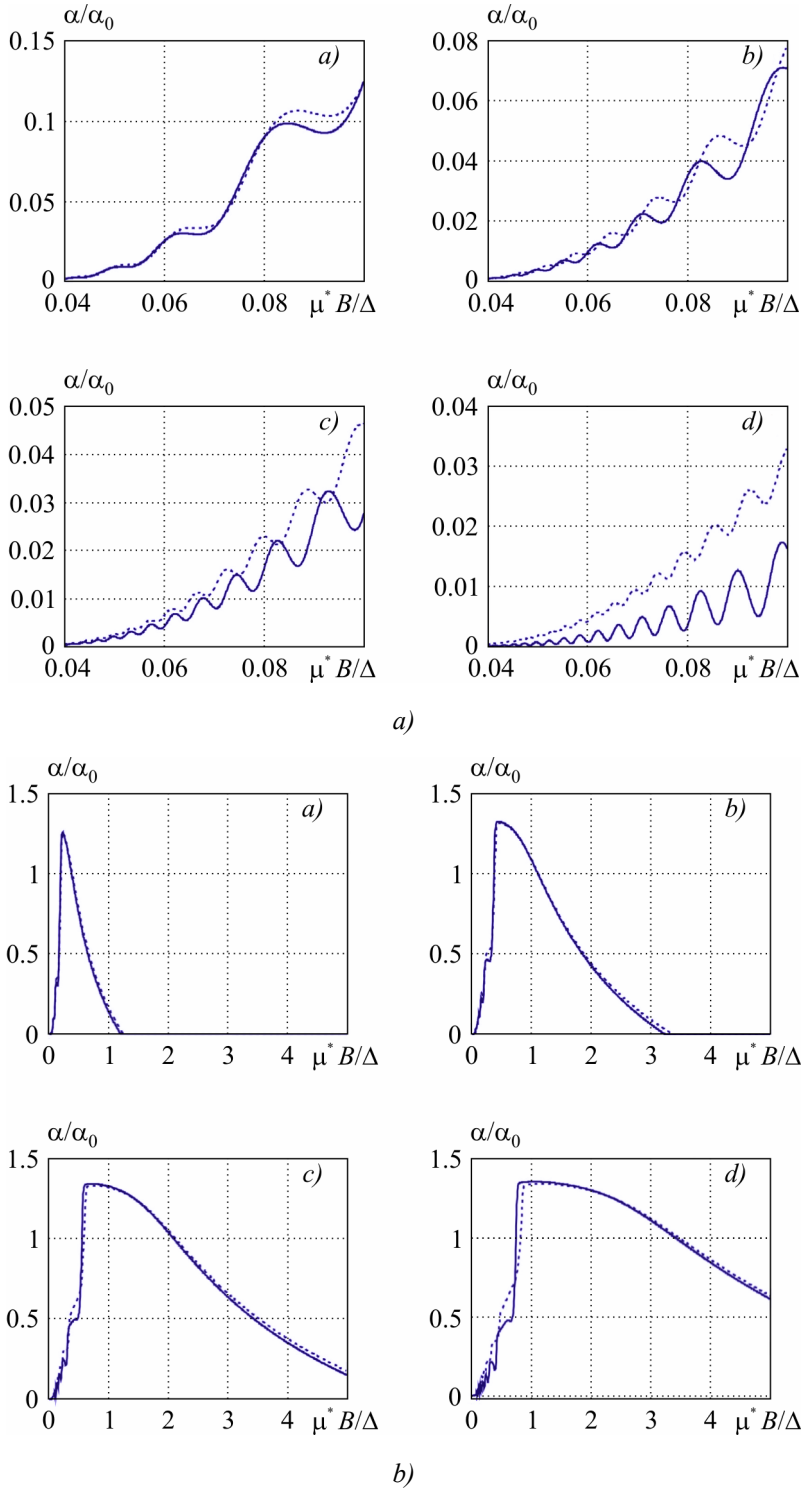

Fig. 1. Field dependences of thermoEMF of a layered crystal: a) in quasi-classical approximation, b) in a wide range of magnetic fields at $kT/\Delta = 0.03$. Solid curves correspond to a real layered crystal, dashed curves – to the effective mass approximation. In the plots, the Latin letter a corresponds to the ratio ζ_0/Δ equal to 0.5, b – 1, c – 1.5, d – 2.

Impact of charge ordering on thermoEMF of layered crystals in a quantizing magnetic field

If charge ordering in a layered crystal is considered as a simple alternation of layers more or less filled with electrons, then the coefficients A, B, C in the approximation of constant relaxation time are determined as follows [3]:

$$A = \sum_{l=1}^{\infty} (-1)^l f_l^{th} \int_{-(\gamma-b)}^{\sqrt{w^2\delta^2+1}} \left| y^{-1} \right| \sqrt{\left(1 + w^2\delta^2 - y^2\right)\left(y^2 - w^2\delta^2\right)} \sin\left[\pi l b^{-1}(\gamma - y)\right] dy, \tag{14}$$

$$B = 0.5 \int_{-(\gamma-b)}^{\sqrt{w^2\delta^2+1}} \left| y^{-1} \right| \sqrt{\left(1 + w^2\delta^2 - y^2\right)\left(y^2 - w^2\delta^2\right)} dy, \tag{15}$$

$$C = \sum_{l=1}^{\infty} (-1)^l f_l^{\sigma} \int_{-(\gamma-b)}^{\sqrt{w^2\delta^2+1}} \left| y^{-1} \right| \sqrt{\left(1 + w^2\delta^2 - y^2\right)\left(y^2 - w^2\delta^2\right)} \cos\left[\pi l b^{-1}(\gamma - y)\right] dy. \tag{16}$$

In these formulae, $\gamma = \zeta / \Delta$, $b = \mu^* B / \Delta$, $w = W_0 / \Delta$. Moreover, δ is order parameter varying in the range from 0 to 1, W_0 is the effective interaction that results in charge ordering. With such ordering, charge carrier motion in the direction normal to layers is described by the formula:

$$W(k_z) = \pm\sqrt{W_0^2\delta^2 + \Delta^2 \cos^2 ak_z}. \tag{17}$$

Equations defining the field dependences of chemical potential and the order parameter are given in [4]. The results of calculating thermoEMF of a charge-ordered layered crystal are depicted in Fig. 2.

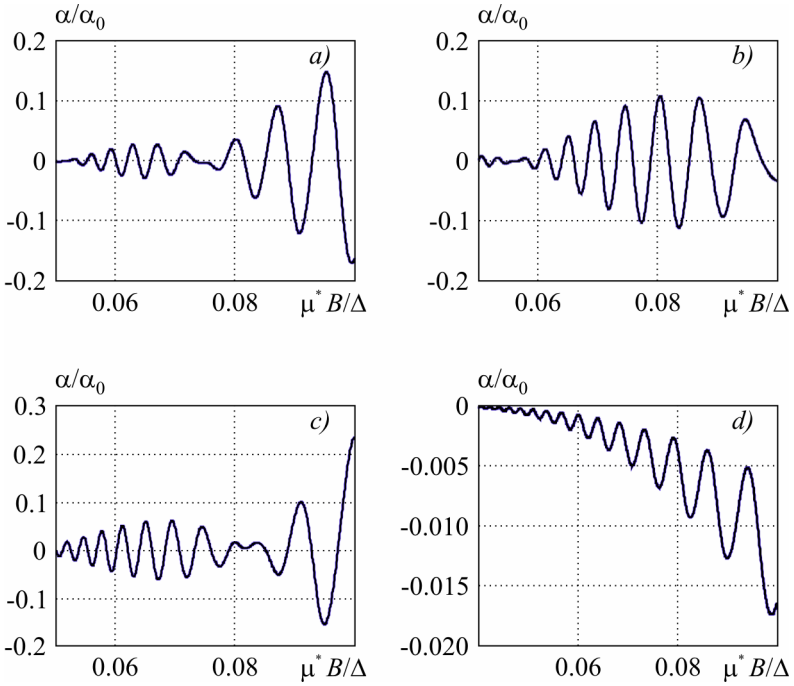

a)

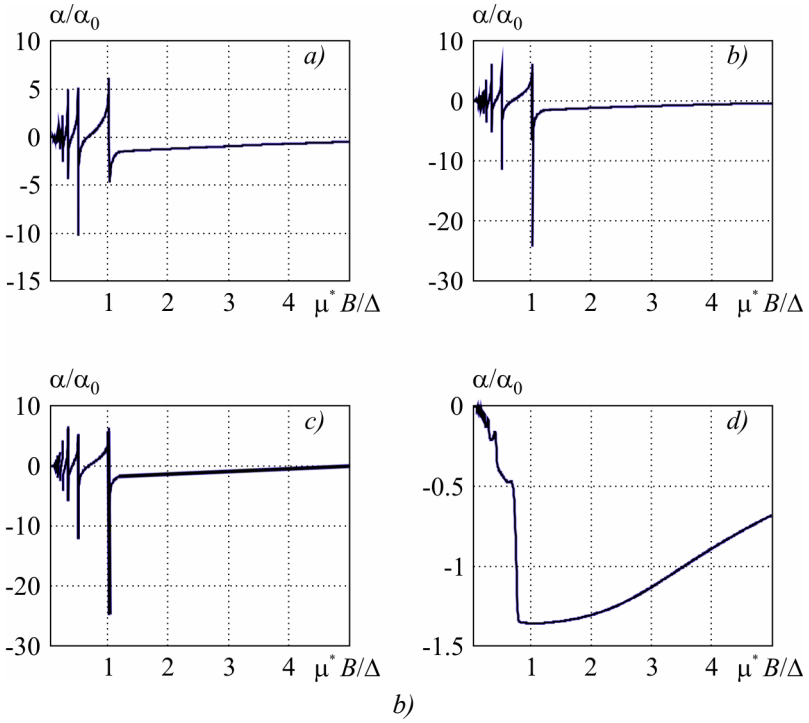

Fig. 2. Field dependences of thermoEMF of a layered charge-ordered crystal: a) in quasi-classical magnetic fields; b) in a wide range of magnetic fields. In the plots the Latin letter a corresponds to the ratio W_0 / ζ_{02D} equal to 1.5, b – 2, c – 2.5, d – 0 (disordered state).

From the plots it is seen that charge ordering is manifested in a biperiodic structure of oscillations in quasi-classical magnetic fields, their polarity reversal in stronger magnetic fields and a drastic drop of thermoEMF value after the point of a topological transition matched by the last polarity reversal.

Conclusions and recommendations

1. The layered structure effects are manifested in the reduction of relative contribution and phase delay of thermoEMF oscillations in quasi-classical magnetic fields, the existence of optimal range where they are most pronounced in the intermediate magnetic fields and a slight displacement of thermoEMF maximum toward weaker magnetic fields.
2. Charge ordering is manifested in the origination of a biperiodic structure of oscillations, thermoEMF polarity reversal in strong magnetic fields and a drastic drop of thermoEMF value after the point of a topological transition from an open FS into a closed one.

References

1. R.F. Fivaz, Band Spectrum of Layered Crystals, *J. Phys. Chem. Sol.* **28**, 839 – 843 (1967).
2. P.V. Gorsky, Power Factor for Layered Thermoelectric Materials with Closed Fermi Surface in Quantizing Magnetic Field, *Ukr. J. Phys.* **58**, 371 – 377 (2013).
3. P.V. Gorsky, Effect of Charge Ordering on the ThermoEMF of Layered Crystals in a Quantizing Magnetic Field, *Journal of Thermoelectricity* **4**, 14 – 24 (2012).
4. P.V. Gorsky, Longitudinal Electric Conductivity of Layered Charge-Ordered Crystals in a Strong Quantizing Magnetic Field, *Semiconductors* **45**, 928 – 935 (2011).

Submitted 25.09.2013.

E.I. Rogacheva[1], A.N. Doroshenko[1], V.I. Pinegin[1], M.S. Dresselhaus[2]

[1]National Technical University "Kharkov Polytechnic Institute",
21, Frunze Str., Kharkov, 61002, Ukraine;
[2]Massachusetts Institute of Technology, 77, Massachusetts Ave.,
Cambridge, MA 02139, USA

ELECTRONIC PHASE TRANSITIONS AND STRUCTURAL INSTABILITY IN $Bi_{1-x}Sb_x$ SOLID SOLUTIONS

An X-ray study of $Bi_{1-x}Sb_x$ alloys in the concentration range x = 0 – 0.1 was carried out. It was established that up to Sb concentration x ~ 0.02 the unit cell parameters (a, c) decrease linearly with increasing concentration, and the diffraction linewidth increases. In the concentration interval of x = 0.025 – 0.1 the a(x) and c(x) curves noticeably deviate from the Vegard straight line, with maximum deviations corresponding to the compositions at which the transition to a gapless state and the energy band inversion occurs (x = 0.03 – 0.035) and the semimetal-semiconductor transition (x = 0.06 – 0.07) takes place. In the indicated concentration regions, and also in the interval x = 0.005 – 0.01, a decrease in the X-ray diffraction line width is observed. It is suggested that the structural instability occurring in these special concentration ranges in $Bi_{1-x}Sb_x$ solid solutions is connected with changes in the electron spectrum under the percolation transition, the transition into a gapless state and band inversion and under a semimetal – semiconductor transition.

Key words: *Bi-Sb* solid solutions, composition, crystal structure, unit cell parameter, *X*-ray line width, electronic transition.

Introduction

Recently, bulk crystals of the $Bi_{1-x}Sb_x$ solid solutions and low-dimensional structures based on them have attracted much attention as promising thermoelectric and magnetoelectric materials for refrigeration devices at temperatures below ~ 200 K [1]. On the other hand, these solid solutions are interesting materials for solid state physics, because they have extremely low effective electron masses and an anomalously high charge carrier mobility and mean free-path [2-4]. Recently, interest in investigating the transport properties of $Bi_{1-x}Sb_x$ crystals and thin films has also grown sharply due to the prediction [5, 6] and subsequent experimental observation [7] of the special properties characteristic of topological insulators [5, 8] in $Bi_{1-x}Sb_x$ crystals.

Bi and *Sb* semimetal crystals are electronic analogs with a similar type of chemical bond and they crystallize under normal conditions in a similar structure (arsenic-type), which is described using not only by a rhombohedral structure but also by a hexagonal and face-centered pseudocubic lattice [9]. *Bi* and *Sb* form between themselves a continuous series of solid solutions [9].

The electronic structure of $Bi_{1-x}Sb_x$ solid solutions has been studied in a great number of works (e.g., [10-15]). In *Bi*, the *T*-valence band overlaps with the L_a conduction band at the *T*-point of the Brillouin zone. At the *L*-point, there is another valence band L_s, separated from the conduction band by a small gap (E_g). At present, it is known that with increasing *Sb* concentration, the energy difference between the L_a and L_s bands decreases, and at a certain critical concentration ($x = 0.02 – 0.04$

according to the data of different authors), a gapless state (GLS) is realized and band inversion occurs [10-15]. Then the energy difference between the L_a and L_s bands increases again. On the other hand, with increasing *Sb* concentration x, the T-valence band decreases in energy, and its overlap with bands at the L and T points (ΔE) vanishes for $0.06 \le x \le 0.07$, resulting in the semimetal-semiconductor (SMSC) transition. Due to the possibility of a radical change in the $Bi_{1-x}Sb_x$ solid solutions band structure under changing composition for this composition range, these materials are very convenient for studying peculiarities of the electronic phase transitions (EPTs) in $Bi_{1-x}Sb_x$.

In [16, 17], we reported the observation of anomalies in the isotherms of the galvanomagnetic and thermoelectric properties in $Bi_{1-x}Sb_x$ solid solutions in the concentration ranges 0.5 – 1.5, 2.5 – 3.5 and 6 – 8 at.% *Sb*. These peculiarities were attributed to critical phenomena accompanying the transition of a percolation type from a dilute to a concentrated solid solution, the transition to a GLS, and to the SMSC transition, respectively. Taking into account that a strong electron-phonon interaction takes place [18-20] in $Bi_{1-x}Sb_x$ solid solutions, it can be expected that a change in the electron spectrum will result in a change in the phonon spectrum, which in turn will lead to the appearance of peculiarities in the isotherms of various physical properties determined by the lattice subsystem of the crystal. In [20], for a $Bi_{0.97}Sb_{0.03}$ solid solution doped with an acceptor impurity, an increase in the high-frequency dielectric constant ε_∞ amounting to 30 % of the dielectric constant for bismuth ($\varepsilon_\infty = 100$) was observed. The increase in high-frequency dielectric constant provides evidence for an increase in the polarizability of the valence electrons in $Bi_{0.97}Sb_{0.03}$ crystals and results from the anomalously small values of the L-point energy gap width at this composition. Due to the high polarizability of these valence electrons, the electron and lattice (phonon) properties appear to be strongly interdependent. This, in turn, causes a softening of the transverse phonon modes and an increase in the rigidity of the longitudinal modes of the optical oscillations of the crystal lattice and makes a phase transition quite possible. However, up to now, the direct observation of the suggested structural phase transitions in the $Bi_{1-x}Sb_x$ solid solutions has not been yet reported.

In this connection there arises a question, whether EPTs are accompanied by structural changes in the crystal lattice, caused by atom redistributions aimed at attaining configurations corresponding to a minimum in the potential energy.

The dependences of the unit cell parameters on the composition of the $Bi_{1-x}Sb_x$ alloys were studied in a number of works [17, 21-33]. Most authors reported a nearly linear change in the a and c parameters (of a hexagonal lattice) under changing composition over the entire concentration interval, although some authors [10, 23, 25, 26, 28] pointed out a deviation of these dependences (mainly the $c(x)$ ones) from Vegard's straight-line law. For example, in [10] a deviation from the linear dependence for the unit cell parameter c was observed for monocrystalline $Bi_{1-x}Sb_x$ alloys in the concentration range $x = 0 – 0.08$. However, according to the authors of [24], such a non-linear change was caused by the alloy inhomogeneity connected with the insufficient time of annealing (24 hours at 523 K). The authors of [31], who measured unit cell parameters along the monocrystalline ingot grown by the Chochralsky method with the concentration gradient $x = 0 – 0.18$, registered an anomalous increase in unit cell parameter c in the ingot section corresponding to $x \sim 0.07 – 0.09$. The authors, however, attributed the anomalous increase to the specificity of the growth technology.

In [17, 33], where $Bi_{1-x}Sb_x$ solid solutions in the composition ranges $x = 0 – 0.05$ [17] and $x = 0 – 0.08$ [33], annealed at 520 K for 100 [17] or 200 [33] hours were studied, it was shown that the unit cell parameters *a* and *c* decrease almost linearly as the *Sb* concentration increases up to $x \sim 0.02$. After that a deviation from the linear dependence, which becomes most significant near $x = 0.03$, is

observed. It was suggested that a transition to a GLS and an inversion of the valence and conduction band symmetries or they are accompanied by structural changes. However, it should have been taken into account that the duration of annealing (100 – 200 hours) could turn out to be insufficient for a complete homogenization of the samples. To rule out the influence of that technological factor, it was necessary to carry out *X*-Ray diffraction studies using samples annealed for a longer time.

The goal of the present work is performing detailed *X*-Ray studies of the $Bi_{1-x}Sb_x$ alloys after long-term annealing with a view to revealing structural instabilities connected with the existence of the EPTs.

The results of the present study have shown that GLS and SMSC transitions are accompanied by structural changes corresponding to an anomalous increase in the unit cell parameters and a decrease in the *X*-Ray diffraction linewidth (XRDL).

Experimental

Polycrystalline samples of $Bi_{1-x}Sb_x$ in the concentration range $x = 0 – 0.1$ were synthesized from high-purity elements (not less than 99.999 %) in quartz ampoules evacuated down to 10^{-3} Pa at $T = (1020 \pm 10)$ K, keeping the melt at this temperature for 5 – 6 hours. After the synthesis, the samples were quenched in air, then annealed for 720 hours at (520 ± 5) K and cooled down inside the off-powered furnace. All samples were prepared simultaneously to ensure the identity of the preparation conditions. The results of microstructural analysis showed that all prepared polycrystalline $Bi_{1-x}Sb_x$ alloys were single-phased with an average grain size $d \approx 300$ μm. The chemical composition and homogeneity of the samples were controlled using electronic microprobe analysis (JSM-6390 LV, Jeol Ltd.), *X*-Ray photoelectronic spectroscopy using a scanning electron microscope (XPS-800 Kratos), and an *X*-ray fluorescent method. It was shown that the chemical compositions of the samples corresponded to what was intended with an accuracy of not less than 5 % (relative to one another), and the degree of the sample homogeneity was satisfactory. Additional control of the sample homogeneity, which was confirmed using the methods of measuring microhardness and microthermopower, demonstrated that the dispersion of the values of the indicated parameters within the sample did not exceed the error of their measurement.

X-ray powder diffraction studies were carried out with a DRON-2 diffractometer using *Ni* filtered *Cu* K_α-radiation. The unit cell parameters *a* and *c* were determined after processing the diffraction profiles, which included smoothing, separation of the background from the reflection profiles, separation of overlapping peaks and the precise determination of their maxima location. The error in the determination of *a* and *c* amounted to $\Delta a = 2 \cdot 10^{-4}$ nm and $\Delta c = 4\ 10^{-4}$ nm. The obtained values of the unit cell parameters ($a = 0.4546$ nm and $c = 1.1853$ nm) for pure *Bi* were in good agreement with those reported in other works [22-25].

Results and discussion

In Fig 1 *a*, as an example, fragments of *X*-ray diffraction patterns in the vicinity of the (0 1 14) diffraction peaks are presented for the samples with different *x* values. In Fig. 1 *b*, the dependences of the unit cell parameters a and c on the $Bi_{1-x}Sb_x$ solid solution composition, are presented. As is seen in Fig. 1 *b*, an increase in *Sb* concentration up to $x = 0.02$ leads to a practically linear decrease in both *a* and *c*, in accordance with Vegard's law. However, under further increase in *x*, in two concentration intervals: $x = 0.025 – 0.035$ and $x = 0.05 – 0.07$, the $a(x)$ and $c(x)$ curves exhibit a distinct deviation from Vegard's straight line behavior.

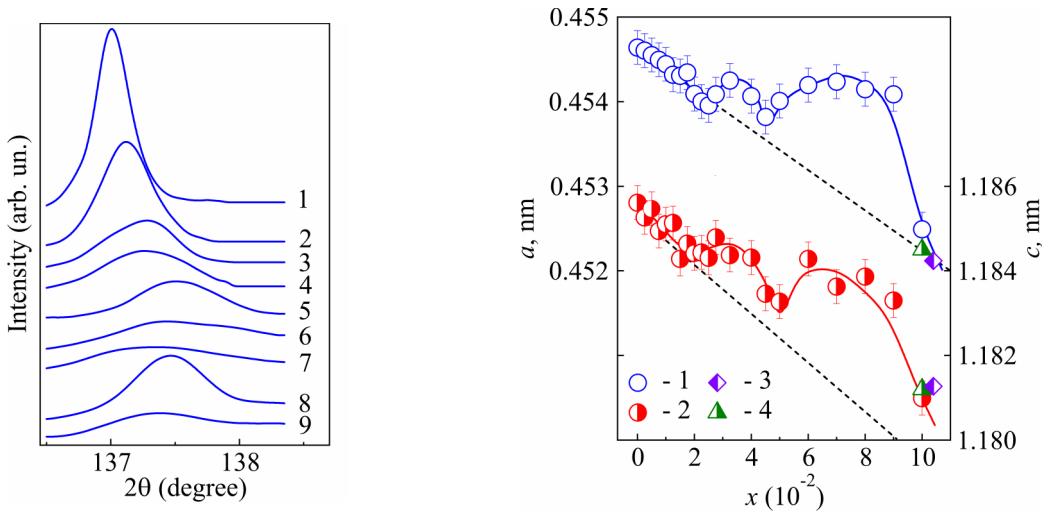

Fig. 1. Sections of the diffractograms plotting X-ray intensity vs 2θ near the (0 1 14) X-ray diffraction peaks (a), and the lattice parameters a and c (b) of the $Bi_{1-x}Sb_x$ solid solutions vs Sb concentration x: (a): x = 0 (1); 0.01 (2); 0.02 (3); 0.0325 (4); 0.045 (5); 0.05 (6); 0.06 (7); 0.07 (8); 0.08 (9). (b): 1 – a; 2 – c; 3 – data from reference [25]; 4 – data from reference [28]; line – Vegard's law.

In Fig. 2, the concentration dependences of the XRDL for the (1 4 6) reflections are presented as $\Delta B/B_0$ vs x. It is seen that the dependence has a sophisticated nonmonotonic character: in the concentration ranges $x = 0.005 – 0.01$, $x = 0.025 – 0.03$ and $x = 0.05 – 0.07$, a decrease in XRDL is observed.

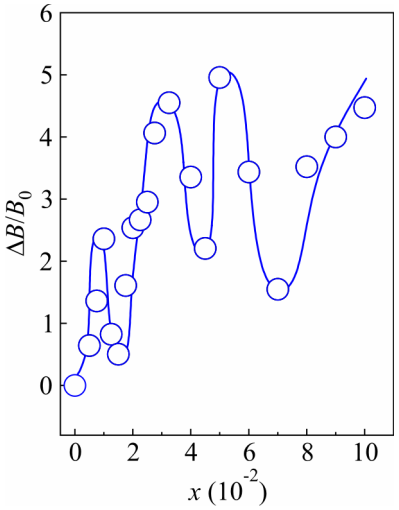

Fig. 2. The dependence of a relative change in the (0 1 14) X-ray diffraction linewidth $\Delta B/B_0$ on the Sb concentration x in the $Bi_{1-x}Sb_x$ solid solutions.

The existence of the concentration anomalies in the $a(x)$ and $c(x)$ curves provides evidence in favor of structural changes in the crystal lattice. Taking into consideration the character of these changes in the energy band structure in the $Bi_{1-x}Sb_x$ solid solutions, one can suggest that such structural changes are connected with both the transition to a GLS and the energy band inversion at the L-point of the Brillouin zone [3, 4] ($x = 0.025 – 0.035$), and with a SMSC transition ($x = 0.05 – 0.07$).

It is known that among the main factors that cause a broadening of the X-ray diffraction lines are the fluctuations of the interatomic distances due to microstresses and to the small size of the coherent scattering regions [34]. In homogeneous solid solutions, a broadening of the X-ray diffraction

lines can be caused by the disorder in the distribution of atoms of different types and the static displacement of atoms surrounding an impurity atom relative to their positions in the ideal crystal lattice. In our case the instrumental factor and the structural characteristics of the samples can be left out of consideration since for all $Bi_{1-x}Sb_x$ solid solutions, the *X*-ray diffraction patterns were measured under identical conditions, the same volume of material was exposed to radiation, and the degree of dispersion of the powder and the strain hardening were also the same. That is why it can be safely suggested that the change in the XRDL with changing concentration of impurity atoms can be attributed to internal structural changes.

The broadening of the *X*-ray diffraction lines that we observed after the introduction of the first portions of *Sb* atoms (Fig. 2) is easy to explain taking into account that foreign atoms introduced into the crystal increase the level of local stresses in the crystal lattice. However, the subsequent sharp decrease in the XRDL shows that in certain concentration intervals, stresses in the crystal structure decrease.

In this connection it can be suggested that in the impurity subsystem of the crystal, self-organization processes take place, resulting in the appearance of an ordered structure. Possible self-organization processes may include a long-range ordering of impurity atoms ("crystallization of the impurity liquid") and short-range ordering (through formation of complexes). As the formation of an ordered structure must lead to lattice periodicity restoration, i.e. to a decrease in the number of defects in the crystal lattice, one should expect a decrease in XRDL, which is indeed observed in the concentration ranges $x = 0.005 - 0.01$, $x = 0.025 - 0.03$, and $x = 0.05 - 0.07$. The formation of a superstructure is expected to cause the appearance of extremum points in the dependences of different properties.

For the realization of a long-range ordering of impurity atoms, the average distance d between impurity atoms ($d = 1/n_o^{1/3}$ where n_o is the impurity atoms concentration) must correspond to their regular distribution over the sites of the crystal lattice (e.g., $d = na_o$ and $d = na_o/4^{1/3}$, respectively, for simple cubic and face-centered cubic lattices formed by impurity atoms, where n is an integer, a_o denotes the unit-cell parameter of the matrix material). If we assume the crystal lattice of $Bi_{1-x}Sb_x$ solid solutions to be a face-centered pseudocubic structure, then $a_o = V^{1/3}$, where V is the volume of the unit cell. A simple rough calculation shows that the compositions that are optimal for ordering in the case of the formation of a face-centered cubic crystal lattice of *Sb* atoms (i.e. compositions for which the condition $d = na_o/4^{1/3}$ is fulfilled) are close to $x = 0.01$ ($n = 4$), $x = 0.02$ ($n = 3$) and to $x = 0.07$ ($n = 2$). A sharp decrease in the XRDL, which was observed in the vicinity of the indicated compositions (Fig. 2), supports the possibility of ordering. When the solid solution region is sufficiently wide, with increasing impurity concentration, different variants of ordering can be realized. However, to prove that ordering has occurred and to determine its type, a special XRD study is required, which is beyond the scope of the present work.

In Fig. 3, along with the $a(x)$ dependence obtained in the present work for $Bi_{1-x}Sb_x$ solid solutions (Fig. 1 *b*), the isotherms of the magnetoresistance $\Delta\rho/\rho$ and Hall charge carrier mobility μ_H obtained at $T = 80$ K and $B = 0.9$ T in [16] are given. It is seen that the positions of extrema points near $x = 0.03$ and $x = 0.07$ in the isotherms of the lattice and electronic properties are practically similar. Let us also notice that the anomaly in the range $x = 0.005 - 0.01$ observed in [16] for the electronic properties and in the present work for the *X*-ray diffraction line width, is not observed for the unit cell parameters. This observation indicates that the formation of percolation channels, significantly affecting the transfer phenomena and the *X*-ray diffraction line width, does not cause noticeable changes in the unit cell parameters.

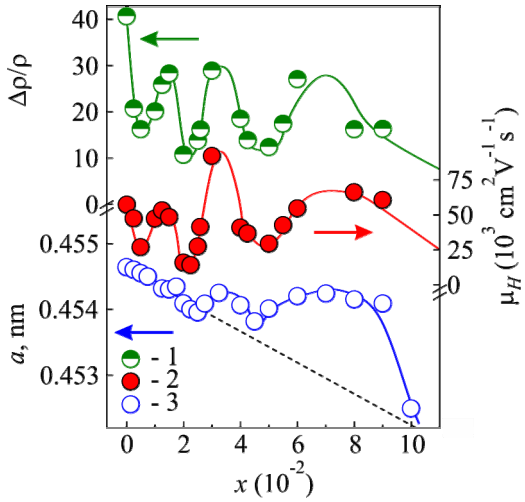

Fig. 3. The dependences of the magnetoresistance Δρ/ρ (1), Hall charge carrier mobility μ_H (2), and unit cell parameter a (3) on the Sb concentration x of $Bi_{1-x}Sb_x$ solid solutions at room temperature. Here (1), (2) refer to [16], and (3) to the present work.

Thus, it follows from the obtained data that the electronic phase transitions occurring in the studied range of concentrations are accompanied by the processes of structural ordering. The latter are manifested through the sharp narrowing of XRDL and the deviation from Vegard's law in the concentration intervals where extrema of electronic properties are observed. At present it is difficult to say which factor – electronic or structural – is primary in determining the appearance of the concentration anomalies of properties in $Bi_{1-x}Sb_x$ solid solutions, as in crystals the electronic and lattice subsystems are closely connected and can be considered independent only conventionally. One should not also exclude that for each of the critical concentration ranges ($x = 0.005 – 0.01$, $x = 0.025 – 0.03$ and $x = 0.05 – 0.07$) there exist two phase transitions – electronic and structural – which occur at close compositions.

Conclusions

For the first time it is here established that in $Bi_{1-x}Sb_x$ solid solutions in the concentration range $x = 0 – 0.1$, the dependences of the unit cell parameters and *X*-ray diffraction line widths on the *Sb* concentration exhibit a distinct non-monotonic oscillatory behavior: in the vicinity of compositions $x = 0.03$ and $x = 0.07$, the maximum positive deviations from Vegard's law are observed, and in the vicinity of compositions $x = 0.01$, 0.03, and 0.07, a narrowing of the *X*-ray diffraction lines takes place. The results obtained show that electronic phase transitions (a transition of a percolation type to impurity continuum, a transition to a gapless state accompanied by *L*-point inversion and by a semimetal-semiconductor transition), occurring in the same concentration intervals, are accompanied by structural changes in the crystal lattice, presumably connected with the formation of ordered structures. This, in turn, indicates a strong electron-phonon interaction in $Bi_{1-x}Sb_x$ solid solutions.

Acknowledgement. The authors thank Dr. Olga Naschekina and Shuang Tang for fruitful and stimulating discussions. This work was supported by the Ukrainian State Foundation for Fundamental Research (grant № UU 42/006-2011) and by the CRDF grant № UKP2-7074-KK-12. The MIT author acknowledges support from grants № NSF/DMR-1107339 and № RF01224242.

References

1. D.M. Rowe, *CRC Handbook of Thermoelectrics* (CRC Press, Boca Raton, London, New York, Washington, 1995).
2. V.S. Edelman, Electrons in Bismuth, *Adv. Phys.* **25** (6), 555 – 613 (1976).
3. B. Lenoir, M. Cassart, J.-P. Michenaud, H. Scherrer, and S. Scherrer, Transport Properties of *Bi*-Rich *Bi-Sb* Alloys, *J. Phys. Chem. Solids* **57** (1), 89 – 99 (1996).
4. A. Banerjee, B. Fauqué, K. Izawa, A. Miyake, I. Sheikin, J. Flouquet, B. Lenoir, and K. Behni, Transport Anomalies Across the Quantum Limit in Semimetallic $Bi_{0.96}Sb_{0.04}$, *Phys. Rev. B* **78**, 161103 (2008).
5. L. Fu, C.L. Kane, and E.J. Mele, Topological Insulators in Three Dimensions, *Phys. Rev. Lett.* **98**, 106803 (2007).
6. S. Murakami, Phase Transition Between the Quantum Spin Hall and Insulator Phases in 3D: Emergence of a Topological Gapless Phase, *New Journal of Physics* **9**, 356 – 372 (2007).
7. D. Hsieh, D. Qian, L. Wray, Y. Xia, Y.S. Hor, R.J. Cava, and M.Z. Hasan, A Topological Dirac Insulator in a Quantum Spin Hall Phase, *Nature* **452**, 970 – 974 (2008).
8. J.E. Moore and L. Balents, Topological Invariants of Time-Reversal-Invariant Band Structures, *Phys. Rev. B* **75**, 121306 (2007).
9. Ya.A. Ugay, E.G. Goncharov, G.V. Semenova, and V.B. Lazarev, *Phase Equilibrium between Phosphorus, Arsenic, Antimony and Bismuth* (Nauka, Moscow, 1989).
10. A.L. Jain, Temperature Dependence of the Electrical Properties of Bismuth-Antimony Alloys, *Phys. Rev.* **114** (6), 1518 – 1528 (1959).
11. N.B. Brandt, S.M. Chudinov, and V.G. Karavaev, The Study of the Gapless State, Induced by the Magnetic Field in Bismuth-Antimony Alloys, *Zh. Eksp. Teor. Fiz*. **70** (6), 2296 – 2317 (1976).
12. E.E. Mendez, A. Misu, and M.S. Dresselhaus, Pressure Dependent Magnetoreflection Studies of *Bi* and $Bi_{1-x}Sb_x$ alloys, *Phys. Rev. B* **24** (2), 639 – 863 (1981).
13. E.J. Tichovolsky and J.G. Mavroides, Magnetoreflection Studies on the Band Structure of Bismuth-Antimony Alloys, *Solid State Communs.* **7**, 927 – 931 (1969).
14. R. Herrmann, W. Braune, and G. Kuca, Cyclotron Resonance of Electrons in Semimetallic Bismuth-Antimony Alloys, *Phys. Stat. Sol. (b)* **68** (1), 233 – 242 (1975).
15. W. Braune, G. Kuka, H.J. Gollnest, and R. Herrmann, Microwave Spectroscopy in Semimetallic Bismuth-Antimony Alloys, *Phys. Stat. Sol. (b)* **89** (1), 95 – 101 (1978).
16. E.I. Rogacheva, A.A. Drozdova, and M.S. Dresselhaus, *Proc. Conf. Thermoelectrics* (July-August 2006, Vienna, Austria), ISSN 1094-2734, p. 107 – 110.
17. E.I. Rogacheva, A.A. Yakovleva, V.I. Pinegin, and M.S. Dresselhaus, Concentration Anomalies of Properties in *Bi-Sb* Semimetallic Solid Solutions, *J. Phys. Chem. Solids* **69** (2), 580 – 584 (2008).
18. I.L. Yarnell, I.L. Warren, R.G. Wenzel, and S.H. Koenig, Phonon Dispersion Curves in Bismuth, *J. Res. Dev.* **8** (3), 234 – 240 (1964).
19. J. Sosnowski, S. Bednarski, W. Bührer, A. Czachor, and E. Maliszewski, Phonon Dispersion Relations in the $Bi_{0.95}Sb_{0.05}$ Alloy, *Phys. Stat. Sol. (b)* **104** (1), 97 – 102 (1981).
20. N.P. Stepanov, Plasmon-Phonon Polaritons in an Acceptor Impurity-Doped Bismuth-Antimony Crystals, *Semiconductors* **38** (5), 552 – 555 (2004).
21. E.G. Bowen and W. Morris-Jones, *X*-ray Investigation of the Bismuth-Antimony, *Philosophical Magazine Series 7*, **13** (87), 1029 – 1032 (1932).
22. W.F. Ehret and M.B. Abramson, The Nature of the Solid Phase in the System Antimony-Bismuth. *J. Am. Chem. Soc.* **59** (2), 385 – 388 (1934).

23. R. Cucka and C.S. Barrett, The Crystal Structure of *Bi* and Solid Solutions of *Pb*, *Sn*, and *Te* in *Bi*, *Acta Crys.* **15** (9), 865 – 872 (1962).
24. M. Dugue, Proprietes Electriques des Solutions Solides Bismuth-Antimoine *Phys. Stat. Sol.* **11**, 149 – 158 (1965).
25. J.P. Dismukes, R.J. Paff, R.T. Smith, and R.J. Ulmer, Lattice Parameter and Density in Bismuth-Antimony Alloys, *Chemical and Engineering Data* **13** (3), 317 – 320 (1968).
26. V.J. Meisalo, Lattice Parameters of *Bi-Sb* Alloys at 4.2 K, *Applied Crystallography* **3** (2), 224 – 228 (1970).
27. N. Wagner and O. Brümme, Remarks on the Relation between Crystal Structure and Electronic Band Structure in Bismuth-Antimony Alloys, *Phys. Stat. Sol. (b)* **75**, K 157 – 161 (1976).
28. H. Berger, B. Christ, and J. Troschke, Lattice Parameter Study in the $Bi_{1-x}Sb_x$ Solid-solution System, *Crystal Research and Technology* **17** (10), 1233 – 1239 (1982).
29. U. Pietsch, The Validity of Vegard's Rule for the Solid Solution System $Bi_{1-x}Sb_x$, *Phys. Stat. Sol. (b)* **110** (1), K5 – K9 (1982).
30. R. Martin-Lopez, B. Lenoir, X. Devaux, A. Daucher, and H. Scherrer, Mechanical Alloying of BiSb Semiconducting Alloys, *Mater. Sci. Eng. A* **248**, 147 – 152 (1998).
31. G.N. Kozhemyakin, D.V. Lutskiy, M.A. Rom, and P.V. Mateychenko, Growth of Sb_xBi_{1-x} Gradient Single Crystals by the Czochralski Method with *Bi* Feed, *J. Crystal Growth* **311**, 1466 – 1470 (2009).
32. J. Druzek, Positron Preferential Annihilation in *Bi-Sb* Alloys, *Phys. Stat. Sol. B*, **246** (10), 2238 – 2241 (2009)
33. A.N. Doroshenko, A.A. Drozdova, V.I. Pinegin, and E.I. Rogacheva, *X*-ray Study of Bismuth-Antimony Solid Solutions, *Scientific Bulletin of Uzhgorod National University, Ser. Physics*, **30**, 107 (2011)
34. Ya.S. Umanskii, *X-Ray Study of Metals and Semiconductors* (Moscow: Metallurgiya, 1969), p. 38.

Submitted 26.11.2013.

O.N. Uryupin[1,2], Yu.V. Ivanov[1], A.A. Shabaldin[1], E.V. Konstantinov[2]

[1]A.F. Ioffe Physics and Technical Institute, 26, Polytekhnicheskaya Str.,
Saint-Petersburg, 194021, Russia;
[2]A.I. Herzen Russian State Pedagogical University, 48, Moika River emb.,
Saint-Petersburg, 191186, Russia

THERMOELECTRIC PROPERTIES OF NANOSTRUCTURES IN CHRYSOTILE ASBESTOS AND POROUS GLASS

The nanostructures of indium and bismuth antimonides in chrysotile asbestos channels and porous glasses have been studied. In asbestos channels, sufficiently perfect quasi one-dimensional wires are formed, and in porous glasses – three-dimensional nets of semiconductor materials. The electric conductance and thermopower of these nanostructures have been measured in the temperature range of 80 to 400 K. It is shown that transport properties of composites depend heavily on the type of a die and the semiconductor material forming a nanostructure. Many features of transport properties of the investigated nanowires can be, at least qualitatively, described by the Luttinger liquid theory. In the nanowires in chrysotile asbestos channels, the thermoelectric power factor increases quickly with a rise in temperature.

Key words: thermoelectricity, Luttinger liquid, nanowire, chrysotile asbestos, porous glass.

Introduction

In recent years, an active search for materials and structures with dimensionless thermoelectric figure of merit $ZT >> 1$ has been pursued. The investigations are conducted in various lines, however, it is only in nanostructures that considerable increase in thermoelectric figure of merit as compared to the value of $ZT = 1$ has been experimentally obtained. In 2001 Venkatasubramanian et al. manufactured superlattices based on bismuth telluride with the dimensionless thermoelectric figure of merit 2.4 at room temperature [1]. At about the same time Harman et al. [2] synthesized *PbSnSeTe*/*PbTe* superlattices consisting of quantum dots, with $ZT = 2.0$ at $T = 300$ K. In 2005 Harman managed to improve considerably his result [3] and obtained at a temperature of 550 K for *PbSeTe*/*PbTe* superlattices the value of $ZT \approx 3.0$. Higher ZT values have not been obtained so far, so a search for novel low-dimensional structures for thermoelectric power conversion continues to be a relevant objective.

According to theoretical estimates, high values of thermoelectric figure of merit can be exhibited by nanostructures consisting of ultrathin nanowires of diameter less than 10 nm [4-7]. However, at the present time in various laboratories worldwide intensive efforts are underway to study sufficiently thick nanowires of diameter ~ 50 nm of such thermoelectric materials as *Bi*, $Bi_{1-x}Sb_x$, Bi_2Te_3, *InSb*, *Si* [8-14], as well as irregular bismuth nanostructures in porous dies [15-17]. All these structures either have large characteristic diameters or differ markedly in their topological structure from quasi one-dimensional wires. So, no sensible increase in thermoelectric figure of merit has been achieved in this line of investigation thus far.

One should note a fundamental distinction of the electronic properties of quasi one-dimensional wires from the respective properties of nanostructures of larger dimensions. In quasi one-dimensional wires the electron-electron interaction results in formation of a specific strongly correlated state of electronic subsystem that came to be known as the Luttinger liquid [18]. The equilibrium and transport properties of the Luttinger liquid are radically different from those of the Fermi gas. For instance, the electric conductance (reverse resistance) of one-dimensional conductor quickly increases with a rise in temperature [19-21], like in semiconductors. The thermopower of the Luttinger liquid increases as a linear function of temperature [22-25], like in metals. Moreover, some calculations predict considerable increase in the thermopower of the Luttinger liquid as compared to that of the Fermi gas [22, 26]. All these properties of the Luttinger liquid hold much promise in terms of thermoelectric applications.

In this paper, some peculiarities of thermoelectric properties of ultrathin wires of indium and bismuth antimonides in chrysotile asbestos and porous glass channels have been studied. The above nanostructures have comparable diameters of the wires they are formed of (~ 5 – 7 nm), but differ in surface topology and roughness degree. It is shown that these features of nanostructures lead to a drastic difference in their transport properties.

Semiconductor nanostructures in porous dies

Estimates show that unltrathin nanowires of indium and, possibly, bismuth antimonide of diameter less than 10 nm must be quasi one-dimensional conductors, since the electrons in them fill only the lower subband of the energy spectrum resulting from dimensional quantization. The manufacture and use of single nanowires of such dimensions is a hard-to-solve problem, so we investigated semiconductor nanostructures obtained by indentation of molten material under high hydrostatic pressure to the pores of dielectric dies [27]. As such dies, chrysotile asbestos and porous glasses were used.

Natural mineral chrysotile asbestos [25, 27] is a tight packing of long nanotubes whose dimensions depend on the geological deposit or synthesis conditions. The internal diameters of asbestos nanotubes are generally 1 to 10 nm, the outer diameters – 10 to 100 nm. In each specific sample the spread of internal diameter values is not large. The samples used in this work had the average channel diameters 5 to 7 nm. These channels were filled with *InSb* or *Bi* melt at a pressure of ~ 15 kbar. The samples cut from asbestos pieces filled in this fashion consisted of 10^5 to 10^7 parallel asbestos nanotubes whose images obtained using electric scanning microscope (SEM) are shown in Fig. 1. Inside each nanotube there is a readily visible channel filled with a semiconductor material.

Analysis of *X*-ray diffraction spectrum of an asbestos die filled with indium antimonide has shown that on entering nanotube channels, the semiconductor does not change its stoichiometric composition. In so doing, high crosswise fillability of channels is observed and nanocrystallites with the average characteristic dimension 4.4 nm are formed [28].

The rigid frame of porous glass [27, 29, 30] consists mainly of SiO_2. The concentration of this oxide is approximately 96 %. The pores of this material are interconnected and form a three-dimensional net consisting of short channels. Unlike chrysotile asbestos, the channels in porous glass have an irregular surface shape, differing dramatically from the cylinder one. The specific feature of porous glasses is a narrow maximum in the distribution of pores according to their lateral dimensions. The width of this maximum at half the height is approximately 0.15 of the average diameter of pores in the sample [30]. At the same time, changing glass synthesis conditions, the average diameter of pores can be varied from several angstroms to several microns.

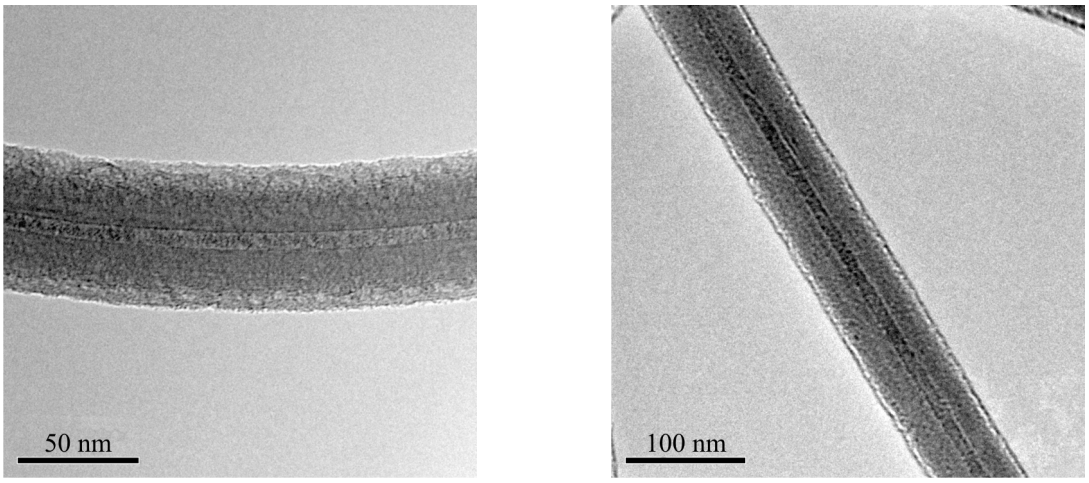

a) *b)*

Fig. 1. SEM-images of two chrysotile-asbestos nanotubes filled with InSb.

In this work, porous glasses with the average lateral dimension of pores ~ 7 nm, close to the average diameter of channels in chrysotile asbestos, were selected. In this case possibility emerges to carry out a comparative analysis of thermoelectric properties of long quasi one-dimensional wires and three-dimensional nets consisting of short nanowires with the same characteristic dimensions. Fig. 2 represents SEM-images of the surfaces of two porous glasses with different dimensions of pores. In the pictures, pores are matched by the darker areas. It is seen that in Fig. 2 *a* the average diameter of pores is ~ 1 μm and Fig. 2 *b* shows a glass with characteristic dimensions of pores 6 to 10 nm that are almost coincident with the internal diameters of the above described asbestos nanotubes.

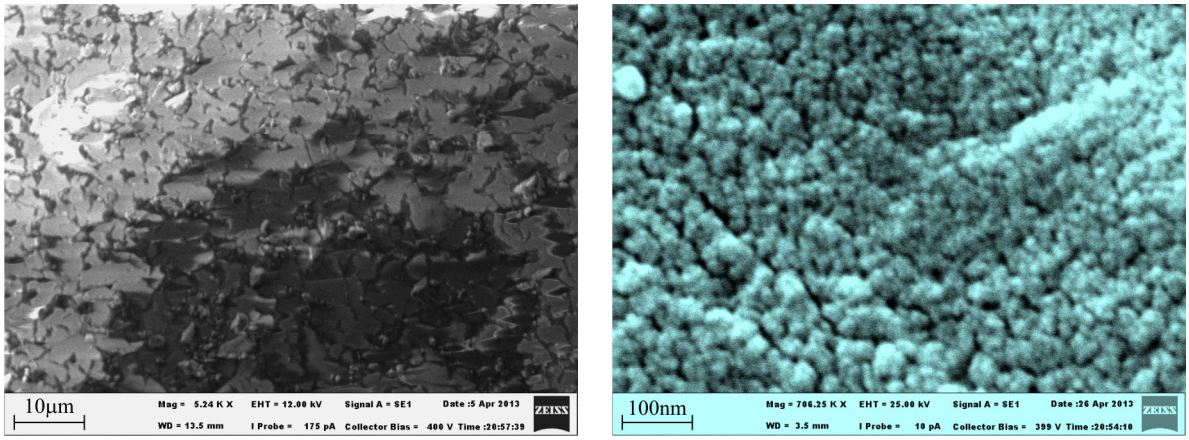

a) *b)*

Fig. 2. SEM-images of the structure of two porous glasses with lateral dimensions of pores ~ 1 μm (a) and 6 – 10 nm (b).

Semiconductor nanostructures in porous glasses were manufactured in the same way as nanowires in asbestos dies. Capsules used for the preparation of composite samples were simultaneously filled with pieces of chrysotile asbestos and the respective porous glass.

To determine the composition of manufactured nanocomposites, the energy-dispersive *X*-ray analyzer INCA *X*-Act from Oxford Instruments was used. The *X*-ray spectra and atomic composition of porous glass filled with *InSb* are represented in Fig. 3. Within the measurement error the

concentration of indium and antimony in the composite corresponds to stoichiometric composition of the initial semiconductor.

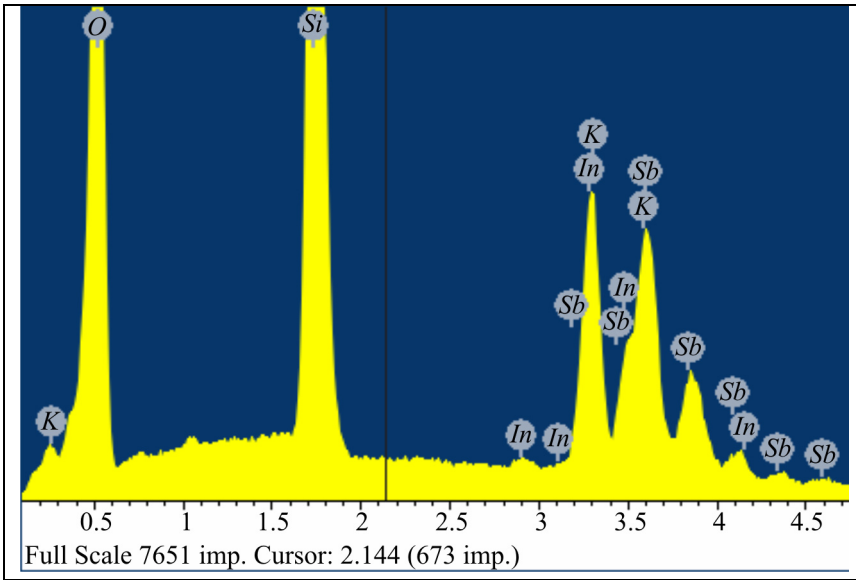

Element	Composition (at. %)
O	66.45
Si	21.10
K	0.20
In	6.24
Sb	6.02

Fig. 3. X-ray spectrum and the results from the compositional analysis of porous glass filled with InSb.

Thus, the above-described procedure for preparation of samples of semiconductor nanostructures allows creating both long quasi one-dimensional wires in chrysotile asbestos channels of diameter 5 to 7 nm and three-dimensional nets of short nanowires of approximately the same diameter. It should be noted that despite the comparable characteristic dimensions, these nanostructures differ in topology. Moreover, the lateral dimensions of a wire in a porous glass change with lengthwise displacement. Therefore, the electron band structure of a semiconductor net in a porous glass to all appearance may be regarded as a totality of connected quantum dots.

Method for measuring the thermopower of nanostructures

The samples of nanostructures obtained by the above-described method can have high electric resistances ~ 10^6 to 10^8 Ω, since in the process of manufacturing not all the channels in the initial dies are filled with semiconductor materials. The investigation of the thermoelectric properties of such objects requires special methods for measuring kinetic coefficients. The most complicated problem is thermopower measurement at high electric resistance values of samples.

Our experimental setup is intended for measuring the thermopower of nanowire bunches in the temperature range of 80 to 400 K. This setup employs a comparative method of thermopower measurement. On the measured and reference samples an identical temperature difference ΔT is created which is then calculated based on the known thermopower of the reference sample. Such an approach requires no direct measurement of ΔT and increases the accuracy of result due to increased signal-noise ratio.

The samples made of nanowire bunches had a length of 1 to 2 mm and a section of ~ 0.01 mm^2. Ohmic contact was provided by indium electrodes. With a view to minimize the resistance, the distance between the indium electrodes was set of the order of 0.3 to 0.1 mm. For thermopower measurement high-resistance voltmeters with input resistance at least 10 GΩ were used. The basic elements of the experimental setup are represented in Fig. 4.

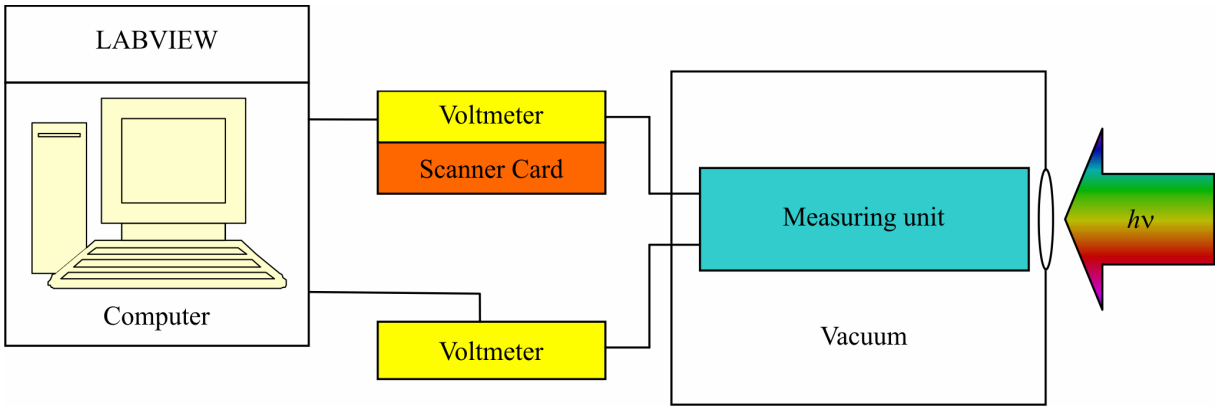

Fig. 4. Simplified circuit of measuring setup

Measuring unit was placed into vacuum chamber. The main element of measuring unit is a holder with two pairs of clamps arranged on it, in one of which the sample under study is clamped, and in the other – the reference. As the reference, calibrated constantan was used. To reduce electric pickup in measuring circuits, the clamps were electrically isolated from the package of measuring unit with retention of the necessary thermal contact. For creation of temperature difference the electric heaters shall not be used because of electric pickup and electric shunting of sample due to leakage currents in the circuits. Therefore, temperature difference on the samples was created by lighting the receiving plate of the hot clamps. In order to minimize parasitic heat fluxes, both clamp pairs were covered with thermal shield.

Fig. 5 shows one of the clamp pairs. On the left there is a cold clamp (8) having a good thermal contact to the holder, so its temperature differs from that of the body at most by 2 K. On the right there is a hot clamp (6). Between this clamp and the copper body (1) there is stainless steel heat spreader (3) having a relatively high thermal resistance and making it possible to obtain temperature difference on the sample. The hot clamp is heated by intensive light beam incident on thermal radiation detector (5) that was blackened with a view to improve light absorption. Such a design assures reliable shading of the object under study.

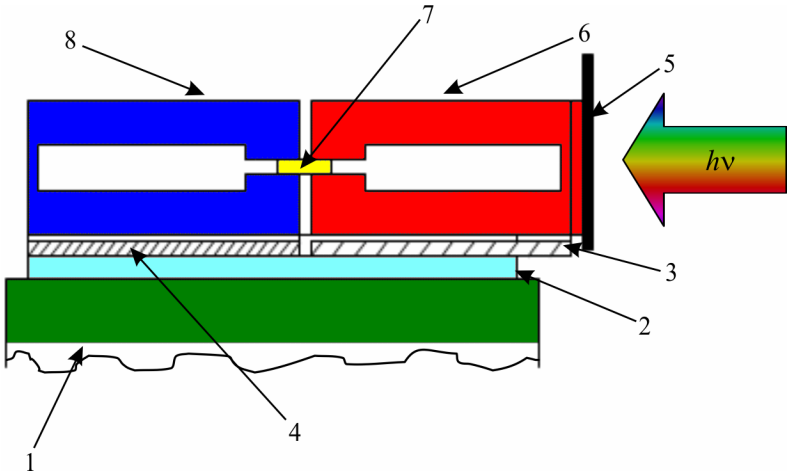

Fig. 5. Schematic of samples holder: 1 – copper body; 2 – dielectric substrate BeO; 3 – stainless steel; 4 – copper plate; 5 – heated element (Cu); 6 – hot clamp; 7 – sample or standard; 8 – cold clamp.

The temperature dependence of the thermopower of the object under study was measured simultaneously with measuring the thermopower of the reference. The measured data was fed into the computer, and the results were used to calculate the Seebeck coefficient of the sample:

$$S_{sample} = S_{ref} \cdot U_{sample} \cdot K(T) / U_{ref}, \quad (1)$$

where S_{ref} is the Seebeck coefficient of the reference, U_{sample} is voltage on the sample, U_{ref} is voltage on the reference, $K(T)$ is correction factor taking into account small diversity of temperature drops on the sample and reference, determined with a parallel measurement of two references.

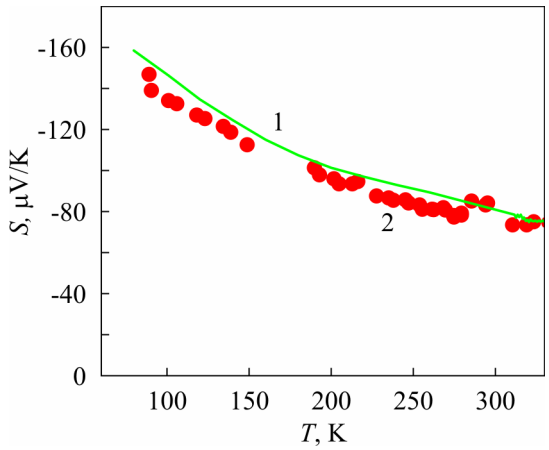

Fig. 6. Temperature dependences of the Seebeck coefficient of $Bi_{0.85}Sb_{0.15}$ single crystal measured by the absolute (1) and relative (2) methods.

Fig. 6 represents the results of testing the above-described experimental setup. The temperature dependence of the Seebeck coefficient S_{11} of $Bi_{0.85}Sb_{0.15}$ single crystal was measured and compared to a similar dependence obtained by traditional absolute method of thermopower measurement. The choice of $Bi_{0.85}Sb_{0.15}$ single crystal as a test material was determined by high homogeneity, stability of properties, high thermopower values and practical isotropy of thermoelectric properties. The difference in the temperature dependences of the Seebeck coefficient of the same $Bi_{0.85}Sb_{0.15}$ crystal measured by the absolute and relative methods does not exceed 10 %, which is a wholly satisfactory result.

Discussion of measurement results

All nanostructures under study consist of ultrathin nanowires having comparable lateral dimensions. Estimates show that strong dimensional quantization of the electron spectrum should cause the emergence in them of a wide forbidden band (~ 500 meV), and the energy gap between the first and upper subbands should be more than 200 meV. Therefore, at temperatures below 300 K only the electrons of the lower spectrum subband must contribute to impurity conduction (all nanostructures under study had *n*-type conductivity). In the circumstances, one might expect the similarity of temperature dependences of the electron kinetic coefficients in all nanostructures considered. However, measurements have shown that the thermoelectric properties of these nanostructures are qualitatively different. They depend on the type of the die used and the semiconductor material it is filled with. Moreover, they may be drastically different even in the samples cut from the same initial piece of composite. The large variety of properties and their dominant physical processes invite further investigations. Below we turn our attention only to some specific features of nanostructures considered.

All one-type samples (for instance, *InSb* nanowires in asbestos die) can be conventionally divided into three groups. The first-group samples have high resistance $R > 10^5$ Ω at 300 K. This group of samples is characterized by abrupt electric resistance jumps on cooling and heating. As a rule, these jumps are irreversible and after several measurement cycles result in resistance increase to 10^{14} Ω and more. We believe that these samples have only a small amount of defective through wires

(wire clusters in porous glasses). Due to the effect of elastic stresses arising with temperature change and electric migration of defects, the wires are broken, leading to a drastic resistance increase. When a considerable electric voltage is applied, a concurrent break of the entire array of wires is possible [31] which is initiated by the electrostatic field of the first broken wire and leads to practically complete sample failure. In some cases on thermal cycling there are reversible resistance jumps (see Fig. 7). We cannot interpret this effect unambiguously. It is likely that such nanostructure behaviour is caused by the difference in the coefficients of linear thermal expansion of semiconductor and die, leading to the emergence of strains which with a drop in temperature break the wires, and then restore the conductivity on heating.

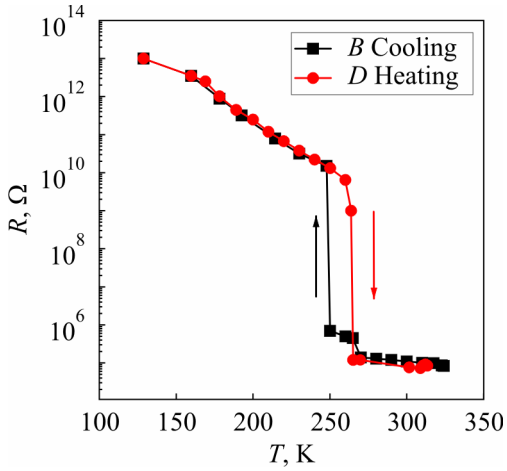

Fig. 7. Temperature dependence of the electrical resistance of InSb sample in the asbestos die belonging to the first group. Temperature change directions are indicated by the arrows.

The second-group samples have low resistances ($< 10^3$ Ω), smoothly and reversibly changing with temperature variation. The thermopower of these samples often changes its sign with temperature variation, and the temperature dependences of conductance in indium antimonide nanostructures are of activation nature [32], like in the bulk semiconductors. An example of such $S(T)$ dependence for bismuth nanowires in asbestos die is given in Fig. 8 (red curve). Such behaviour of second-group samples is due to the presence in them of a crack filled with semiconductor. In the process, a conducting channel with a characteristic dimension of ~ 1 μm is formed. Electron scattering by the channel surface reduces their contribution to thermopower and results in the Seebeck coefficient's sign reversal (classical dimensional effect).

Of greatest interest from physical and practical standpoints are the third-group samples. They are relatively stable, and at room temperature their resistances are $10^3 < R < 10^7$ Ω. Their thermopower is proportional to temperature (sometimes there are slight deviations from proportionality), like in metals. Conductance, as a rule, is increased with a rise in temperature, like in semiconductors. However, in contrast to them, $G(T)$ dependence is not of activation nature. The thermoelectric properties of this group of samples are governed by sufficiently perfect quasi one-dimensional semiconductor wires or their three-dimensional nets.

Special emphasis should be placed on the thermoelectric properties of ultrathin *InSb* wires in the asbestos die (third-group samples). As mentioned above, in quasi one-dimensional conductor due to increased effect of electron-electron interaction, a strongly correlated state of electron subsystem is formed which was called the Luttinger liquid [18]. Unlike the Fermi liquid, the elementary excitations in the Luttinger liquid are collective excitations similar to phonons, rather than quasi-particles. According

to theory, the temperature dependence of a linear conductance of the Luttinger liquid containing a defect (or several independent defects) should be described by power function $G \propto T^{\alpha}$, where power exponent α is determined by the value of electron-electron interaction [19, 20]. The thermopower should be proportional to temperature [22, 23]. These dependences for one of the samples with quasi one-dimensional *InSb* wires are represented in Fig. 9, and, for the sake of illustration, the plot of $G(T)$ dependence is built in log-log scale. It is seen that the plot in Fig. 9 *a* at $T < 250$ K is practically linear and corresponds to $G \propto T^{5.2}$ dependence. The thermopower of the same sample represented in Fig. 9 *b* in the range of $T < 300$ K is really proportional to temperature. Slight deviations of the represented curves from the theoretical dependences at $T > 250$ K seem to be related to the violation of electron subsystem strong degeneracy condition which governs the applicability of the Luttinger liquid theory.

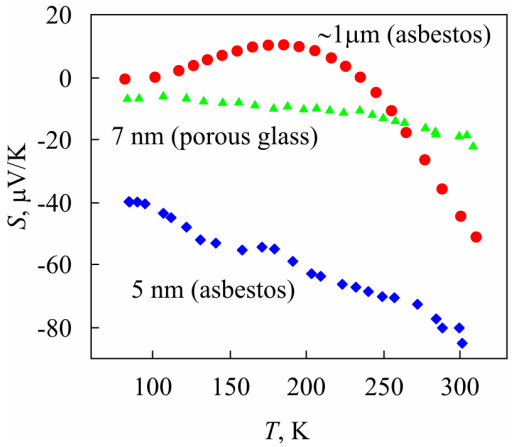

Fig. 8. Temperature dependences of thermopower of bismuth in chrysotile asbestos nanotubes (blue diamonds), in porous glass nanopores (green triangles) and in asbestos die crack (red circles). The approximate characteristic dimensions of structures are indicated.

It should be noted that the sample whose data is represented in Fig. 9 was manufactured with the use of tellurium-doped indium antimonide. By our estimates, the concentration of electrons in it was $\sim 4 \cdot 10^{18}$ cm^{-3}. In so doing, the Fermi energy in the bulk *InSb* should be ~ 270 meV, and in the wires of diameter 7 nm – ~ 60 meV. Therefore, the thermopower values in Fig. 9 *b* are not high. In similar samples, but not doped with tellurium, the absolute thermopower value at room temperature can reach 200 μV/K [24].

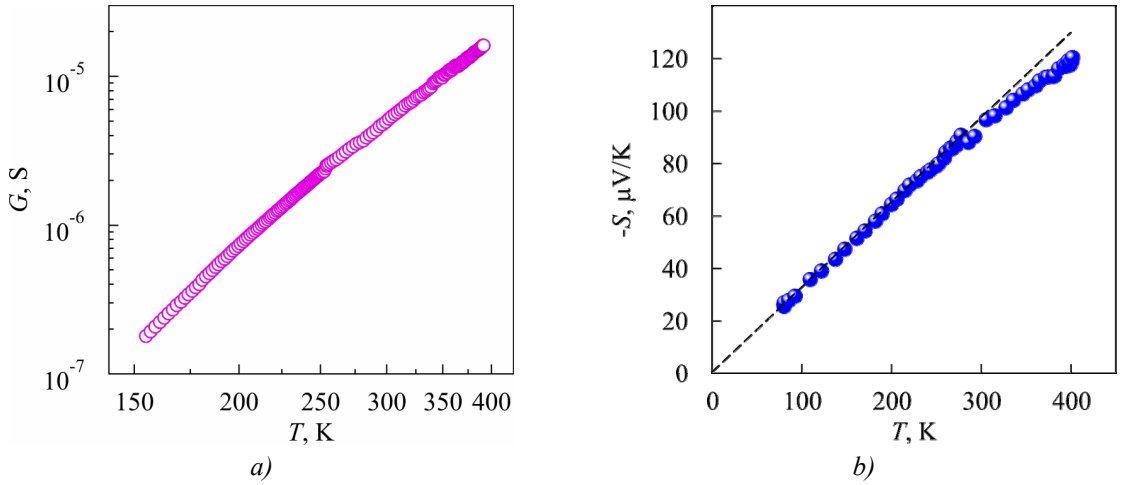

Fig. 9. Temperature dependences of conductance (a) and thermopower (b) of a sample cut from chrysotile asbestos filled with InSb. The dashed line shows the $S \propto T$ dependence.

Unlike quasi one-dimensional *InSb* wires in asbestos die, similar samples consisting of bismuth wires of the same diameter have practically temperature-independent conductance. The temperature dependence of thermopower for one of such samples is shown in Fig. 8 (blue curve). It is little different from the dependence represented in Fig. 9 *b*. However, in this case strict proportionality of the Seebeck coefficient to temperature, if any, exists only in the low-temperature region. Such differences in the properties of one-type nanostructures cannot be explained so far. It may be related to the surface states [33] that determine the electronic properties of bismuth thin films and wires.

The thermoelectric properties of nanostructures based on porous glass differ from the considered properties of nanowires in chrysotile asbestos. The conductance of three-dimensional nets formed by short wires of both indium antimonide and bismuth slowly grows with a rise in temperature [21, 34]. The temperature dependence of thermopower of bismuth in porous glass is shown in Fig. 8 (green curve). The distinctive feature of this dependence is the abnormally low thermopower value. It is, for instance, 4 to 5 times lower than the thermopower of quasi one-dimensional bismuth wires in asbestos. There is no unambiguous explanation of such a drastic difference in the properties of nanostructures with equal characteristic dimensions. At first glance, it may seem that strong shape irregularity of bismuth wires in porous glass should result in strong Anderson localization of electrons. However, in [34] it is shown that in such nanostructures at low temperatures only small localization of charge carriers is possible.

The most probable reason for a strong difference between thermopower values of the two considered nanostructure types lies in the different nature of their electron states. In quasi one-dimensional wires in asbestos dies the Luttinger liquid is formed, whereas in nanostructures in porous glass due to their three-dimensionality a conventional Fermi-liquid is formed. Moreover, in theoretical works [22, 23, 26] it is asserted that the thermopower of the Luttinger liquid should exceed manifold that of the Fermi gas. However, in our opinion, the study of this problem is far short of completion. Electron spectrum nonlinearity does not contribute to the thermopower of the Luttinger liquid [35]. The contribution to transport properties of electron-phonon interaction should not be considerable either, since in one-dimensional degenerate semiconductors there are few phonons capable of inverting electron pulse. At the same time, the contribution to the Luttinger liquid transport properties of electron scattering on defects (potential barriers) is governing due to formation of a quasi-gap in the tunneling density of states [18, 19]. In [26] it is shown that the thermopower of the Luttinger liquid comprising two closely-spaced barriers (quantum well) should be increased by electron-electron interaction. However, depending on quantum well parameters this contribution can be of any sign. Therefore, with averaging over the defective structure of a real nanowire this process should not be a major contribution to thermopower. Of great significance is a model considering the Luttinger liquid with one potential barrier (or several independent barriers). It is stated [23] that here again the thermopower should be increased manyfold as compared to that of the Fermi gas. However, another calculation [36] of a similar module yielded the opposite result, namely the contribution to thermopower of electron scattering on the barrier proved to be considerably less than the respective contribution to thermopower of the Fermi gas. Thus, further investigations are necessary to clarify the peculiarities of nanostructures considered.

Conclusion

Sufficiently perfect semiconductor nanostructures have been manufactured in chrysotile asbestos and porous glass channels with characteristic dimensions of 5 to 7 nm. The semiconductor

material retains its stoichiometric composition on indentation into nanoporous dies. Very long quasi one-dimensional wires are formed in asbestos channels. The nanostructures in porous glasses are a three-dimensional net consisting of arbitrary-shaped short wires. The thermoelectric properties of nanostructures depend heavily on the type of a die and the semiconductor it is filled with. Moreover, certain property variations are observed even in the samples cut from the same composite. Of greatest interest, both in terms of basic physics, and for practical application, are quasi one-dimensional indium antimonide wires in the channels of asbestos nanotubes. The temperature dependences of thermopower and electrical conductance of these wires are adequately described by the Luttinger liquid theory. For practical purposes it may be beneficial to use the high thermopower of these wires that far exceeds the thermopower of the bulk filling material and that of the respective nanostructure in a porous glass. Moreover, in quasi one-dimensional indium antimonide wires the power factor increases quickly with a rise in temperature. This feature may be of advantage in the development of nanostructured materials for thermoelectric power conversion.

The work was supported by the Russian Foundation for Basic Research (grant № 12-08-00688 a).

References

1. R. Venkatasubramanian, E. Siivola, T. Colpitts, and B. O'Quinn, *Nature* **413**, 597 (2001).
2. T.C. Harman, P.J. Taylor, M.P. Walsh, and B.E. LaForge, *Science* **297**, 2229 (2002).
3. T.C. Harman, M.P. Walsh, B.E. LaForge, and G.W. Turner, *J. Electron. Mater*. **34**, L19 (2005).
4. L.D. Hicks and M.S. Dresselhaus, *Phys. Rev. B* **47**, 16631 (1993).
5. Y.-M. Lin, X. Sun, and M.S. Dresselhaus, *Phys. Rev. B* **62**, 4610 (2000).
6. N. Mingo, *Appl. Phys. Lett.* **84**, 2652 (2004), (Erratum: *Appl. Phys. Lett*., **88**, 149902 (2006)).
7. I. Bejenari, V. Kantser, and A.A. Balandin, *Phys. Rev. B* **81**, 075316 (2010).
8. A.I. Hochbaum, R. Chen, R.D. Delgado, W. Liang, E.C. Garnett, M. Najarian, A. Majumdar, and P. Yang, *Nature* **451**, 163 (2008).
9. A.I. Boukai, Y. Bunimovich, J. Tahir-Kheli, J.-K. Yu, W.A. Goddard, and J.R. Heath, *Nature* **451**, 168 (2008).
10. A. Mavrokefalos, A.L. Moore, M.T. Pettes, L. Shi, W. Wang, and X. Li, *J.Appl. Phys*. **105**, 104318 (2009).
11. F. Zhou, A.L. Moore, M.T. Pettes, Y. Lee, J.H. Seol, Q.L. Ye, L. Rabenberg, and L. Shi, *J. Phys. D: Appl. Phys*. **43**, 025406 (2010).
12. Y.-M. Lin, O. Rabin, S.B. Cronin, J.Y. Ying, and M.S. Dresselhaus, *Appl. Phys. Lett.* **81**, 2403 (2002).
13. F. Zhou, J.H. Seol, A.L. Moore, L. Shi, Q.L. Ye, and R. Scheffler, *J. Phys.: Condens. Matter* **18**, 9651, (2006).
14. T.E. Huber, A. Adeyeye, A. Nikolaeva, L. Konopko, R.C. Johnson, and M.J. Graf, *Phys. Rev. B* **83**, 235414 (2011).
15. T. Huber, A. Nikolaeva, A. Gitsu, D. Konopko, M.J. Graf, and J. Huang, arXiv:cond-mat/0311112.
16. J.P. Heremans, C.M. Thrush, D.T. Morelli, and M.-C. Wu, *Phys. Rev. Lett.* **88**, 216801, (2002).
17. M.S. Dresselhaus, and J.P. Heremans, in *Thermoelectrics Handbook: Macro to Nano*, edited by D.M. Rowe (CRC Press, Taylor & Francis Group, Boca Raton, FL, 2006), pp. 39 – 1 – 39-20.
18. T. Giamarchi, *Quantum Physics in One Dimension* (Oxford University Press, 2003).
19. C.L. Kane and M.P.A. Fisher, *Phys. Rev. B* **46**, 15233 (1992).

20. M. Bockrath, D.H. Cobden, J. Lu, et al., *Nature* **397**, 598 (1999).
21. S.V. Zaitsev-Zotov, Y.A. Kumzerov, Y.A. Firsov, and P. Monceau, *J. Phys.: Condens. Matter*. **12**, L303 (2000).
22. I.V. Krive, E.N. Bogachek, A.G. Scherbakov, and U. Landman, *Phys. Rev. B* **63**, 113101 (2001).
23. I.A. Romanovsky, I.V. Krive, E.N. Bogachek, and U. Landman, *Phys. Rev. B* **65**, 075115 (2002).
24. O.N. Uryupin, M.V. Vedernikov, A.A.Shabaldin, Y.V. Ivanov, Y.A. Kumzerov, and A.V. Fokin, *J. Electron. Mater*. **38**, 990 (2009).
25. M.V. Vedernikov, Y.V. Ivanov, O.N. Uryupin, and Y.A. Kumzerov, in *Thermoelectrics and its Energy Harvesting. Modules, Systems, and Applications in Thermoelectrics*; ed. by D.M. Rowe, (CRC Press, Taylor & Francis Group, Boca Raton, London, New York, 2012), pp. 5-1 – 5-17 .
26. K.-H. Yang, Y. Chen, H.-Y. Wang, and Y.-J. Wu, *J. Low Temp. Phys*. **167**, 26 (2012).
27. Y. Kumzerov and S. Vakhrushev, in *Encyclopedia of Nanoscience and Nanotechnology*, edited by H.S. Nalwa (American Scientific Publishers, Los Angeles, 2004, Vol. 7), pp. 811 – 849.
28. O.N. Uryupin, N.F. Kartenko, Y.V. Ivanov and M.V. Vedernikov, Reports to XII Intregovernmental Workshop "Thermoelectrics and Their Applications" (S.-Petersburg, 2010), p. 79.
29. D. Enke, F. Janowski, and W. Schwieger, *Microporous and Mesoporous Materials* **60**, 19 (2003).
30. P. Levitz, G. Ehret, S.K. Sinha, and J.M. Drake, *J. Chem. Phys*. **95**, 6151 (1991).
31. S. Shekhar, M. Erementchouk, M.N. Leuenberger, and S.I. Khondaker, *Appl. Phys. Lett.* **98**, 243121 (2011).
32. M.V. Vedernikov, O.N. Uryupin, B.M. Goltsman, Yu.V. Ivanov, and Yu.A. Kumzerov, *MRS 2001 Fall Meeting Proceedings. Symposium G: Thermoelectric Materials 2001 – Research and Applications* (November 26-30, 2001, Boston, USA; Vol. 691, p. G.8.34.1 – G.8.34.6, 2002).
33. P. Hofmann, *Prog. Surf. Sci*. **81**, 191 (2006).
34. T.E. Huber, and M.J. Graf, *Phys. Rev. B* **60**, 16880 (1999).
35. Y.V. Ivanov, *J. Phys.: Condens. Matter* **22**, 245602 (2010).
36. Yu.V. Ivanov, *Reports to XIII Intergovernmental Workshop "Thermoelectrics and Their Applications"* (S.-Petersburg, November 13-14, 2012), p. 73.

Submitted 24.09.2013.

I.A. Kruglov[1,2], N.R. Serebryanaya[1,2], G.I. Pivovarov[1], V.D. Blank[1,2]

[1]Technological Institute for Superhard and Novel Carbon Materials of Ministry of Education and Science of RF, 7 a, Centralnaya Str., Troitsk, 142190, Russian;
[2]Moscow Institute of Physics and Technology, 9, Institutskii per., Dolgoprudny, 141700, Russia

THE METASTABLE PHASE Bi_2Te_3-*m* OBTAINED DIRECTLY FROM THE SEPARATE ELEMENTS

A Bi_2Te_3-m metastable phase has been obtained from the stoichiometrically mixed separate elements (Bi and Te) by the HPHT- treatment and mechanical alloying methods. Structure of the new phase has been clarified by Rietveld refinement. The density and hardness of the samples have been measured. The homogeneity of initial and metastable phases was investigated by the scanning electron microscopy (SEM). The temperature region of Bi_2Te_3-m stability was defined by the differential scanning calorimetry. The thermoelectric properties of Bi_2Te_3-m have been measured.
Key words: pressure-induced phase transition, *X*-ray diffraction, thermoelectric material, mechanical alloying.

Introduction

The bismuth telluride is widely used as a base material in the thermoelectric cooling systems and converters of heat into electric energy at room temperatures, so the investigation of its properties is highly important. Recently, pressure dependencies of the electrical resistance, thermal conductivity, and thermal power (Seebeck coefficient) [1, 2, 3] along with the resistance and the Hall coefficient [4] of Bi_2Te_3 have been studied up to 10 GPa. An experimental study has been carried out up to 29 GPa in diamond anvil cells [5, 6, 7], where reversible pressure-induced phases have been found; the experimental data have been confirmed by theoretical calculations [7]. The structures and bulk properties of the new phases [3, 5] were investigated. The fascinating electronic properties of Bi_2Te_3 were detected. For example, the electronic topological transition in Bi_2Te_3 under the high pressure was observed [8], the structural phase transition of Bi_2Te_3 from normal to superconductive state was found [9]. The atomic structure of the latter phase was determined by particle-swarm optimization method [10].

Earlier Bi_2Te_3 metastable phase has been observed after HPHT-treatment at a pressure $P > 6$ GPa and temperature $T > 800$ °C [11]. Here we investigated the formation of this phase from separate elements (*Bi* and *Te*) in stoichiometric proportion using quenching at high pressure and high temperatures. We studied the stability, structural and thermoelectric properties of the metastable phase at ambient conditions. The authors of [11] denoted the discovered phase as Bi_2Te_3 II, but this notation was later used for another pressure-induced phase [6], then we labeled this phase as Bi_2Te_3-*m* (metastable).

Experiment

Previously the Bi_2Te_3-*m* metastable phase was obtained from the initial compound of Bi_2Te_3 (I) [11]. In order to increase the thermoelectric figure of merit, it was suggested to synthesize the Bi_2Te_3-*m*

metastable phase directly from the initial elements under pressure. Bismuth and tellurium (Aldrich: *Bi* 99.999 %, *Te* 99.999 %) were taken as initial elements. The *Bi* and *Te* ingots taken in stoichiometric proportion were crushed and rubbed in a mortar. We synthesized the metastable high-pressure-phase from these materials by a rapid quenching after the electrical current thermoresistive heating of the "anvil with cavity" high-pressure apparatus [12]. The sample cooling rate was ≈ 60 °C/min, and pressure reduction rate in the reaction cell ≈ 1 GPa/min.

Mechanical alloying (MA) was used to obtain the new phases of Bi_2Te_3 with a higher figure of merit (*ZT*), but at lower pressures [13, 14] using an AGO-2U planetary mill. In order to avoid possible contamination of treated materials by oxygen and water vapor, all the procedures with the mixtures were carried out in a glove box filled with argon of purity not less than 0.1 ppm. A stoichiometric mixture of powders of bismuth and tellurium was placed in the mill's drums. The tungsten carbide balls WC6 of diameter 10 mm, weight 6.2 g, were used as the milling bodies for generation of higher pressures and temperatures during collision of balls.

The appearance of Bi_2Te_3-*m* metastable phase was determined by comparing the diffractograms of Bi_2Te_3-*m* and Bi_2Te_3 (I). A Bi_2Te_3-*m* diffractogram obtained after quenching at 7.7 GPa and 700 °C from the original Bi_2Te_3 (I) alloy was taken as a standard of the new phase. The *X*-ray powder diffraction patterns were obtained by using ARL X´TRA powder diffractometer (*Cu-K*a radiation) equipped with a solid-state (*Si*(*Li*)) semiconductor detector.

Thereby, the samples were obtained in three different ways:

1. Processing of a stoichiometric *Bi* and *Te* mixture under the 7.7 GPa pressure and 700 °C temperature in a hydraulic press.
2. Mechanical alloying of a stoichiometric *Bi* and *Te* mixture at mill's speed of rotation 1090 rot./min and 1 hour holding time.
3. Sintering of the mechanically alloyed Bi_2Te_3 (I) powder under the 5.5 GPa pressure at 600 °C.

Results and discussion

Diffractograms of the metastable phase Bi_2Te_3-*m* are shown in Fig. 1.

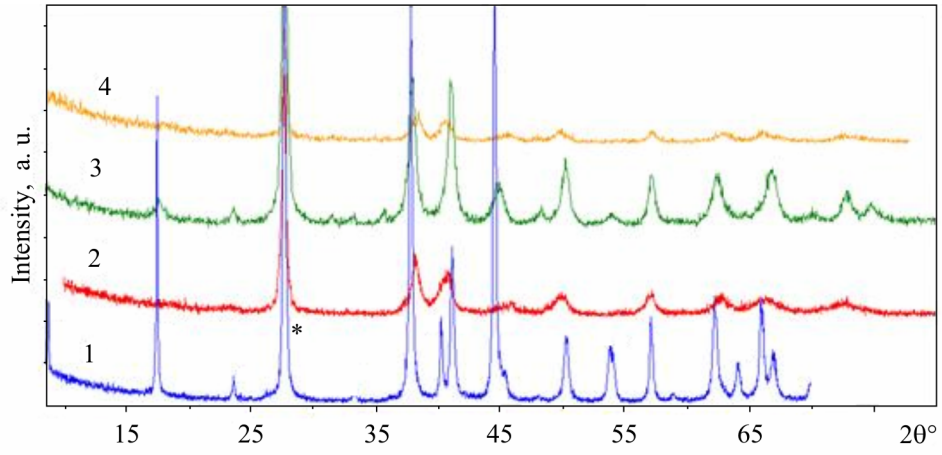

*Fig. 1. X-ray diffractograms of Bi_2Te_3-m obtained by three different ways. 1) initial Bi_2Te_3 (I); 2) Bi_2Te_3-m obtained by the 1st method; 3) mixture of Bi_2Te_3 (I) and Bi_2Te_3-m obtained by the 2nd method; 4) Bi_2Te_3-m obtained by the 3rd method. No appearance of Bi_2Te_3 (I) in patterns (2) and (4) was found. Only one strongest peak (about 2θ ~ 28°) of the initial phase coincides with peak of new phase (marked by asterisks *).*

While using the 1-st and 3-rd method, the *Bi_2Te_3-m* outcome was 100 %. We can conclude that it is a new phase, because the peaks change their positions and intensity. After MA (the 2-nd method), we can conclude that there is a mixture of the initial and metastable phases in the planetary mill drums (Fig. 1, No 3), because the reflections corresponding to the *Bi_2Te_3* (I) lose their intensity (in comparison with an initial phase diffractogram), but peaks of the metastable phase start appearing (in comparison with diffractograms 2 or 4). The Rietveld analysis showed that 20 – 30 % of the first phase in the metastable phase transforms after mechanical alloying. The diffraction peaks of the sample obtained by the 3-rd method were broad, i.e. the coherent region is very small (50 nm). The new phase of *Bi_2Te_3-m* is not a mechanical mixture of two elements, because the diffractograms have no separate peaks of bismuth and tellurium.

Cell parameters of the initial and metastable phases are shown in Table 1. The difference in volumes is 0.6 %.

Table 1

Parameters of Bi_2Te_3 (I) and Bi_2Te_3-m

Phase	Space group	*a*, Å	*c*, Å	*V*, Å^3	ρ, g/cm^3
Bi_2Te_3 (I)	$R\bar{3}m$	4.40	30.44	509.28	7.834
Bi_2Te_3-m	$R3m$	4.42	29.84	503.87	7.962

By the Rietveld fit method (FullProf software [15]), the unit-cell-parameters and the tellurium and bismuth coordinates were refined. Two – phased simulation was carried on, the contribution of the initial and metastable phases was 6.2 % and 93.8 %, respectively. The factor of the reliability of the structure determining is R_{Bragg} ~ 10 % calculated by the positions of diffractional reflections (Fig. 2).

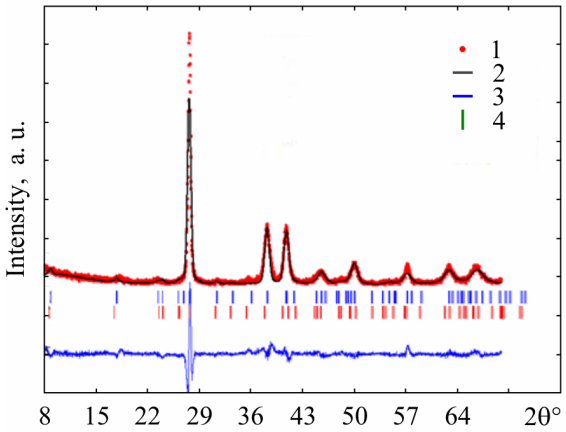

Fig. 2. Results of Rietveld analysis of two – phased Bi_2Te_3 pattern.

The *Te – Te* distance changes dramatically (from 4.54 Å to 3.15 Å) (Table 2) and become closer to the covalent bond *Te – Te* (sum of covalent radii of *Te*, 2.74 Å), which testifies the strengthening in the covalent bond of the metastable *Bi_2Te_3-m* modification.

Microhardness of the new metastable phase was measured and equals to (1.5 ± 0.2) GPa, which is almost identical with the hardness of the initial phase (*H* = 1.7 GPa).

The thermal properties of *Bi_2Te_3-m* were studied by a DSC 800° scanning calorimeter (PerkinElmer). The measurements were carried out during heating at a 20 °C/min speed in the 50 ÷ 380 °C temperature range. When heated, the release of heat was found (Fig. 4 *a* "First run"

curve) after 80 °C (exothermic effect), the intensity of which increases with the temperature rise up to 230 °C. The exothermic effect gradually reduces after 230 °C. "Second run" (Fig. 3) curve shows that there is no exothermic effect in the sample and Bi_2Te_3 (I) is stable at these temperatures. It means that Bi_2Te_3-*m* phase is stable up to 80 °C and the reverse transition stops at 230 °C.

Table 2

Coordinates of the atoms and distances between them in Bi_2Te_3 (I) and Bi_2Te_3-m

Phase	Element	*x*	*y*	*z*	Ionic radius, Å	Covalent radius, Å	Atomic radius, Å	Atoms	Distances, Å
Bi_2Te_3 (I)	Bi_1	0	0	0.40	1.60	1.46	1.70	$Bi_1 - Te_1$	3.07
	Te_1	0	0	0.79	1.40	1.37	1.60	$Te_2 - Te_2$	3.65
	Te_2	0	0	0				$Bi_1 - Te_2$	3.26
Bi_2Te_3-*m*	Bi_1	0	0	0.20				$Bi_1 - Bi_2$	3.15
	Bi_2	0	0	0.59				$Bi_1 - Te_1$	3.36
	Te_1	0	0	0.79				$Bi_2 - Te_2$	3.32
	Te_2	0	0	0				$Te_3 - Te_2$	3.15
	Te_3	0	0	0.39				$Te_3 - Te_1$	3.21

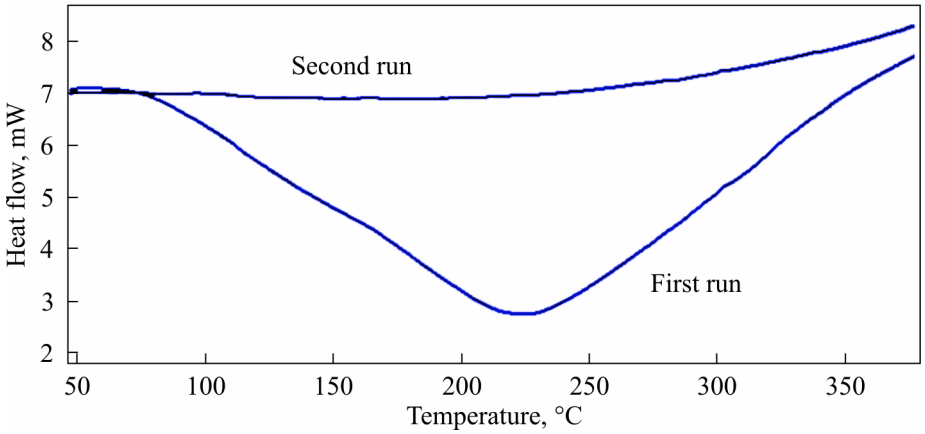

Fig. 3. The reverse Bi_2Te_3-m → Bi_2Te_3 (I) transition.

The Seebeck coefficient (α), electric conductivity (σ) and thermal conductivity (κ) were measured by the Harman method (direct method for obtaining the figure of merit (*ZT*) of a material) [16] (Table 3). The significant decreasing of the *ZT* coefficient in Bi_2Te_3-*m* (*n*-type sample) was obtained.

Table 3

The thermoelectric properties of Bi_2Te_3-m and Bi_2Te_3 (I)

(All data is given at temperature 300 K)	Bi_2Te_3 (I)	Bi_2Te_3-*m*
α, μV/K	(274 ± 14)	(72 ± 4)
σ, 1/(Ω·cm)	(1100 ± 60)	(850 ± 40)
κ, W/(m·K)	(1.45 ± 0.07)	(2.06 ± 0.1)
Z, (10^{-3}1/K)	(1.8 ± 0.2)	(0.25 ± 0.03)

We can conclude that the Bi_2Te_3-*m* metastable phase appears during the high-pressure – high-temperature treatment. The MA process only activates the phase transition, because the pressure created by planetary mill is not enough for a complete transformation. Additives of Bi_2Te_3-*m* could both increase and decrease the thermoelectric power of the bulk materials, because *ZT* is not an additive value. During the phase transition, the symmetry changes (the center of symmetry is lost), a layered structure is retained. The phase transition also changes the alternation of the atomic layers (-*Bi-Te-Te-Te-Bi*-). It should be noted that Bi_2Te_3-*m* is stable at normal conditions and has rhombohedral structure in contrast with the pressure – induced reversible phases of Bi_2Te_3 obtained *in situ* at room temperatures [5, 6, 7]. Such a low value of *ZT* in Bi_2Te_3-*m* could be explained by increasing of the covalent bonding between *Te* atoms.

Conclusions

A Bi_2Te_3-*m* metastable phase was obtained by a direct high-pressure – high-temperature synthesis of the separate elements mixed stoichiometrically at 7.7 GPa and 700 °C. Pre-MA of the Bi_2Te_3 (I) powder allows to fabricate a compact material with a 100 % Bi_2Te_3-*m* outcome at a lower pressure 5.5 GPa and temperature 600 °C. This phase is stable under normal conditions and differs from all the other pressure-induced phases of Bi_2Te_3 obtained by authors of [5-7]. The Bi_2Te_3-*m* structure was refined; the positions of the atoms in the metastable structure were determined. The hardness (1.7 GPa) of Bi_2Te_3-*m* is the same as the Bi_2Te_3 (I) values within the limits of experimental error. The volume change is 0.6 %, i.e. metastable phase is denser than initial phase. The Bi_2Te_3-*m* phase is stable up to 80 °C at the atmospheric pressure. The value of figure of merit of the metastable phase is lower than that of the initial one and equals to $(0.25 \pm 0.003)\cdot 10^{-3}$ K. The new phase is characterized by semimetal properties, which could lead to decreasing in *ZT* coefficient.

Acknowledgements. This research was supported by Russian Federation Ministry of Education and Science (Grant No 16.523.11.3002). Authors would like to thank A. Sorokin for measuring Seebeck coefficient, thermo- and electroconductivity.

References

1. S.V. Ovsyannikov, V.V. Shchennikov, and G.V. Vorontsov, Giant Improvement of Thermoelectric Power Factor of Bi_2Te_3 Under Pressure*, J. Appl. Phys*. **104**, 053713 (2008).
2. M.K. Jacobsen, S.V. Sinogeikin, R.S. Kumar, and A.L. Cornelius, High Pressure Transport Characteristics of Bi_2Te_3, Sb_2Te_3, and $BiSbTe_3$, *J. Phys. Chem. Solids* **73**, 1154 – 1158 (2012).
3. L.G. Khvostantsev, A.I. Orlov, N.Kh. Abrikosov, T.E. Svechnikova, and S.N. Chizhevskaya, Thermoelectric Properties and Phase Transitions in Bi_2Te_3 Under Hydrostatic Pressure up to 9 GPa and Temperature up to 300 °C*, Phys. Status Solidi A* **71**, 49 – 53 (1982).
4. S.J. Zhang, J.L. Zhang, X.H. Yu, J. Zhu, P.P. Kong, S.M. Feng, Q.Q. Liu, L.X. Yang, X.C. Wang, L.Z. Cao, W.G. Yang, L. Wang, H.K. Mao, Y.S. Zhao, H.Z. Liu, X. Dai1, Z. Fang, S.C. Zhang, and C.Q. Jin, The Comprehensive Phase Evolution for Bi_2Te_3 Topological Compound as Function of Pressure, *J. Appl. Phys*. **111**, 112630 (2012).
5. M. Einaga, A. Ohmura, A. Nakayama, F. Ishikawa, Y. Yamada, and S. Nakano, Pressure-Induced Phase Transition of Bi_2Te_3 to a bcc Structure*, Phys. Rev. B* **83**, 092102 (2011).
6. A. Nakayama, M. Einaga, Y. Tanabe, S. Nakano, F. Ishikawa, and Y. Yamada, Structural Phase Transition in Bi_2Te_3 Under High Pressure*, High Pressure Research* 29 (2), 245 – 249 (2009).

7. R. Vilaplana, O. Gomis, F.J. Manjon, A. Segura, E. Perez-Gonzalez, P. Rodrıguez-Hernandez, A. Munoz, J. Gonzalez, V. Marın-Borras, V. Munoz-Sanjose, C. Drasar, and V. Kucek, High-Pressure Vibrational and Optical Study of Bi_2Te_3, *Phys. Rev. B* **84**, 104112 (2011).
8. A. Polian, M. Gauthier, S.M. Souza, D.M. Triches, J. Cardoso de Lima, and T.A. Grandi, Two-Dimensional Pressure-Induced Electronic Topological Transition in Bi_2Te_3, *Phys. Rev. B* **83**, 113106 (2011).
9. M.A. Ilyina, E.S. Itskevich, Superconductivity of Bismuth Telluride, *Sov. Phys. Solid State* **13**, 2098 – 2100 (1972).
10. L. Zhu, H. Wang, Y. Wang, Jian Lv, Ya. Ma, Q. Cui, Y. Ma, and G Zou, Substitutional Alloy of *Bi* and *Te* at High Pressure, *Phys. Rev. Lett*. **106**, 145501 (2011).
11. E.Ya. Atabaeva, E.S. Itskevich, S.A. Mashkov, S.V. Popova, and L.F. Vereschagin, Bismuth Telluride Polymorphism Under High Pressures and Temperatures, *Sov. Phys. Solid. State* **10**, 43 (1968).
12. S.G. Buga, N.R. Serebryanaya, G.A. Dubitskiy, E.E. Semenova, V.V. Aksenenkov, V.D. Blank, Structure and Electrical Properties of Sb_2Te_3 and $Bi_{0.4}Sb_{0.6}Te_3$ Metastable Phases Obtained by HPHT Treatment, *High Pressure Research* **31** (1), 86 – 90 (2011).
13. M. Zakeri, M. Allahkarami, Gh. Kavei, A. Khanmohammadian, and M.R. Rahimipour, Synthesis of Nanocrystalline Bi_2Te_3 via Mechanical Alloying, *J. Mat. Proc. Techn*. **209**, 96 – 101 (2009).
14. F. Yu, B. Xu, J. Zhang, D. Yu, J. He, Zh. Liu, and Yo. Tian, Structural and Thermoelectric Characterizations of High Pressure Sintered Nanocrystalline Bi_2Te_3 Bulks, *Mat. Res. Bull*, **47**, 1432 – 1437 (2012).
15. J. Rodriguez – Carvajal, Recent Developments of the Program FULLPROF, in *Commission on Powder Diffraction (IUCr) Newsletter* **26**, 12 (2001).
16. T.M. Tritt, *Recent Trends in Thermoelectric Materials I*, (2001), pp. 45 – 47.

Submitted 11.06.2013.

V.V. Shchennikov, I.V. Korobeynikov, N.V. Morozova

Institute of Metal Physics of Russian Academy of Sciences, Urals Division,
18, S. Kovalevskaya Str., Yekaterinburg, 620990, Russia

INFLUENCE OF PHYSICAL AND "GEOMETRICAL" FACTORS ON THE PROPERTIES OF THERMOELECTRIC MATERIALS

In the present work, the ways to improvement of thermoelectric parameters are considered based on exploring both physical and "geometrical" factors. The experimental results on the influence of pressure and magnetic field on thermoelectric properties for a wide range of materials are analyzed. Experimental data are obtained in the pressure range of 0 – 30 GPa using an automated setup with the sintered diamond anvils, and the measurements of the thermo-magnetic Nernst-Ettingshausen effect are carried out using an autonomous version of the diamond anvils cell. The approach has been developed for the calculations of the above mentioned effects for inhomogeneous thermoelectric materials. The results of calculations are found to be in good agreement with the experimental data obtained in the vicinity of semiconductor-metal phase transition. It is shown that both physical and "geometrical" factors can improve the power factor of materials.
Key words: Nernst-Ettingshausen effect, Seebeck effect, high-pressure, multi-phase materials.

Introduction

The basic parameters characterizing performance of thermoelectric (TE) converters are the power factor, and the figure of merit:

$$æ = \frac{S^2}{\rho}, \qquad Z = \frac{S^2}{\rho \cdot \lambda}, \tag{1}$$

depending on the thermopower S, the electrical resistivity ρ, and the thermal conductivity $\lambda = \lambda_e + \lambda_{ph}$ consisting of electron (λ_e) and phonon (λ_{ph}) contributions. All the parameters depend on semiconductor gap E_g. The ways to improvement of the above thermoelectric parameters are considered based on exploring both physical factors including high pressure and magnetic fields and "geometrical" factors, like configuration and concentration of discrete elements of multi-phase thermoelectric material.

Experimental details and results

Experimental thermoelectric data were obtained using two automated setups with diamond and hard alloy high pressure anvils [1]. An automated high-pressure setup made it possible to measure simultaneously the force applied, the sample thickness, anvil temperature, thermal gradient ΔT, and electrical signal from the sample [2-3].Temperature distribution in the anvils for various sample sizes and thermal conductivities [2-3] was used for estimation of error in the determination of ΔT along the sample. The measurements of thermomagnetic Nernst-Ettingshausen (N-E) effect were performed using miniature versions of high-pressure chambers with sintered diamond anvils in the stationary magnetic field up to $B \sim 2$ T. New results, as well as those published earlier, were considered in the range of pressures up to ~ 40 GPa.

Influence of physical factors on the thermoelectric parameters of materials: high pressure

A typical variation of the electrical resistivity ρ, the thermal conductivity λ and the thermoelectric power S versus a change in forbidden gap E_g is shown in Fig. 1. The dependences reflect the complex behavior of the above values on E_g which is mainly due to variation of the concentration and mobility of charge carriers. As a result, TE parameters æ and Z have the optimal values in the certain range of E_g values (Fig. 1). The above figure explains high TE properties of narrow-gap semiconductors like Bi_2Te_3, $PbTe$, etc. and also serves as an indicator in searching for novel materials for TE applications. At the same time, Fig. 1 shows that variation of E_g either from large values or from zero ones under some exposure may bring the material into the region of optimal values of E_g for thermoelectricity. High pressure seems to be such an exposure due to strong influence on E_g both in the region of structural stability [4] and in the vicinity of phase transition which leads to opening of E_g or its drastic variation.

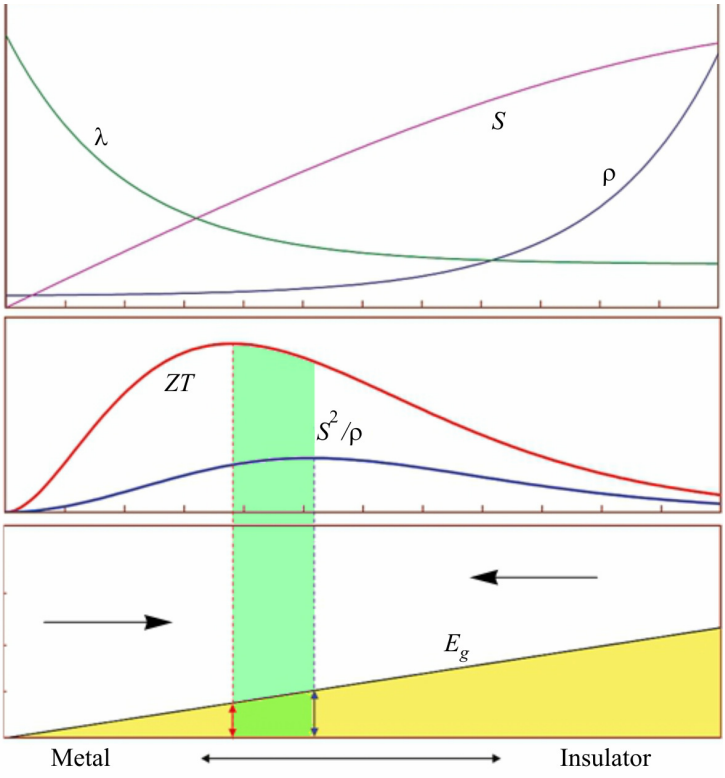

Fig. 1. Dependences of the thermopower (S), the electrical resistivity (ρ), the thermal conductivity (λ), the thermoelectric power factor æ and dimensionless figure of merit (ZT) on the energy gap. The maxima of æ and (ZT) are achieved at some optimal values of a forbidden gap (shown by vertical arrows and by dashed lines). The right and left arrows show that the above optimal values of E_g can be achieved either by decreasing the semiconductor gap (right arrow) or by opening it (left arrow) due to applied pressure.

The pressure dependence of thermoelectric power S can be described by an equation valid for a nearly intrinsic semiconductor [1, 5]:

$$\frac{S}{k/|e|} = \left\{ \sum_i \frac{(\sigma_{pi} - \sigma_{ni})}{\sigma} \times (r+2) + \sum_i \frac{(\sigma_{pi} - \sigma_{ni})}{\sigma} \times \frac{E_g}{2kT} + \frac{3}{4} \times \ln \frac{m_p^*}{m_n^*} + \frac{\Delta E_v}{kT} \times \frac{\sigma_{p2}}{\sigma} \right\}, \qquad (2)$$

where $\sigma = \Sigma(\sigma_{ni} + \sigma_{pi})$ is the total conductivity, $m_p^*(m_n^*)$ is the effective masses of holes (electrons), and r is the scattering parameter of carriers, ΔE_v is the energy difference between the upper and the next bands.

The index "*i*" corresponds to the electron and hole bands, and the index "2" corresponds to the additional hole band, like in Bi_2Te_3 and *PbTe* [5]. The variation of both E_g and ΔE with *P* affects the value of *S*.

The value of *S* corresponds to the average energy transferred by electrons (term ~ E_g) and depends both on the position of the Fermi level (term ~ $\ln(m_p/m_n)$) and on the contribution of second valence band (term ~ ΔE_v).

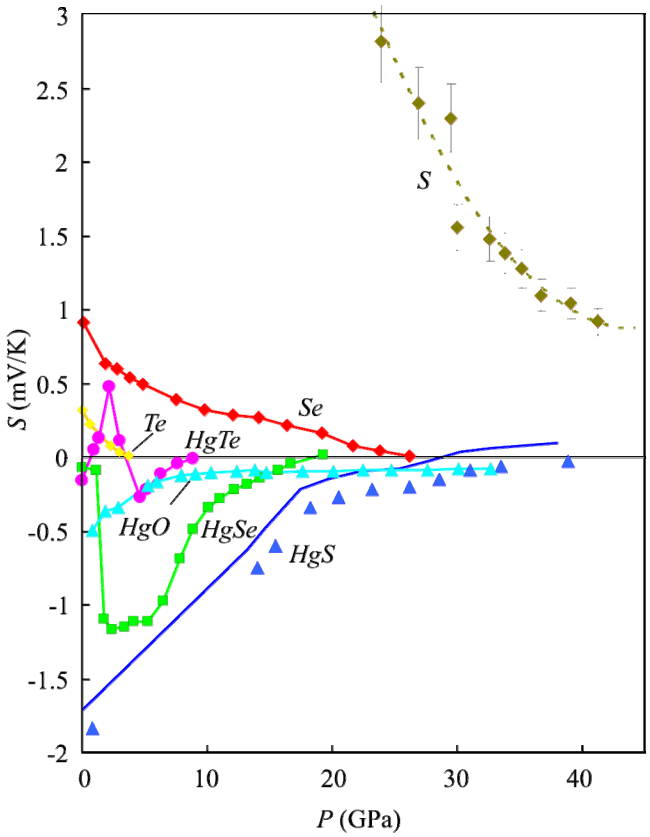

Fig. 2. Thermoelectric power of mercury chalcogenides and chalcogens at very high pressures. The curves virtually demonstrate the variation of energy gaps in a wide range of pressures, since the value of S is proportional to E_g (Eq. 2). The data for HgTe, HgSe, HgS, Te, and Se are taken from [2], the data for HgO are from [6] and for sulphur – from [7].

Fig. 2 shows *S*(*P*) dependence for mercury chalcogenides and chalcogens in a wide pressure range, reflecting the behavior of E_g. For *Te*, *Se*, cinnabar *HgS*, mercury oxide *HgO* and sulphur *S* a strong decrease in *S* was observed under high pressure, testifying to narrowing of E_g (Fig. 2). The first four materials *Te*, *Se*, *HgS* and *HgO* were found to transfer into metal state with closing of E_g [2, 6]. For gap-less semiconductors *HgTe* and *HgSe* the abrupt opening of E_g was established at pressure-induced phase transition from zinc blende to cinnabar structure [2]. With further increase in pressure *P*, the narrowing of E_g and transition to metal state was also found [9]. In Fig. 3, the results of high pressure application are shown for $Sn_2P_2S_{1-x}Se_x$ crystals in the pressure range of 0 – 22 GPa. Under ambient conditions, Sn_2P_2S-based compounds are known to be ferroelectrics with a wide forbidden gap E_g ~ 2.3 eV [8]. The application of pressure strongly decreases the gap E_g and thus causes the drop of electrical resistance by ~ 8 orders of magnitude (Fig. 3). In the pressure range of ~ 15 – 22 GPa the compounds become narrow-gap semiconductors with acceptable thermoelectric properties (Fig. 3). For a basic crystal SnP_2S_6 the closing of E_g and transition to metal state was confirmed by optical measurements [10] near *P* ~ 39.2 GPa. For mixed $Sn_2P_2S_{6-x}S_x$ compounds with small content of *Se* a similar behavior is expected under pressure.

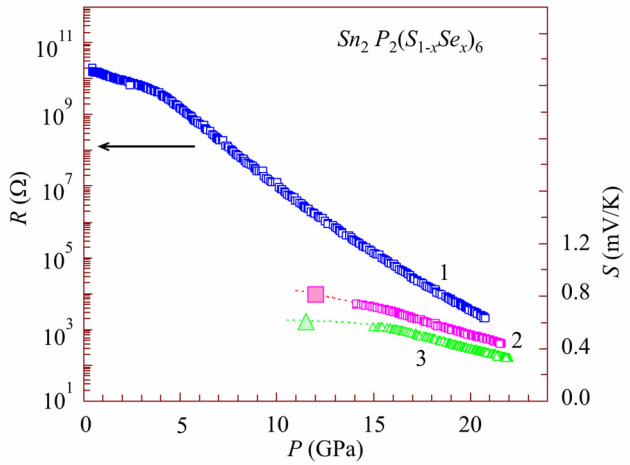

Fig. 3. The pressure dependences of the electrical resistance (1) and the thermoelectric power (2, 3) of $Sn_2P_2(S_{1-x}Se_x)_6$ crystals at room temperature for samples with x = 0.082 (1, 3) and x = 0.092 (2). A series of electronic transitions, starting from a ferroelectric to a paraelectric near ~ 1 GPa, then to a wide-gap semiconductor, and then to narrow-gap semiconductor occurs up at a pressure of 22 GPa. Above ~ 30 GPa the transition to metal state is expected [8].

Thus, it can be noted that the external pressure is really able to bring wide-gap materials into optimal range of E_g for thermoelectricity. The opposite case of opening E_g due to pressure-induced phase transitions for *HgTe* (Fig. 2), *PbTe* and *PbSe* [11] crystals also shows the improvement of thermoelectric properties. The theoretical calculations confirm that high pressure phases of *HgTe* (above ~ 2 GPa), *PbTe* and *PbSe* (above 5 – 6 GPa) are indeed potentially promising thermoelectrics [12-14].

Influence of physical factors on the thermoelectric parameters of materials: magnetic field

The influence of magnetic field on TE parameters is mainly realized due to longitudinal $\Delta S_{\parallel}$ and transverse Q thermomagnetic N-E effects – thermal analogs of magnetoresistance and the Hall effect, respectively [5]

$$\Delta S_{\parallel}(B) = A_2 \times \left(\frac{k}{e}\right) \times (\mu \times B)^2, \tag{3}$$

$$Q = A_3 \times r \times \left(\frac{k}{e}\right) \times \mu, \tag{4}$$

$$Q = \left(\frac{k}{e}\right) a_r \times \left[r\left(\frac{\sigma_n}{\sigma}\mu_n + \frac{\sigma_p}{\sigma}\mu_p\right) + \frac{\sigma_n \sigma_p}{\sigma^2}(\mu_n + \mu_p)\left(2r + 5 + \frac{E_g}{kT}\right) \right], \tag{4a}$$

where e is the electron charge, k is the Boltzmann constant, $\mu = e \times \tau/m$ is the mobility of charge carriers, m is the effective mass, τ is the relaxation time of charge carriers, and r is the scattering parameter describing a dependence of τ on the electron energy ε, $\tau(\varepsilon) \approx \varepsilon^r$. Eq. 4 corresponds to one type of charge carriers, while Eq. 4a – to two types.

Transverse N-E effect Q is proportional to mobility. According to Eqs (3-4), the highest N-E effect ought to arise in materials with the largest mobilities of charge carriers. Combined effect of pressure and magnetic field leads to increasing TE parameters for the pressure-induced states with a negligible direct semiconductor gap. Such states were proved to exist for *Te* and *Se* in the vicinity of

the semiconductor gap closing (Fig. 2) and for *PbTe* and *PbSe* at high pressures near $P \sim 3$ GPa due to decreasing E_g with pressure [15]. Experimental investigations indeed showed a large transverse N-E effect in *Te*, *Se* (Fig. 4) and *PbTe* (Fig. 5) near pressure-induced gap-less states which led to additional increase in power factor (for *PbTe* by ~ 30 % in a magnetic field up to ~ 2 T (Fig. 5)). It would be interesting to test direct-gap $Sn_2P_2S_6$ crystals and compounds on their basis in the vicinity of pressure-induced closing of E_g in the search for strong N-E effects (Fig. 3 and [10]).

Thus, combined application of pressure and magnetic field converts the non-thermoelectric materials like *Te* and *Se* into potential thermoelectric (thermomagnetic) ones. For the known narrow-gap thermoelectric like *PbTe* magnetic field with the simultaneous assistance of high pressure leads to additional increase of TE parameters (power factor, Fig. 5).

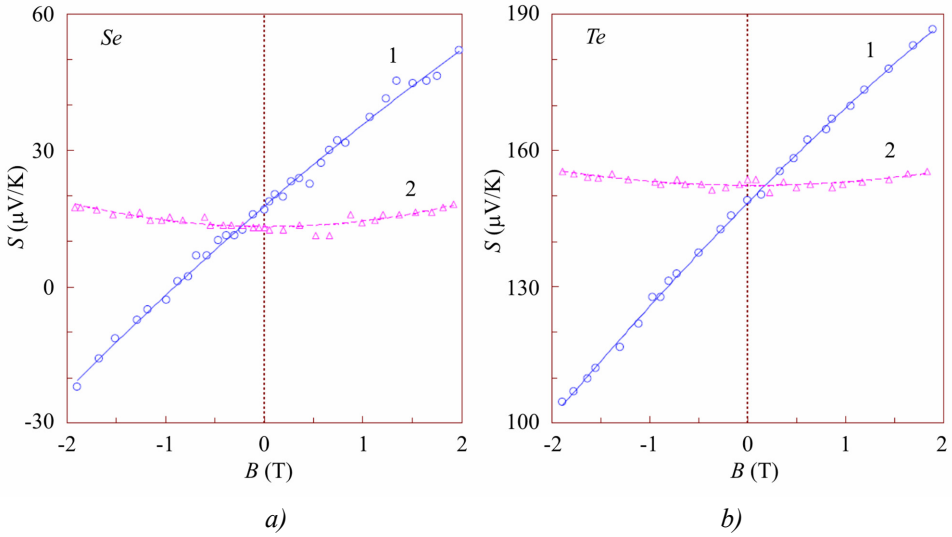

Fig. 4. The magnetic field dependences of thermoelectric power for Se(a), and Te(b) samples in two positions 1 and 2 of high pressure chamber in a magnetic field at fixed pressure, GPa: (a) P = 13.6 GPa; (b) P = 1 GPa.[16]. Position 1 corresponds to transverse N-E effect (Eq. 4), while position 2 – to longitudinal one (Eq. 3). For PbTe samples the similar dependences were obtained and used in the calculation of power factor (see Fig. 5 below).

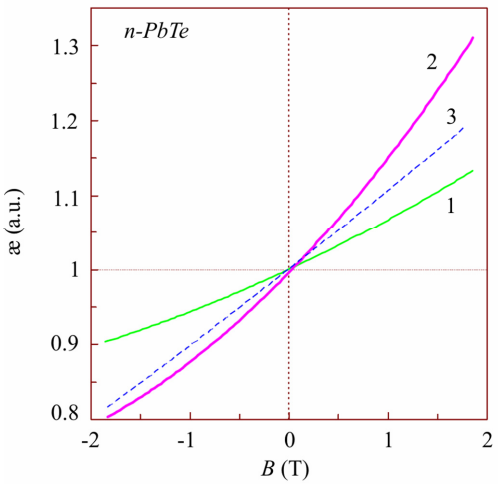

Fig. 5. The dependences of a relative change in the thermoelectric power factor æ on magnetic field B, æ(P;B)/æ(P;B = 0) for a single crystal of n-PbTe at fixed pressures P: 1 – P = 2.0 GPa, $S_0 = S(B = 0) = -190$ μV/K; 2 – P = 3.2 GPa, $S_0 = -127$ μV/K; 3 – P = 4.5 GPa, $S_0 = -79$ ΔV/K[17].

Influence of "geometrical factors" on the thermoelectric parameters of materials

Usually, one can determine experimentally only the generalized characteristics of material (averaged over the total volume of substance measured). These effective properties comprise "geometrical" parameters of every phase: concentration, shape, and position of inclusions [18]. Effective properties of materials (thermal, magnetic, mechanical, etc.) are calculated mostly by two main approaches: in the first one local properties of system are supposed to be known functions of coordinates, and in the second one they are considered statistically as random fields [19].

In the authors' model, the effective electrical resistivity ρ or the electrical conductivity σ (and the thermal conductivity) are considered as normalized sums of phase contributions in two equivalent considerations of "series" and "parallel" electrical (thermal) connection of phases [20, 21]

$$\rho = \sum c_i \rho_i g_i(\rho) \left(\sum c_i g_i(\rho)\right)^{-1}, \tag{5}$$

$$\sigma = \sum c_i \sigma_i g_i(\sigma) \left(\sum c_i g_i(\sigma)\right)^{-1}, \tag{6}$$

where a sum of phase concentrations c_i is equal to 1 and configuration parameters g_i along electrical (thermal) current are of the form:

$$g_i(\rho) = 3/\left[A\rho + (3-A)\rho_i\right] \quad g_i(\sigma) = 3/\left[A\sigma_i + (3-A\sigma)\right] \tag{7}$$

When parameter A equals 0, 3 or 1, the Eq. 5 – 6 agree with the cases of parallel and series electrical connections, or with the case of spherical inclusions, respectively [20-23]. Intermediate values of A ($0 < A < 3$) correspond to interpolated configuration of inclusions in a certain direction (like elongated or contracted ellipsoids).

Unlike the majority of previous models [18, 22, 23] where a shape of inclusions was fixed, in the present model [20] a configuration parameter of phase inclusions is variable between the limiting cases of parallel and series (electrical, thermal) connections. The second distinct advantage of the model is a simultaneous consideration of more than one property of inhomogeneous material.

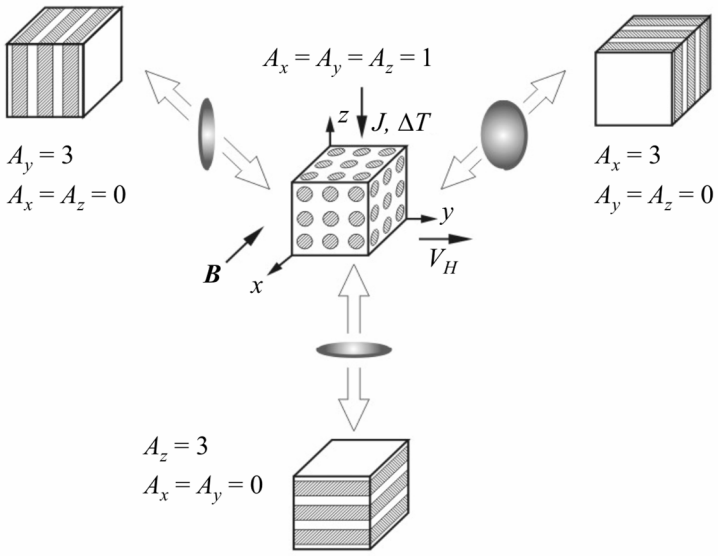

Fig. 6. Examples of materials with the boundary configurations of phase inclusions (planes and spheres). The black arrows show directions of electrical current J (thermal gradient ΔT), magnetic field B and the resulting voltage V_H of the transverse N-E and Hall effects. Parameter A_i along different axes is given for the fixed limiting cases. The intermediate values of A < 1 correspond to elongated ellipsoids, while the values of A > 1 correspond to oblate ones.

As is evident (5) – (7), for the description of effective properties of phase mixture with an arbitrary configuration of inclusions the well-known formulas for parallel and series connection of elements can be used:

$$\sigma^{\parallel} = \sum_{i=1}^{n} \sigma_i c_i \ , \ \sigma^{\perp} = \left(\sum_{i=1}^{n} \frac{\sigma_i}{c_i} \right)^{-1} , \tag{8}$$

on the assumption that voltages (in the first case) and currents (in the second case) for each phase comprise additional multipliers G_i being a function of concentration and configuration of inclusions: $G_i(\rho) \equiv G_i$ and $G_i(\sigma)$

$$G_i = g_i (\sum c_i g_i)^{-1} , \tag{9}$$

$$G_i(\sigma) = g_i(\sigma) \cdot (\sum c_i g_i(\sigma))^{-1} . \tag{10}$$

This approach allows obtaining algebraic formulas for complex properties depending on the vectors of electrical, thermal and magnetic fields directed along the different axes [21]. The application of the approach for the calculation of the electric, thermal, mechanical and magnetic effects is shown below. Interpolation of formula for S obtained in [24, 25] for spherical inclusions to the above simplest limiting cases yields the following equation [20] for a varied configuration of inclusions:

$$S = (\sum S_i c_i g_i(\rho) g_i(\lambda)) / (\sum c_i g_i(\rho) g_i(\lambda)). \tag{11}$$

Eq. (5), (6) and (11) imply a simple relation for the electrical and thermal values of a two-phase system derived for the first time in [20]:

$$\frac{S - S_2}{S_1 - S_2} = \frac{(\rho\lambda - \rho_2\lambda_2)}{(\rho_1\lambda_1 - \rho_2\lambda_2)} . \tag{12}$$

It is interesting that Eq. 12 allows estimating thermoEMF for any system (including modern nano-structures) without cumbersome numerical calculations taking into account certain configuration and concentration of inclusions. The only values required are the effective resistivity and the effective thermal conductivity of the system determined by Eq. 5 and Eq. 6 and the corresponding values of ρ, S and λ for the initial phases. In Fig. 7, the calculated dependences of electrical resistivity and thermoEMF on the concentration of one phase (Eqs. 5, 6), as well as the dependence between them (Eq. 12) are shown for a two-phase system with a variable configuration parameter. The Eq. 12 fits well the experimental data for the materials undergoing semiconductor-metal transitions under pressure or temperature variation [20].

Later in the framework of the model (Fig. 6) a more regular equation for S was obtained [20], to correct the case of spherical inclusions [24, 25]

$$S = (\sum_i S_i \cdot c_i \cdot f_i \cdot (\rho) \cdot \lambda_i^{-1} \cdot f_i(\lambda)) / (\sum_i c_i \cdot f_i \cdot (\rho) \cdot \sum_i c_i \cdot \lambda_i^{-1} \cdot f_i(\lambda)) . \tag{13}$$

For two-phase statistically inhomogeneous materials the equation for S was also obtained in [26], and compared to the equations obtained in [24, 25] for the case of spherical inclusions. For certain binary mixtures the difference between the calculated values of S obtained by these equations (Eq. 11 at $A = 1$) and the equation derived in [26] was estimated to be rather appreciable [26], so correction of Eq. 11 seems to be quite appropriate.

Using Eq. 13 leads to some deviation from the relation (12), especially in the vicinity of the

abrupt change in the properties (near phase transition point), in the case when the thermal conductivities λ_i of phases sufficiently differ. However, for nearly similar thermal conductivities of different phases (components of multi-phase system) Eq. 12 remains sufficiently valid. Due to a wide use of inhomogeneous materials (grain-oriented, textured alloys, etc) in thermoelectricity [27] the relation (12) seems to be useful for the prediction of their properties and, thus, for the development of complex thermoelectric materials.

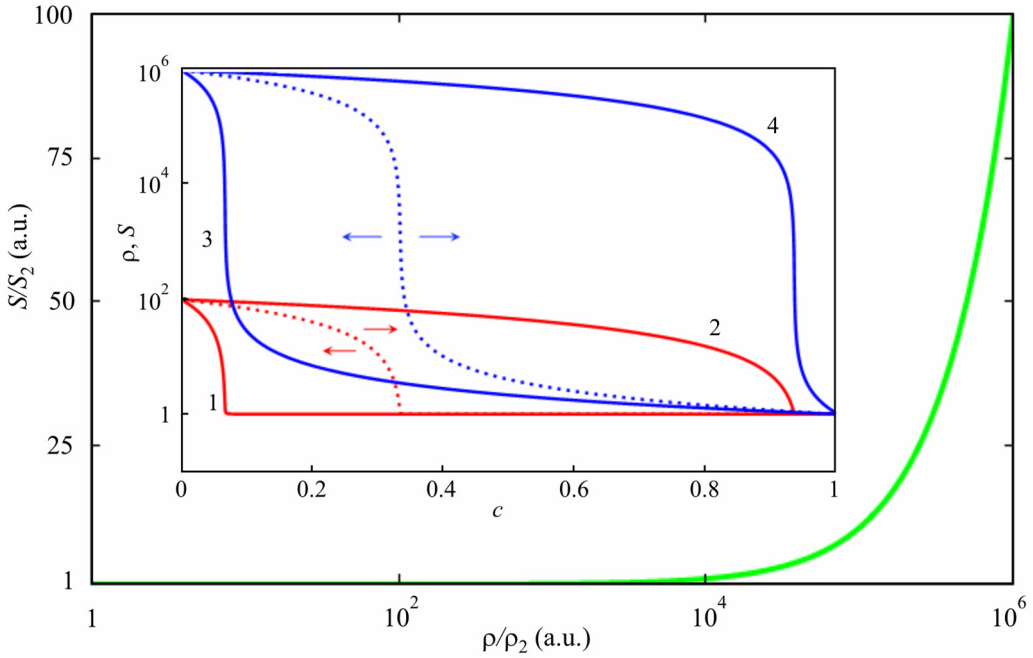

Fig. 7. The relation between the thermopower (S) and the electrical resistivity (ρ) of a two-component system corresponding to Eq. 12 (The parameters of phases taken are as follows $S_1 = 10^2$, $S_2 = 1$, $\rho_1 = 10^6$, $\rho_2 = 1$ a.u.). On the insert, the calculated dependences $S = S(c_1)$ (curves 1 – 2) and $\rho = \rho(c_1)$ (curves 3-4) of a two-component heterophase system on concentration c_1 of component I are shown. Curves 1 and 3 represent the case of A = 0.2 ("nearly parallel" connection) and curves 2 and 4 – A = 2.8 ("nearly series" connection). Dashed curves represent the dependences for parameter A = 1. Arrows show a displacement of the above dependences with increase or decrease in constant A. The drastic drop of thermopower and resistivity values occurs near the concentration c = A/3 of the "metallic" component according to Eqs. 5 and 11.

Developing this model for the transverse N-E effect Q and the Hall effect R for a hetero-phase system, one can obtain [21]:

$$R = \frac{\sum_i c_i \cdot R_i \cdot g_i^J(\sigma) \cdot g_i^H(\rho)}{\left(\sum_i c_i \cdot g_i^J(\sigma)\right) \cdot \left(\sum_i c_i \cdot g_i^H(\rho)\right)}, \quad Q = \frac{\sum_i c_i \cdot Q_i \cdot g_i^T(\lambda) \cdot g_i^H(\rho)}{\left(\sum_i c_i \cdot g_i^T(\lambda)\right) \cdot \left(\sum_i c_i \cdot g_i^H(\rho)\right)}, \tag{14}$$

where g_i^T (g_i^J) and g_i^H are configuration parameters of inclusions along thermal gradient ΔT (current J) and along the Hall direction V_H (perpendicular to magnetic field B), respectively. The parameters A_i are can be varied between the limiting cases of inclusions. Equations (14) coincide with the known formulas for the limiting cases of layered structures [28]. By the way, the equation for Young's modulus was also derived with the use of this model [21], which demonstrated good agreement with the experimental data, including the case of hard alloys in a wide range of component concentrations [29].

Thermoelectric power factor (æ) and thermoelectric figure of merit (Z) of a hetero-phase system

are also functions of concentration and geometrical configuration of inclusions (Fig. 8). Calculations performed using Eqs. 5, 6 and Eq. 13 for some two-phase systems (Fig. 8) show that thermoelectric power factor æ exceeds significantly the values of æ of each component. Losing a little in the thermoelectric figure of merit, one can increase considerably the thermoelectric power factor for "nearly layered" configuration of components (curve 1 in Fig. 8). Note, that at HP-HT synthesis or treatment resulting in production of inhomogeneous materials (grain-oriented, textured alloys, etc), the increase in power factor is really achieved in some cases [27].

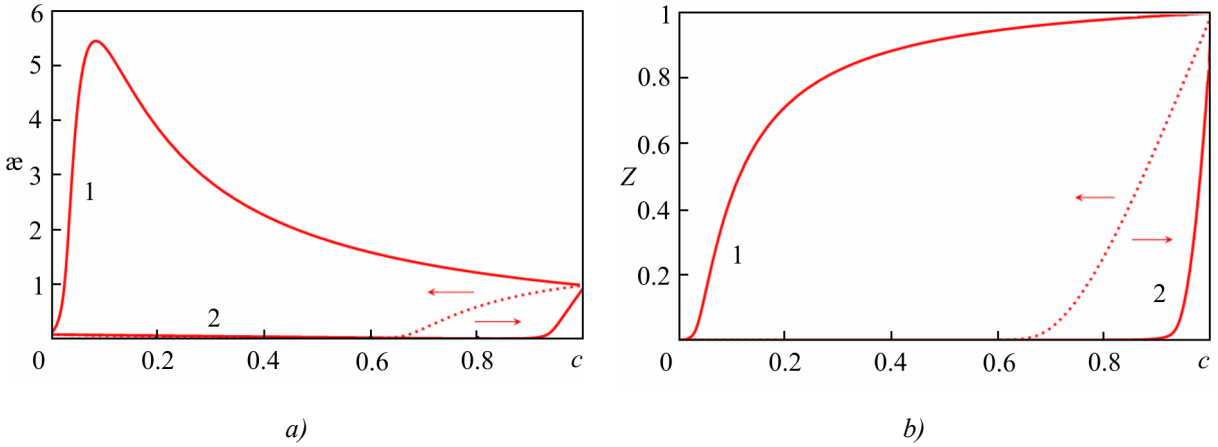

a) *b)*

Fig. 8. Dependence of normalized thermoelectric figure of merit Z (right) and thermoelectric power factor æ *(left) of a two-phase system on concentration c_1 of phase I calculated by Eq. 5, 6 and Eq. 13 ($\lambda_1 = 1$, $\lambda_2 = 100$, $\rho_1 = 10^4$, $\rho_2 = 1$, $S_1 = 100$, $S_2 = 1$ a. u.). The parameter A is taken to be A = 2.9 (curves) 1) and A = 0.2 (curves 2). For dashed curves A = 1. The arrows show a displacement in the dependences with decrease or increase of A.*

Magnetic field can further improve the thermoelectric parameters æ, *Z* characterizing the work of thermoelectric cooling devices, as thermo-magnetic cooling by N-E effect is known to be preferable in comparison with the pure Peltier one [27]. Thus, the approach developed allows to improve working parameters of thermoelectric generators, as well as to take into account the parasitic signals caused by the N-E and Hall effects in operation of electronic devices.

Conclusion

The ways to improvement of thermoelectric parameters through use of physical factors including high pressure and magnetic field, as well as "geometrical" ones including configuration and concentration of discrete elements of a multi-phase thermoelectric material are considered.

High pressure was shown to improve TE parameters of some substances due to variation of semiconductor gap E_g in a wide range, and the narrowing or opening of E_g. Certain non-TE materials, as well as high-pressure phases were found to be promising thermoelectrics.

A combined effect of high pressure and magnetic field is capable of improving TE parameters of substances in pressure-induced narrow-gap and gap-less states with very high mobilities of charge carriers and strong N-E effects.

Variation of the concentration and configuration of discrete elements of a multi-phase system seems incapable of improving the figure of merit by simple "mixing" of phases, but the power factor can strongly increase due to optimal choice of "geometrical" factors.

Acknowledgments. The work was done within RAS Program (Project no. 01.2.006 13394), by UD RAS as part of Program ''Matter at high energy densities'' of the Presidium of RAS (project 12-P-2-1004), by the Ministry of Education and Science of the Russian Federation (Contract 14.518.11.7020), and by the Oriented Basic Research Project of the Ural Branch of the Russian Academy of Sciences.

References

1. V.V. Shchennikov, S.V. Ovsyannikov, and A.Y. Manakov, Measurement of the Seebeck Effect (Thermoelectric Power) at High Pressure up to 40 GPa, *J. Phys. Chem. Solids* **71**, 1168 – 1174 (2010).
2. I.M. Tsidil'kovskii, V.V. Shchennikov, and N.G. Gluzman, Thermoelectric Power of Mercury Chalcogenides at Very High Pressures, *Semiconductors* **17**, 604 – 606 (1983).
3. V.V. Shchennikov, S.V. Ovsyannikov, Phase Transitions from Mechanical Contraction: Direct Observation of Phase-Transition-Related Volumetric Effects in Crystals of *ZnO*, *GaAs*, $CaCO_3$, and *CeNi* under Compression up to 25 GPa, *High Pressure Res*. **29**, 514 – 519 (2009).
4. W. Paul, D.M. Warshawer, *Solids under Pressure* (New York, McGraw-Hill, 1963), 524.
5. B.M. Askerov, *Electron Transport Phenomena in Semiconductors* (Singapore, World Scientific, 1994), 416.
6. I.M. Tsidil'kovskii, V.V. Shchennikov, and N.G. Gluzman, Influence of Ultrahigh Pressures on the Electrical Properties of Mercury Oxide, *Semiconductors* **19**, 901 – 902 (1985).
7. V.V. Shchennikov, S.V. Ovsyannikov, Thermoelectric Power of Sulphur at High Pressure up to 40 GPa, *Phys. Status Solidi (b)* **239**, 399 – 404 (2003).
8. V.V. Shchennikov, N.V. Morozova, I. Tyagur, Y. Tyagur, and S.V. Ovsyannikov, Colossal Tuning of an Energy Gap in $Sn_2P_2S_6$ under Pressure, *Appl. Phys. Lett*. **99**, 212104 (2011).
9. I.M. Tsidil'kovskii, V.V. Shchennikov, and N.G. Gluzman, Metallization of Mercury Chalcogenides under Ultrahigh Pressures, *Physics of the Solid State* **24**, 1507 – 1511 (1982).
10. S.V. Ovsyannikov, H. Gou, N.V. Morozova, I. Tyagur, Y. Tyagur, and V.V. Shchennikov, Raman Spectroscopy of Ferroelectric $Sn_2P_2S_6$ under High Pressure up to 40 GPa: Phase Transitions and Metallization, *J. Appl. Phys*. **113**, 013511 (2013).
11. S.V. Ovsyannikov, V.V. Shchennikov, Y.S. Ponosov, S.V. Gudina, V.G. Guk, E.P. Skipetrov, and V.E. Mogilenskikh, Application of the High-Pressure Thermoelectric Technique for Characterization of Semiconductor Micro-Samples: *PbX*-Based Compounds, *J. Phys. D: Appl. Phys.* **37**, 1151 – 1157 (2004).
12. S.V. Streltsov, A.Yu. Manakov, A.P. Vokhmyanin, S.V. Ovsyannikov, and V.V. Shchennikov, Crystal Lattice and Band Structure of Intermediate High-Pressure Phase of *PbSe*, *J. Phys.: Condens. Matter* **21**, 385501 (2009).
13. Y. Wang, X. Chen, T. Cui, Y. Niu, Y. Wang, M. Wang, Y. Ma, and G. Zou, Enhanced Thermoelectric Performance of *PbTe* within the Orthorhombic Pnma Phase, *Phys. Rev. B* **76**, 155127 (2007).
14. X. Chen, Y. Wang, T. Cui, Y. Ma, G. Zou, and T. Iitaka, *HgTe*: A Potential Thermoelectric Material in the Cinnabar Phase, *J. Chem. Phys*. **128**, 194713 (2008).
15. V.V. Shchennikov, S.V. Ovsyannikov, A.Yu. Derevskov, Thermopower of Lead Chalcogenides at High Pressures, *Phys. Solid State* **44**, 1845 – 1849 (2002).
16. V.V. Shchennikov, S.V. Ovsyannikov, Thermoelectric and Galvanomagnetic Investigations of VI Group Semiconductors *Se* and *Te* at High Pressure up to 30 GPa, *Solid State Commun*. **121**,

323 – 327 (2002).
17. V.V. Shchennikov, S.V. Ovsyannikov, and A.V. Bazhenov, A Composite High-Pressure Cell with Sintered Diamond Insets for Study of Thermoelectric and Thermomagnetic Properties in a Range up to 30 GPa: Application to *Pr* and *PbTe*, *J. Phys. Chem. Solids* **69**, 2315 – 2324 (2008).
18. B. Makhov, B.Z. Pevzner, Influence of the Type of Structure on the Properties of the Heterophase Materials, *Izv. AN USSR: Inorg. Mater*. **21**, 1599 – 1607 (1985).
19. J. Sandetski, *Mechanics of Composite Materials* (New York and London, Academic Press, 1974).
20. V.V. Shchennikov, ThermalEMF and Electrical Conductivity of Materials in the Region of the Semiconductor – Metal Phase Transition Point, *Phys. Met. Metall*. **67**, 92 – 96 (1989).
21. V.V. Shchennikov, S.V. Ovsyannikov, G.V. Vorontsov, and V.V. Shchennikov Jr., Investigations of Multiphase States in Vicinity of Pressure-Induced Phase Transitions, *Phys. Status Solidi (b)* **241**, 3203 – 3209 (2004).
22. V.I. Odelevskii, Calculation of Overall Conductivity of Heterogeneous Systems, *J. Tech. Phys*. **21**, 667 – 685 (1951).
23. R. Landauer, The Electrical Resistance of Binary Metallic Mixtures, *J. Appl. Phys*. **23**, 779 – 784 (1952).
24. S.V. Airapetyants, Thermoelectric Force and the Additional Thermoconductivity of Statistical Mixture, *J. Tech. Phys*. **27**, 478 – 483 (1957).
25. V. Halpern, The Thermopower of Binary Mixtures, *J. Phys. C: Solid State Phys*. **16**, L217 – L220 (1983).
26. C. Herring, Effect of Random Inhomogeneties on Electrical and Galvanomagnetic Measurements, *J. Appl. Phys*. **31**, 1939 – 1953 (1960).
27. S.V. Ovsyannikov, V.V. Shchennikov, High-Pressure Routes in the Thermoelectricity or How one Can Improve a Performance of Thermoelectrics, *Chem. Mater*. **22**, 635 – 647 (2010).
28. G.N. Dul'nev, V.V. Novikov, *Transfer Processes in Inhomogeneous Media* (Leningrad, Energoatomizdat, 1991), 248.
29. S.V. Ovsyannikov, V.V. Shchennikov, I.A. Komarovskii, G.V. Vorontsov, I.V. Korobeynikov, and V.V. Shchennikov Jr., Electrical and Mechanical Properties of Multi-Phase Systems under External Impacts, *Proc. SPIE 7978*, 79781W (2011).

Submitted 04.06.2013.

L.I. Anatychuk[1,2], R.R. Kobylianskyi[1,2], I.A. Konstantinovich[1,2]

[1]Institute of Thermoelectricity of the NAS and MES Ukraine,
1, Nauky Str., Chernivtsi, 58029, Ukraine;
[2]Yu. Fedkovych Chernivtsi National University, 2, Kotsyubinsky Str.,
Chernivtsi, 58000, Ukraine

THE IMPACT OF A THERMOELECTRIC SUPPLY ON THE ACCURACY OF TEMPERATURE AND HEAT FLUX MEASUREMENT

In this paper, the accuracy of human body temperature and heat flux measurement with a thermoelectric supply on its surface has been studied. For this purpose, physical, mathematical and computer models of biological tissue with a thermoelectric sensor and a thermoelectric supply have been constructed. Object-oriented computer simulation was used to obtain the distributions of temperature and heat fluxes with regard to blood circulation and metabolism of biological tissue. Dependences describing the impact of a thermoelectric supply power and its distance from a thermoelectric sensor on the accuracy of temperature and heat flux measurement have been defined.

Key words: computer simulation, thermoelectric supply, temperature and heat flux sensor.

Introduction

Low-power thermoelectric supplies (10^{-1} W – 10^{-4} W) offer a number of attractive properties, so the possibilities of their application are studied more and more intensively [1-13]. Among them of particular interest are thermoelectric supplies using human heat for their operation. For instance, they are beneficial for the diagnostics of human health status by long-term measurement of temperature and heat fluxes [14-24]. However, if such a supply is arranged sufficiently close to temperature and heat flux sensors, it can affect their readings.

So, *the purpose of this paper* is to study the impact of thermoelectric supplies on the results of measuring temperature and heat fluxes on human skin surface.

A physical model of biological tissue with a thermoelectric sensor and a thermoelectric supply

Such a model is given in Fig. 1. Here, an area of human skin is a structure consisting of three layers (epidermis 1, dermis 2, subcutis 3) and internal tissue 4. This structure is characterized by thermal conductivity κ_i, specific heat C_i, density ρ_i, blood perfusion rate ω_b, blood density ρ_b, blood heat capacity C_b and specific heat release q_{met} due to metabolic processes (Table 1). The respective biological tissue layers 1 – 4 are regarded as the bulk sources of heat q_i, where:

$$q_i = q_{met} + \rho_b \cdot C_b \cdot \omega_i \cdot (T_b - T_i), \quad i = 1..4. \tag{1}$$

T_b is blood temperature, T_i is temperature of the i-th layer of biological tissue. The geometric

dimensions of each layer are designated as a_i, b_i and l_i, and the temperatures at the boundaries of the respective biological tissue layers - as T_1, T_2, T_3 and T_4.

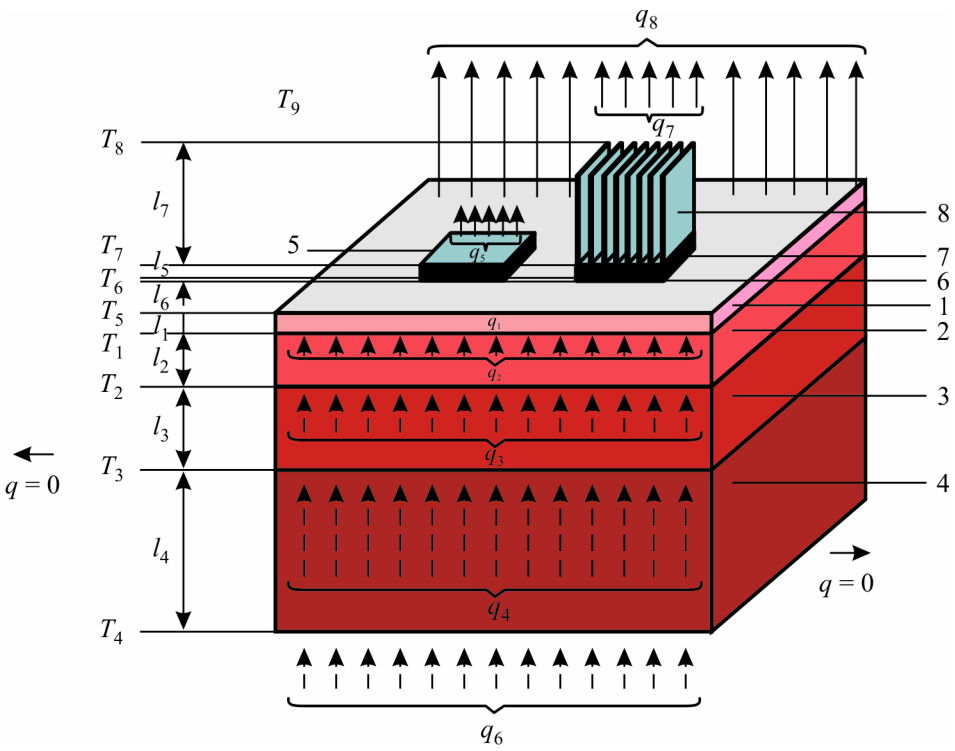

Fig. 1. A physical model of biological tissue with a thermoelectric sensor and a thermoelectric supply: 1 – epidermis, 2 – dermis, 3 – subcutis, 4 – internal tissue, 5 – thermoelectric temperature and heat flux sensor, 6 – heat-leveling plate, 7 – thermoelectric supply, 8 – heat sink.

A thermoelectric temperature and heat flux sensor 5 is a rectangular bar of dimensions a_5, b_5, l_5, consisting of semiconductor thermocouple elements connected into a series circuit and a dielectric package with embedded temperature sensor (thermistor) [25]. The thermoEMF [1, 2] developed by the thermoelectric sensor is given below:

$$E = \alpha \cdot N \cdot \Delta T, \tag{2}$$

where α is the Seebeck coefficient, N is the number of thermoelectric material legs, ΔT is temperature difference between the sensor's upper and lower surfaces. The number of thermoelectric material legs in the temperature and heat flux sensor is $N = 1500 – 3000$ pcs. Simulation of a thermoelectric sensor with such a number of elements is an intricate problem even for modern personal computers. At the same time, from formula (2) it is evident that the sensor's EMF value is mainly influenced by temperature difference ΔT between its surfaces. Therefore, to reach the purpose set in this paper, it is quite sufficient to replace a thermoelectric sensor having a large number of elements by the bulk homogeneous medium of equivalent thermal conductivity κ. Then, on the basis of calculated ΔT, one can easily determine the sensor's EMF and then determine heat flux density according to calibration plots of EMF and heat flux.

The skin surface layer (epidermis 1) of temperature T_5 is in the state of heat exchange with heat-leveling plates 6 of high thermal conductivity material whose geometric dimensions are a_6, b_6, l_6. Let us denote contact surface temperature T_6. Located on the surface of biological tissue (epidermis 1) is a thermoelectric sensor 5 with the geometric dimensions a_5, b_5, l_5 and contact surface temperature

T_7, as well as a thermoelectric supply 7 with the geometric dimensions a_7, b_7, l_7 and contact surface temperature T_8.

Table 1

Thermophysical properties of human biological tissue [26-30]

Biological tissue layers	Epidermis	Dermis	Subcutis	Internal tissue
Thickness, l (mm)	0.08	2	10	30
Specific heat, S ($J \cdot kg^{-1} \cdot K^{-1}$)	3590	3300	2500	4000
Thermal conductivity, κ ($W \cdot m^{-1} \cdot K^{-1}$)	0.24	0.45	0.19	0.5
Density, ρ ($kg \cdot m^{-3}$)	1200	1200	1000	1000
Metabolism, q_{met} ($W \cdot m^{-3}$)	368.1	368.1	368.3	368.3
Tissue blood perfusion rate, ω_b ($m^3 \cdot s^{-1} \cdot m^{-3}$)	0	0.00125	0.00125	0.00125
Blood density, ρ_b ($kg \cdot m^{-3}$)	1060	1060	1060	1060
Blood heat capacity, C_b ($J \cdot kg^{-1} \cdot K^{-1}$)	3770	3770	3770	3770

Free surfaces of the thermoelectric sensor 5 of temperature T_7 and the thermoelectric supply 7 of temperature T_8 are in the state of heat exchange with the environment of temperature T_9 which is taken into account by heat exchange coefficient α_1 and emissivity coefficient ε_1. Specific heat flux from the surface of the thermoelectric sensor 5 to the environment is q_5, from the surface of heat sink 8 to the environment is q_7, from free skin surface – q_8, and specific heat flux of human internal bodies – q_6.

Heat exchange between the skin surface and the environment of temperature T_9 is taken into account by heat exchange coefficient α_2 and emissivity coefficient ε_2. Skin heat exchange due to perspiration is disregarded.

As long as a physical model of biological tissue is a four-layered area, with identical biochemical processes occurring in adjacent layers, it can be assumed that there is no heat overflow along the biological tissue ($q = 0$).

Mathematical description and a computer model

A general equation of heat exchange in biological tissue is as follows [26-30]:

$$\nabla(k \cdot \nabla T) + \rho_b \cdot C_b \cdot \omega_b \cdot (T_b - T) + q_{met} = \rho \cdot C \cdot \frac{\partial T}{\partial t}, \tag{3}$$

where ρ is the density of corresponding biological tissue layer (kg/m^3), C is specific heat of biological tissue layer ($J \cdot kg^{-1} \cdot K^{-1}$), ρ_b is blood density (kg/m^3), C_b is specific heat of blood ($J \cdot kg^{-1} \cdot K^{-1}$), ω_b is blood

perfusion rate ($m^3 \cdot s^{-1} \cdot m^{-3}$), T_b is human blood temperature (°C), where $T_b = 310.15$ K, q_{met} is the specific amount of metabolic heat (W/m^3).

The summand in the right-hand side of equation (3) is the rate of change in thermal energy comprised in the unit volume of biological tissue. Three summands in the left-hand side of this equation are the rate of change in thermal energy due to thermal conductivity, blood perfusion and metabolic heat, respectively.

To solve the problem formulated in this work, it is sufficient to consider a three-dimensional steady-state model. Then equation (3) will acquire the form (4):

$$k \cdot \left(\frac{\partial^2 T}{\partial x^2} + \frac{\partial^2 T}{\partial y^2} + \frac{\partial^2 T}{\partial z^2}\right) + \rho_b \cdot C_b \cdot \omega_b \cdot (T_b - T) + q_{met} = 0. \tag{4}$$

A steady-state equation of heat exchange in biological tissue (4) is solved with the corresponding boundary conditions (5 – 6):

$$\begin{cases} q\big|_{x=0} = 0, \\ q\big|_{x=a} = 0, \end{cases} \quad \begin{cases} q\big|_{y=0} = 0, \\ q\big|_{y=a} = 0, \end{cases} \tag{5}$$

$$\begin{cases} T\big|_{z=0} = 37\ ^\circ\text{C}, \\ q\big|_{z=b,c,d} = \alpha \cdot (T_0 - T) + \varepsilon \cdot \sigma \cdot (T_0^4 - T^4), \end{cases} \quad \begin{cases} q\big|_{x=e,f} = 0, \\ q\big|_{y=e,f} = 0, \end{cases} \tag{6}$$

where q is heat flux density, T is absolute temperature, T_0 is ambient temperature, α is heat exchange coefficient, ε is emissivity coefficient, σ is the Boltzmann constant.

To determine the impact of a thermoelectric supply on the accuracy of temperature and heat flux measurement by a thermoelectric sensor, a three-dimensional computer model of biological tissue having on its top a thermoelectric supply and a sensor was created. For construction of a computer model, the Comsol Multiphysics software package was employed [31], enabling simulation of thermophysical processes in biological tissue with regard to blood circulation and metabolism.

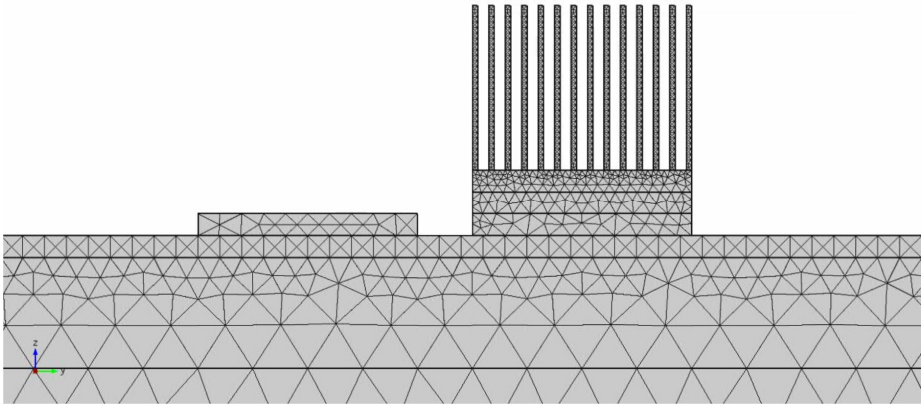

Fig. 2. Finite element method mesh.

The distribution of temperature and heat flux density in human biological tissue, the thermoelectric temperature and heat flux sensor and the thermoelectric supply was calculated by finite element method the essence of which is that an object under study is split into a large number of finite elements (Fig.2), for each of which the value of function is found which satisfies given differential equations of second kind with the respective boundary conditions. The accuracy of solving the

formulated problem depends on the method of splitting and is assured by using a large number of finite elements [31].

Computer simulation results

Object-oriented computer simulation was used to obtain the distributions of temperature (Fig. 3, 4) and heat flux density lines in human biological tissue, the thermoelectric temperature and heat flux density sensor and the thermoelectric supply.

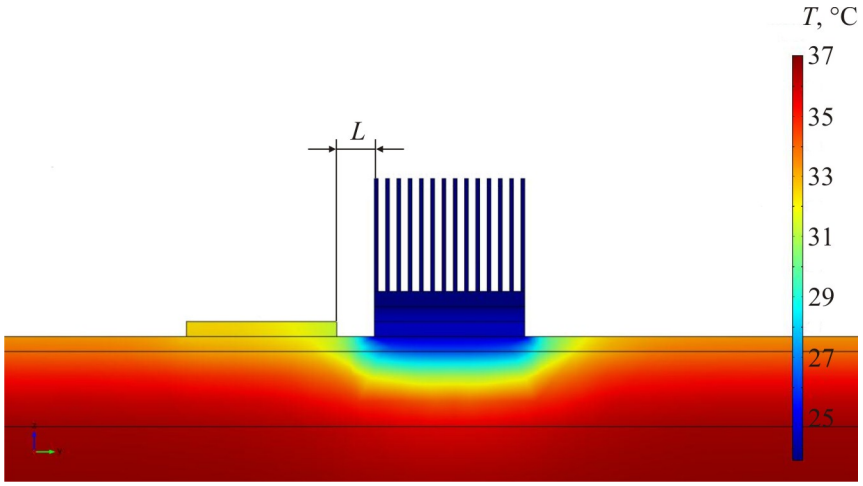

Fig. 3. Temperature distribution in human biological tissue having on its top a thermoelectric temperature and heat flux sensor and a thermoelectric supply for the case of a distance between them L = 0.5 cm and supply power P = 0.6 mW, corresponding to cross-sectional area S = 4 cm^2.

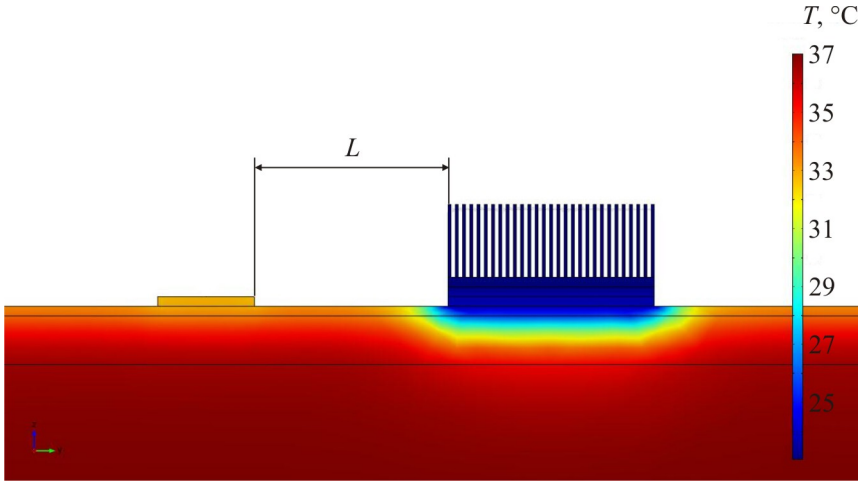

Fig. 4. Temperature distribution in human biological tissue having on its top a thermoelectric temperature and heat flux density sensor and a thermoelectric supply for the case of a distance between them L = 4 cm and the thermoelectric supply power P = 2.23 mW, corresponding to cross-sectional area S = 16 cm^2.

Computer simulation was used to define dependences describing the impact of the thermoelectric supply power and its distance from the thermoelectric sensor on the accuracy of temperature and heat flux measurement (Figs. 5 – 8).

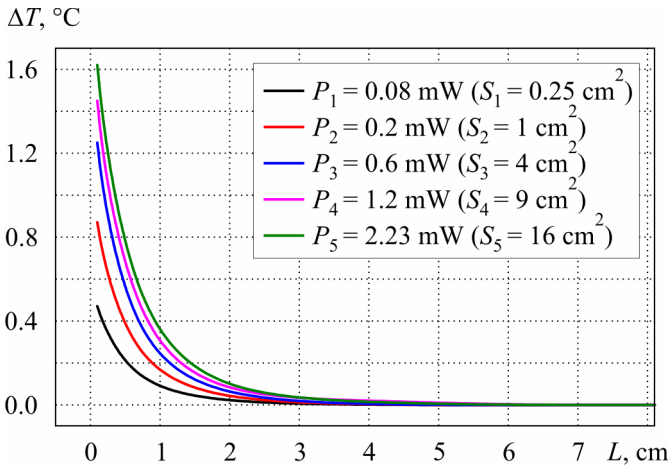

Fig. 5. The error of measuring temperature ΔT versus the distance between the sensor and the thermoelectric supply.

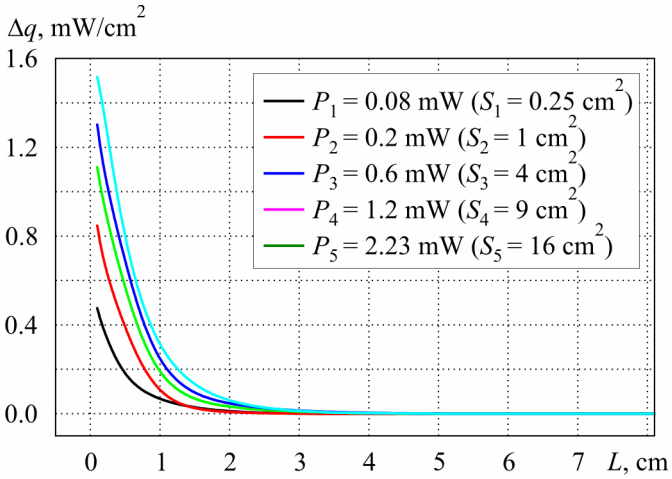

Fig. 6. The error of measuring heat flux density Δq versus the distance between the sensor and the thermoelectric supply.

Calculations have been made for the ambient temperature $T = 20$ °C, the geometric dimensions of the thermoelectric temperature and heat flux sensor (20×20) mm^2 and heat exchange coefficients of the biological tissue, sensor and thermoelectric supply with the environment $\alpha = 10$ W/m^2·K.

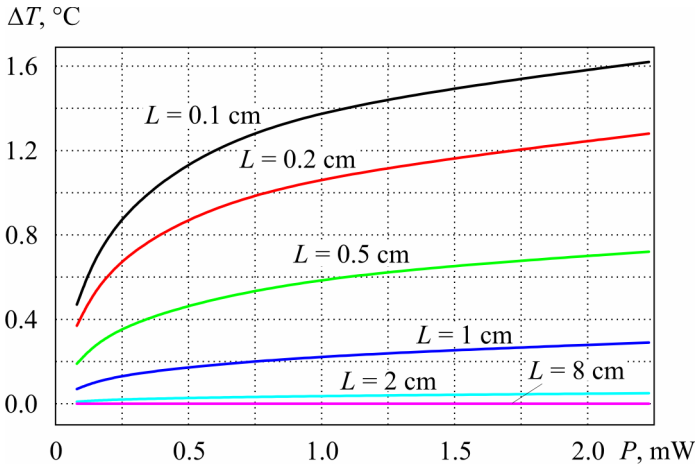

Fig. 7. The error of measuring temperature ΔT versus the thermoelectric supply power.

Figs. 5 – 6 represent dependences showing the impact of the thermoelectric supply distance from the thermoelectric sensor on the errors of measuring temperature ΔT and heat flux density Δq by the thermoelectric sensor.

Figs. 7 – 8 represent dependences showing the impact of the thermoelectric supply power on the errors of measuring temperature ΔT and heat flux density Δq by the thermoelectric sensor.

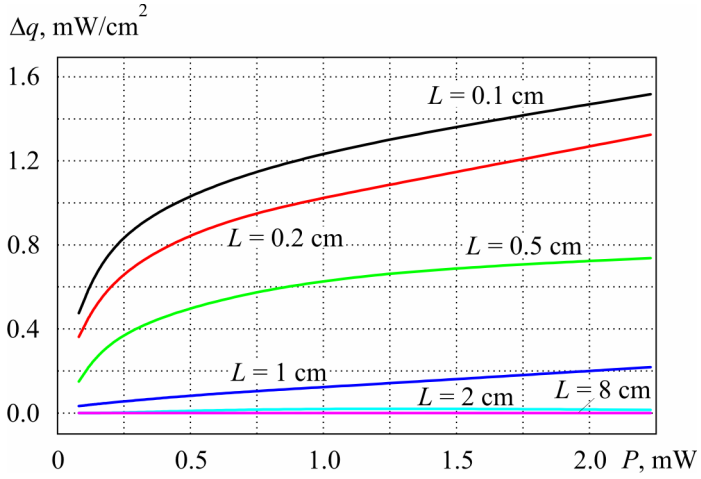

Fig. 8. The error of measuring heat flux density Δq versus the thermoelectric supply power.

From Figs. 5 to 8 it is evident that arrangement of the thermoelectric supply at a distance not less than $L = 5$ cm from the temperature and heat flux sensor leads to measurement errors that do not exceed $\Delta T = 0.01$ °C and $\Delta q = 0.001$ mW/cm^2, respectively. With the arrangement of the sensor and the thermoelectric supply at a distance of $L = 2$ cm, maximum error of temperature measurement is $\Delta T = 0.1$ °C. The above errors of temperature measurement are valid for thermoelectric supplies of power $P = 0.08 \div 2.23$ mW (Fig. 5). Similarly, with the arrangement of the sensor and the thermoelectric supply at a distance of $L = 1$ cm, maximum error of heat flux density measurement is $\Delta q = 0.25$ mW/cm^2, and at the distance of $L = 2$ cm maximum error of heat flux density measurement is $\Delta q = 0.05$ mW/cm^2 (Fig. 6).

Conclusions

1. Object-oriented computer simulation was used to obtain temperature and heat flux distributions in human biological tissue, which afforded an opportunity to determine the impact of the thermoelectric supply on the accuracy of temperature and heat flux measurement by the thermoelectric sensor.
2. Dependences describing the impact of the thermoelectric supply power and its distance from the thermoelectric sensor on the accuracy of temperature and heat flux measurement have been defined. In particular, it has been found that with the arrangement of the thermoelectric supply at a distance not less than $L = 5$ cm from the temperature and heat flux sensor, the errors of temperature and heat flux measurement do not exceed $\Delta T = 0.01$ °C and $\Delta q = 0.001$ mW/cm^2, respectively.

References

1. L.I. Anatychuk, *Thermoelements and Thermoelectric Devices: Handbook* (Kyiv: Naukova Dumka, 1979), 768 p.

2. L.I. Anatychuk, *Thermoelectricity, Vol. 2, Thermoelectric Power Converters* (Kyiv, Chernivtsi: Institute Thermoelectricity, 2003), 376 p.
3. L.T. Strutynska, Thermoelectric Microgenerators. State of the Art and Application Potential, *Tekhnologiya i Konstruirovaniye v Elektronnoi Apparature* **4**, 5 – 13 (2008).
4. Patent US 6222114, Portable Wrist Device, *Mitamura Gen (JP)* (2001).
5. G.J. Snyder, Small Thermoelectric Generators, *The Electrochemical Society Interface. – Fall 2008*.
6. L.I. Anatychuk, R.R. Kobylianskyi, and S.B. Romanyuk, Electronic Medical Thermometer with Thermoelectric Power Source, *XV International Forum on Thermoelectricity (May 21-24, 2013, Tallinn, Estonia)*.
7. L.I. Anatychuk, R.R. Kobylianskyi, and S.B. Romanyuk, *Application № u201308794 of 15.07.13*, Electronic Medical Thermometer with a Thermoelectric Power Source.
8. L.I. Anatychuk, R.R. Kobylianskyi, and S.B. Romanyuk, *Application № u201308793 of 15.07.13*, Electronic Medical Thermometer with a Combined Power Source.
9. L.I. Anatychuk, *Application № u201312570 of 28.10.2013*, Electronic Medical Thermometer with a Thermoelectric Power Source.
10. L.I. Anatychuk, R.R. Kobylianskyi, On the Accuracy of Temperature Measurement by Electronic Medical Thermometer with a Thermoelectric Power Supply, *J. Thermoelectricity* **5**, 68 – 72 (2013).
11. L.I. Anatychuk, R.R. Kobylianskyi, *Patent of Ukraine № 71619*, Thermoelectric Medical Heat Meter, Application № u 2011 14007; filed 28.11.11; publ. 25.07.12, Bul. № 14.
12. P.D. Mykytyuk, R.R. Kobylianskyi, and T.V. Slepenyuk, *Patent of Ukraine № 73037*, Thermoelectric Medical Device, Application № u 2012 01922; filed 20.02.12; publ. 10.09.12, Bul. № 17.
13. Vladimir Leonov, Human Machine and Thermoelectric Energy Scavenging for Wearable Devices, *ISRN Renewable Energy*, Vol. 2011, Article ID 785380, 11 pages (doi:10.5402/2011/785380).
14. R.B. Ladyka, D.N. Moskal and V.D. Didukh, Semiconductor Heat Meters in Arthropathy Diagnostics and Treatment, *Meditsinskaya Tekhnika* **6**, 34 – 35 (1992).
15. R.B. Ladyka, O.N. Dakalyuk, L.P. Bulat and A.P. Myagkota, Use of Semiconductor Heat Meters in the Diagnostics and Treatment, *Meditsinskaya Tekhnika* **6**, 36 – 37 (1996).
16. L.I. Anatychuk, N.G. Lozinsky, P.D. Mykytyuk Yu.Yu. Rozver, Thermoelectric Semiconductor Heat Meter, *Instruments and Experimental Techniques* **5**, 236 (1983).
17. L.I. Anatychuk, L.P. Bulat, D.D. Gutsal and A.P. Myagkota, Thermoelectric Heat Meter, *Instruments and Experimental Techniques* **4**, 248 (1989).
18. B.M. Demchuk, L.Ya. Kushneryk, and I.M. Rublenyk, Thermoelectric Sensors for use in Orthopedics, *J. Thermoelectricity* **4**, 78 – 82 (2002).
19. A.A. Ascheulov, L.Ya. Kushneryk, Thermoelectric Device for Medico-Biological Express-Diagnostics, *Tekhnologiya i Konstruirovaniye v Elektronnoi Apparature* **4**, 38 – 39 (2004).
20. R.R. Kobylianskyi, R.G.Garabazhiv, and T.V.Slepenyuk, On Applications of Thermoelectricity in Medicine, *VII School on Thermoelectricity* (July 16-19, 2012, Yaremche, Ukraine, 2012).
21. L.I. Anatychuk, R.R. Kobylianskyi, Research into the Effect of Thermoelectric Heat Meter on Human Heat Release Measurement, *J. Thermoelectricity* **4**, 59 – 65 (2012).
22. L.I. Anatychuk, R.R. Kobylianskyi, Computer Design of Thermoelectric Heat Meter Readings Under Real-Service Conditions, *J. Thermoelectricity* **1**, 47 – 54 (2013).
23. L.I. Anatychuk, R.G. Giba, and R.R. Kobylianskyi, Some Peculiarities of Using Medical Heat Meters in the Investigation of Local Human Heat Release, *J. Thermoelectricity* **2**, 82 – 88 (2013).
24. L.I. Anatychuk, R.R. Kobylianskyi, Peculiarities of Using Thermoelectric Medical Heat Meters

when Measuring Local Human Heat Release, *XV International Forum on Thermoelectricity* (May 21-24, 2013, Tallinn, Estonia).

25. V.S. Gischuk, Modernized Device for Human Heat Flux Measurement, *J. Thermoelectricity* **2**, 92 – 96 (2013).
26. S.C. Jiang, N. Ma, H.J. Li and X.X. Zhang, Effects of Thermal Properties and Geometrical Dimensions on Skin Burn Injuries, *Burns* 28, 713 – 717 (2002).
27. M.P. Cetingul, C. Herman, Identification of Skin Lesions from the Transient Thermal Response Using Infrared Imaging Technique, *IEEE*, 1219 – 1222 (2008).
28. M. Ciesielski, B. Mochnacki and R. Szopa, Numerical Modeling of Biological Tissue Heating. Admissible Thermal Dose, *Scientific Research of the Institute of Mathematics and Computer Science* 1 (10), 11 – 20 (2011).
29. Florin Filipoiu, Andrei Ioan Bogdan and Iulia Maria Carstea, Computer-Aided Analysis of the Heat Transfer in Skin Tissue, *Proceedings of the 3rd WSEAS Int. Conference on Finite Differences - Finite Elements - Finite Volumes - Boundary Elements*, 2010, p. 53 – 59.
30. Daniela Carstea, Ion Carstea and Iulia Maria Carstea, Interdisciplinarity in Computer-Aided Analysis of Thermal Therapies, *WSEAS Transactions on Systems and Control* 6 (4), 115 – 124 (2011).
31. COMSOL Multiphysics User's Guide, COMSOLAB, 2010, 804 p.

Submitted 09.12.2013.

R.G. Cherkez, M.V. Maksymuk, P.P. Fenyak

Institute of Thermoelectricity of the NAS and MES Ukraine,
1, Nauky Str., Chernivtsi, 58029, Ukraine

DESIGN OF THERMOELECTRIC PERMEABLE STRUCTURES BASED ON *Mg* AND *Mn* SILICIDES

Results of computer design of permeable thermoelements based on Mg and Mn silicides are presented. Optimal concentrations of doping impurities for such materials and optimal thermophysical parameters whereby maximum thermodynamic efficiency of permeable thermoelements is accomplished are determined. The energy characteristics of single- and double-segment permeable thermoelements are calculated under optimal operating conditions for different values of heat carrier temperatures. It is shown that the efficiency of a permeable thermoelement depends on the geometry of legs (the height, the diameter and number of channels) and reaches maximum value of 4 % and 7 % for single- and double-segment variants, respectively.
Key words: computer design, permeable structures, heat recuperators, efficiency.

Introduction

In recent decade, due to growing demand for energy resources, increasing attention has been drawn to the recovery of heat from industry and internal combustion engines via thermoelectricity. The temperature level of such heat sources reaches 700 to 800 K. However, the constraining factor for a wide introduction of thermoelectric recuperators is insufficiently high efficiency of the existing thermoelectric materials. Moreover, the overwhelming majority of thermoelectric materials used nowadays for creation of thermoelectric converters include difficult to obtain and toxic components. With this consideration in mind, development and research on high-performance, cheap, environmentally safe thermoelectric materials and power converters on their basis is a relevant task.

One of the promising methods for efficiency improvement of thermoelectric converters and expansion of their possible practical implementation is to use materials based on *Mg* and *Mn* silicides which meet a number of requirements: low-cost initial components, high mechanical strength and, particularly, environmental safety.

Analysis of known investigations shows that the efficiency of thermoelectric modules made of homogeneous materials based on doped *n-Mg-Si* and *p-Mn-Si* solid solutions at hot side temperature 773K and cold side temperature 320 K is at a level of ~ 4 % [1]. Through use of double-segment structures based on *Mg* and *Mn* silicides the efficiency of modules is increased by a factor of 1.3 to 1.5. In [1] it is shown that the best efficiency values should be expected for *n*-type $Mg_2(Si_{0.3}Sn_{0.7})_{1-x}Sb_x$ and *p*-type $Mn(Al_xSi_{1-x})_{1.8}$ materials.

At the same time, studies on thermoelements where heat inlet and outlet takes place not only through the junction surfaces, but also due to the use of developed heat exchange surface in the bulk of thermoelement legs material have aroused heightened interest of late [2]. In such cases, thermoelements are created that are permeable to gas or liquid fluxes which allows improving the efficiency of thermoelectric energy conversion by 30 % already for the existing low-temperature generator materials based on Bi_2Te_3 [3]. Studies on such permeable thermoelements of promising

materials based on *Mg* and *Mn* silicides have not been performed.

The purpose of this work is calculation and study of the efficiency of permeable generator thermoelements made of optimal materials based on *Mg* and *Mn* silicides.

Physical model and its mathematical description

A physical model of a permeable thermoelement in electric energy generation mode is represented in Fig. 1. The thermoelement is composed of *n*- and *p*-type legs whose physical properties are temperature dependent. Heat input takes place by passing heat carrier along the leg through channels (pores). Each leg consists of N_n and N_p segments, respectively, with connection contact resistance r_0. The lateral surfaces of legs are adiabatically isolated, heat carrier temperature at input to thermoelement T_m is assigned. Cold junction temperature T_c is thermostated.

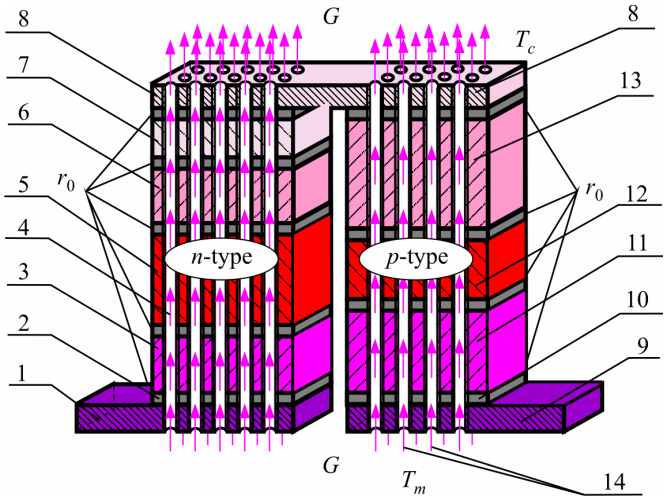

Fig. 1. Physical model of a permeable segmented thermoelement 1, 8, 9 – connecting plates; 2, 10 – connecting layers; 3, 5, 6, 7 – segments (sections) of n-type leg; 4 – heat carrier flux; 11, 12, 13 – segments (sections) of p-type leg; 14 – high thermally conductive dielectric.

A system of differential equations that describes the distribution of temperatures and heat fluxes in the steady-state one-dimensional case, in the infinitely small part *dx* of each *k*-th segment of *n*- and *p*-type legs, in dimensionless coordinates is of the form [3]:

$$\left.\begin{aligned} \frac{\mathrm{d}T}{\mathrm{d}x} &= -\frac{\alpha_k j}{\kappa_k}\,T - \frac{j}{\kappa_k}q, \\ \frac{\mathrm{d}q}{\mathrm{d}x} &= \frac{\alpha_k^2 j}{\kappa_k}T + \frac{\alpha_k j}{\kappa_k}q + j\rho_k + \frac{\alpha_T \Pi_K^1 N_K l_K^2}{(S-S_K)\,j}(t-T), \\ \frac{\mathrm{d}t}{\mathrm{d}x} &= \frac{\alpha_T \Pi_K^1 N_K l_k}{G c_P}(t-T), \end{aligned}\right\}_{n,p} \quad \begin{aligned} &k = 1,\ldots,N_{n,p} \\ &x_{k-1} \le x \le x_k \end{aligned} \qquad (1)$$

where Π_K^1 is channel perimeter; N_K is the number of channels; S_K is cross-sectional area of all channels; S is cross-section of leg together with channels; l_k – height of *k*-th segment of leg; G is heat carrier flow rate in the channels; c_P is specific heat of heat carrier; t is heat carrier temperature at point x; T is leg temperature at point x; α_T is heat transfer coefficient; α, κ, ρ are the Seebeck coefficient, thermal conductivity and resistivity of leg material.

Specific heat fluxes q and reduced density of electric current j are determined by the relations:

$$q = \frac{Q}{I}, \qquad j = \frac{Il}{S}, \tag{2}$$

where Q is power of heat flux that passes through thermoelement leg; I is electric current; $S_{n,p}$ is cross-sectional area of legs of n- and p-type thermoelement.

The boundary conditions necessary for solving (1) with regard to the Joule-Lenz heat release due to contact resistance r_0 at points of connection of leg segments are formulated in the form:

$$\begin{aligned} &T_{n,p}(0) = T_C, \qquad t_{n,p}(1) = T_m, \qquad q_{n,p}(1) = 0, \\ &T_{n,p}\left(x_k^+\right) = T_{n,p}\left(x_k^-\right), \qquad q_{n,p}\left(x_k^+\right) = q_{n,p}\left(x_k^-\right) + \frac{r_0}{S_{n,p}} I, \end{aligned} \tag{3}$$

where indices "–" and "+" denote the values of functions immediately to the left and right of the joint between x_k segments; $k = 1, \ldots, N$ is the index that determines the number of leg segment.

In the case of search for optimal values of doping impurities that determine carrier concentrations in leg segments, it is necessary to assign the dependences of material parameters α, κ, ρ on temperature and concentration of carriers (or impurities) C_k: $\alpha_k = \alpha_k(C_k, T)$, $\rho_k = \rho_k(C_k, T)$, $\kappa_k = \kappa_k(C_k, T)$.

The goal of designing a permeable segmented generator thermoelement is to determine such matched parameters (reduced current density j in the legs, heat carrier losses in channels G, concentration of doping impurities in materials of each segment C_k), whereby thermoelement efficiency reaches its maximum value.

The efficiency will be found through the ratio between the electric power P generated by thermoelement and the change in heat carrier enthalpy:

$$\eta = \frac{P}{\sum\limits_{n,p} Gc_p\left(T_m - T_C\right)}. \tag{4}$$

Efficiency maximum can be conveniently reduced to achieve functional minimum:

$$J = \ln\left[\sum_{n,p}\left\{Gc_P\left(T_m - T_C\right)\right\}\right] - \ln\left[\sum_{n,p}\left\{Gc_P\left(T_m - t(0)\right) + q(0)\frac{j\left(S - S_K\right)}{l} - I\left(\frac{r_0}{S_n} + \frac{r_0}{S_p}\right)\right\}\right]. \tag{5}$$

The problem was solved using the Pontryagin maximum principle [4] giving the necessary optimality conditions:

1) optimal values of specific current density in thermoelement legs j must satisfy the equalities

$$-\left[\frac{\partial J}{\partial j}\right]_{n,p} + \sum_{n,p}\int_0^1 \left[\psi_1^k \frac{\partial f_1^k}{\partial j_k} + \psi_2^k \frac{\partial f_2^k}{\partial j_k} + \psi_3^k \frac{\partial f_3^k}{\partial j_k}\right]_{n,p} dx = 0, \tag{6}$$

where $\left(f_1^k, f_2^k, f_3^k\right)_{n,p}$ are right-hand sides of equations (1); $\psi = \left(\psi_1^k, \psi_2^k, \psi_3^k\right)_{n,p}$ is vector function of pulses [3, 4] found from solving an auxiliary system of differential equations

$$\left.\begin{aligned} \frac{d\psi_1}{dx} &= \frac{\alpha_k j_k}{\kappa_k} R_1 \psi_1 - \left(\frac{\alpha_k j_k}{\kappa_k} R_2 - \frac{\alpha_e l_k}{\left(S - S_K\right) j_k}\right)\psi_2 + \frac{\alpha_T \Pi_K^1 N_K}{Gc_P}\psi_3, \\ \frac{d\psi_2}{dx} &= \frac{j_k}{\kappa_k}\psi_1 - \frac{\alpha_k j_k}{\kappa_k}\psi_2, \\ \frac{d\psi_3}{dx} &= -\frac{\alpha_T \Pi_K^1 N_K l_k}{\left(S - S_K\right) j_k}\psi_2 - \frac{\alpha_T \Pi_K^1 N_K}{Gc_P}\psi_3, \end{aligned}\right\}_{n,p} \tag{7}$$

where

$$\left.\begin{aligned} R_1 &= 1+\frac{d\ln\alpha}{dT}T-\frac{d\ln\kappa}{dT}\left(T+\frac{q}{\alpha}\right), \\ R_2 &= R_1+\frac{\kappa}{\alpha^2\sigma}\frac{d\ln\sigma}{dT}+\frac{d\ln\kappa}{dT}\left(T+\frac{q}{\alpha}\right). \end{aligned}\right\}_{n,p}$$

With the boundary conditions

$$\psi_1^{n,p}(1)=0,$$

$$\psi_2^{n,p}(0)=\frac{\frac{j(S-S_K)}{l}}{\sum_{n,p}\left\{Gc_P\left(T_m-t(0)\right)+q(0)\frac{j(S-S_K)}{l}-I\left(\frac{r_0}{S_n}+\frac{r_0}{S_p}\right)\right\}}, \tag{8}$$

$$\psi_3^{n,p}(0)=\frac{Gc_P}{\sum_{n,p}\left\{Gc_P\left(T_m-t(0)\right)+q(0)\frac{j(S-S_K)}{l}-I\left(\frac{r_0}{S_n}+\frac{r_0}{S_p}\right)\right\}}.$$

2) optimal values of heat carrier flow rate G in the channels

$$-\left[\frac{\partial J}{\partial G}\right]_{n,p}+\sum_{n,p}\int_0^1\left[\psi_1^k\frac{\partial f_1^k}{\partial G}+\psi_2^k\frac{\partial f_2^k}{\partial G}+\psi_3^k\frac{\partial f_3^k}{\partial G}\right]_{n,p}dx=0. \tag{9}$$

3) optimal values of doping impurities in material of each segment C_k are found from the ratios

$$\int_0^1\left[\psi_1^k\frac{\partial f_1^k}{\partial C_k}+\psi_2^k\frac{\partial f_2^k}{\partial C_k}+\psi_3^k\frac{\partial f_2^k}{\partial C_k}\right]_{n,p}dx=0,\quad k=1\ldots,N_{n,p}. \tag{10}$$

In case of thermoelement design for fixed materials in the segments the optimality conditions (10) are disregarded.

Based on the obtained relations, using successive approximation method, the Runge-Kutta numerical method for solving systems of differential equations (1) and (7) with the boundary conditions (3) and (8), the Newton method for solving systems of integral-differential equations (6), (9), (10), a computer program was developed for the design of permeable segmented thermoelement. The results of computer studies are given below.

Results of computer studies of the energy characteristics of permeable segmented generator thermoelement based on *Mg* and *Mn* silicides

Fabrication techniques of materials based on magnesium and manganese silicides and the results of experimental research on their thermoelectric properties are described in a number of scientific papers [5-12]. Analysis has revealed that with regard to the figure of merit value, the most advisable materials for creation of generator thermoelements are as follows:

– $Mg_2(Si_{0.3}Sn_{0.7})_{1-x}Sb_x$ ($0 \le x \le 0.04$) for *n*-type legs which is obtained in the course of a two-stage solid-phase reaction in combination with spark plasma sintering [6]. Maximum figure of merit of this antimony-doped silicide is $ZT \approx 1.0$ at 640 K for the composition of $x = 0.025$.

– $Mn(Al_xSi_{1-x})_{1.80}$ ($0 \le x \le 0.003$) for *p*-type legs which is obtained by induction melting with further hot pressing [7]. Maximum figure of merit of such aluminum-doped manganese silicide is $ZT \approx 0.65$ at 850 K for the composition of $x = 0.0015$.

The above materials were selected for computer investigations of the energy characteristics of permeable thermoelements. The experimental dependences of their parameters α, κ, σ were approximated in the form of polynomial dependences on temperature T and doping parameter C (doping with antimony silicide ($0 \le x \le 0.04$) for n-type leg and doping with aluminum ($0 \le x \le 0.003$) for p-type).

Calculation of permeable segmented thermoelement was performed under the following conditions: heat exchange coefficient $\alpha_T = 0.01$ W/cm^2·K, cross-sectional area of leg together with channels $S = 1$ cm^2, contact resistance at points of leg segments connection $r_0 = 5 \cdot 10^{-6}$ Ω·cm^2.

Optimal parameters of thermoelement were found, and the energy characteristics of double-segment permeable thermoelement with channel diameter $d_k = 0.1$ cm, the number of channels $N_k = 25$ pcs per 1 cm^2 depending on the height of legs are listed in Table 1. The calculated results are given for the case when heat carrier temperature at thermoelement inlet is $T_m = 900$ K, and cold junction temperature is $T_c = 300$K. It is seen that hot junction temperature of thermoelement under optimal operating conditions is $T_n(1) = 495$ K.

Table 1

Optimal parameters and energy characteristics of a double-segment permeable thermoelement based on Mg and Mn silicides

l, cm	EMF_{max},	$t_n(0)$, K	$T_n(1)$, K	P, W	G_{opt}, g·cm/s	j_{opt}, A/cm	$C_1^n{}_{opt}$	$C_2^n{}_{opt}$	$C_1^p{}_{opt}$	$C_2^p{}_{opt}$
0.6	0.019	373.4	391.0	0.339	0.0150	4.29	0.00409	0.0229	0.00159	0.00187
0.7	0.023	371.3	409.0	0.426	0.0156	5.08	0.00394	0.0229	0.00161	0.00188
0.8	0.026	369.2	424.9	0.503	0.0158	5.82	0.00374	0.0229	0.00164	0.00189
0.9	0.030	366.4	438.3	0.565	0.0158	6.47	0.00352	0.0229	0.00166	0.00190
1.0	0.033	363.2	449.3	0.612	0.0157	7.03	0.00328	0.0228	0.00169	0.00190
1.1	0.035	359.6	458.3	0.647	0.0153	7.51	0.00303	0.0228	0.00171	0.00191
1.2	0.037	356.0	465.5	0.670	0.0149	7.93	0.00278	0.0228	0.00173	0.00191
1.3	0.039	352.3	471.3	0.685	0.0145	8.30	0.00254	0.0228	0.00175	0.00192
1.4	0.041	348.8	476.0	0.692	0.0141	8.62	0.00231	0.0228	0.00177	0.00192
1.5	0.043	345.4	479.7	0.695	0.0136	8.91	0.00209	0.0228	0.00178	0.00193
1.6	0.044	342.5	482.9	0.697	0.0132	9.26	0.00185	0.0228	0.00180	0.00194
1.7	0.045	339.6	485.4	0.693	0.0128	9.51	0.00164	0.0228	0.00182	0.00194
1.8	0.046	336.9	487.5	0.687	0.0124	9.73	0.00145	0.0228	0.00183	0.00194
1.9	0.047	334.3	489.1	0.678	0.0120	9.91	0.00128	0.0228	0.00185	0.00195
2.0	0.048	332.0	490.4	0.668	0.0116	10.08	0.00112	0.0228	0.00186	0.00195
2.1	0.049	329.8	491.5	0.657	0.0113	10.23	0.00097	0.0228	0.00187	0.00196
2.2	0.049	327.8	492.4	0.645	0.0109	10.36	0.00083	0.0228	0.00188	0.00196
2.3	0.050	326.0	493.2	0.633	0.0106	10.48	0.00070	0.0228	0.00189	0.00196
2.4	0.050	324.3	493.8	0.620	0.0103	10.59	0.00058	0.0228	0.00190	0.00196
2.5	0.051	322.8	494.3	0.608	0.0100	10.69	0.00047	0.0228	0.00191	0.00197
2.6	0.051	321.4	494.7	0.596	0.0097	10.78	0.00037	0.0228	0.00192	0.00197
2.7	0.052	320.1	495.0	0.583	0.0094	10.86	0.00027	0.0228	0.00192	0.00197
2.8	0.052	318.9	495.3	0.571	0.0091	10.94	0.00019	0.0228	0.00193	0.00197
2.9	0.052	317.8	495.6	0.559	0.0089	11.01	0.00010	0.0228	0.00194	0.00198
3.0	0.053	316.8	495.8	0.547	0.0087	11.07	0.00003	0.0228	0.00194	0.00198

In so doing, heat carrier temperature at thermoelement outlet approaches cold junction temperature and is at a level of $t_n(0) = 317$ K, that is, heat carrier enthalpy is reduced by the value of temperature difference (900 – 330) = 570 K, which approaches the available change of temperatures $(T_m - T_c) = 600$ K. This testifies to a more complete utilization of heat carrier thermal energy as compared to classical thermocouple elements, where only half the available temperature difference is used beneficially [2].

Fig. 2 shows a dependence of maximum efficiency η and the respective specific electric power W of permeable segmented generator thermoelement at optimal values of j, G and doping parameter C in leg segments on the general height of legs l. It is seen that with increase in leg height, the efficiency grows and reaches saturation near the value of 5.5 %, and the respective specific power P has an extremum at the leg height $l \sim 1.5$ cm.

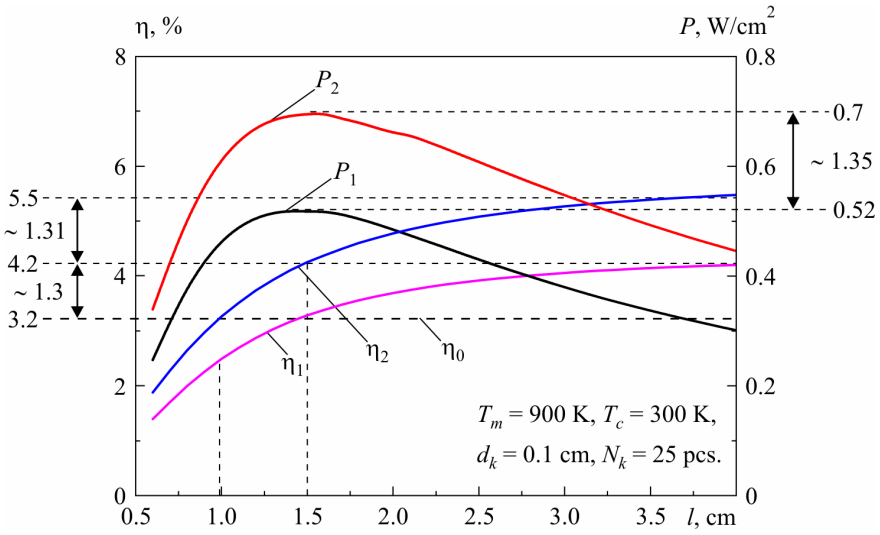

Fig. 2. Dependence of the energy characteristics of a permeable segmented thermoelement based on Mg and Mn silicides on leg length l. 1 – single-segment permeable thermoelements; 2 – double-segment permeable thermoelements.

At such height (1.5 cm) maximum efficiency value (for a single-segment permeable thermoelement) is about 3.2 %, which corresponds to the efficiency of classical thermocouple thermoelement ($\eta_0 = 3.2$ %) under similar operating conditions. In so doing, the specific power value does not exceed 0.52 W/cm^2 for a single-segment leg and 0.7 W/cm^2 for a double-segment leg.

Calculation results show that with increase in the number of leg segments, there is saturation both in the value of specific power and the efficiency. Hence, the reasonable number of leg segments makes 2 – 3 pcs. Further build up of segments does not result in considerable improvement of energy conversion characteristics which is also typical of classical segmented thermoelements [13].

Results of research on the dependence of the energy characteristics of a permeable segmented generator thermoelement on channel diameter d_k for single- (index 1) and double-segment legs (index 2) under conditions of optimal values of j, G and concentrations of doping impurities in leg segments are given in Fig. 3.

It is seen that increase in channel diameter improves energy conversion efficiency. In so doing, the electric power in maximum efficiency mode has an extremum in the case of $d_k = 0.14$ cm, whereby the efficiency is 3.2 % for a single-segment thermoelement and 4 % for a double-segment thermoelement. The results obtained show that for practical applications the reasonable channel diameter of a permeable segmented thermoelement will lie within 1 to 2 cm.

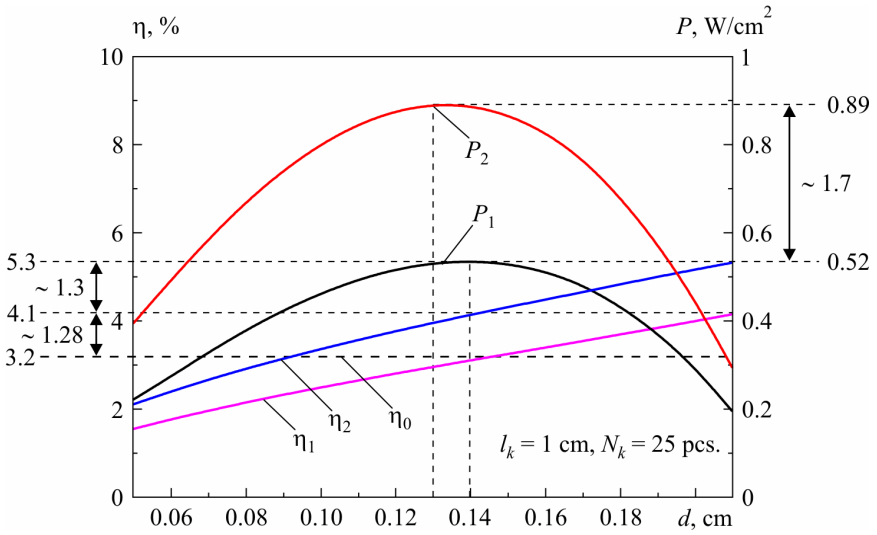

Fig. 3. Dependence of the energy characteristics of a permeable segmented thermoelement on channel diameter d_k. 1 – single-segment permeable thermoelements; 2 – double-segment permeable thermoelements.

The effect of the number of channels N_k on the energy characteristics of a permeable thermoelement under conditions of optimal j, G and C_k for different number of leg segments N is shown in Fig. 4.

It is evident that the efficiency grows with increase in the number of channels, reaching the saturation. In so doing, the specific electric power has a maximum observed at 13 channels per 1 cm^2. So, the rational number of channels per unit area will be within 10 to 24 pcs per 1 cm^2. Considerable efficiency increase depending on the number of segments of thermoelement legs N is also observed only for the variant of using 2 segments. Further increase in the number of segments does not result in essential efficiency and specific power increase.

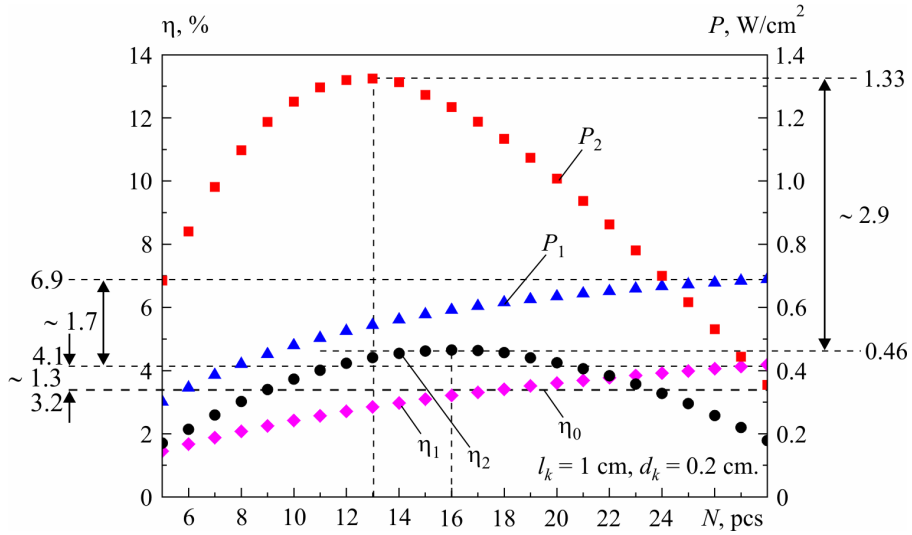

Fig. 4. Dependence of the energy characteristics of a permeable segmented thermoelement on the number of channels N_k. 1 – single-segment permeable thermoelements; 2 – double-segment permeable thermoelements.

Comparison of the efficiency of permeable thermoelement to that of classical thermoelement η_0 under similar operating conditions testifies to possible increase of energy conversion efficiency by 30 to 40 %.

Conclusions

1. Procedure for calculation and design of a permeable generator thermoelement of segmented materials based on *Mg* and *Mn* silicides is represented.
2. The effect of structural parameters (the diameter and number of channels, the height of legs and the number of segments) under optimal efficiency operating conditions on the basic energy conversion characteristics is determined. The reasonable values of such parameters are found, which allows finding the necessary material science and technological requirements for the development of a permeable thermoelement.
3. It is shown that with the use of materials based on *Mg* and *Mn* silicides for a permeable segmented thermoelement at the initial heat carrier temperature 900 K and thermostated cold junctions at a level of 300 K, the reasonable number of leg segments is 2 pcs. Comparison of a permeable thermoelements in terms of thermodynamic energy conversion efficiency to conventional thermoelements has shown the possibility of energy conversion efficiency increase by 30 to 40 %.

References

1. V.R. Bilinsky-Slotylo, L.M. Vikhor, and V.Ya. Mykhailovsky, Design of Thermoelectric Generator Modules from *Mg* and *Mn* Silicide Based Materials, *J. Thermoelectricity* **1**, 60 – 66 (2013).
2. L.I. Anatychuk, R.G. Cherkez, Permeable Thermoelement in Electric Energy Generation Mode, *J. Thermoelectricity* **2**, 35 – 46 (2003).
3. L.I. Anatychuk, R.G. Cherkez, Permeable Sectional Thermoelement in Electric Energy Generation Mode, *J. Thermoelectricity* **3**, 5 – 12 (2010).
4. L.S. Pontryagin, V.G. Boltyansky, R.V. Gamkrelidze, and E.F. Mischenko, *Mathematical Theory of Optimal Processes* (Moscow: Nauka, 1976), 392 p.
5. Zh. Du, T. Zhu, and X. Zhao, Enhanced Thermoelectric Properties of $Mg_2Si_{0.58}Sn_{0.42}$ Compounds by *Bi* Doping, *Materials Letters* **66** (1), 76 (2012).
6. W. Liu, Q. Zhang, X. Tang X et al., Thermoelectric Properties of *Sb*-Doped $Mg_2Si_{0.3}Sn_{0.7}$, *Journal of Electronic Materials* **40** (5), 1062 (2011).
7. W. Luo, H. Li, F. Fu et al., Improved Thermoelectric Properties of *Al*-Doped Higher Manganese Silicide Prepared by a Rapid Solidification Method, *Journal of Electronic Materials* **40** (5), 1233 (2011).
8. A.J. Zhou, T.J. Zhu, X.B. Zhao et al., Improved Thermoelectric Performance of Higher Manganese Silicides with *Ge* Additions, *Journal of Electronic Materials* **39** (9), 2002 (2010).
9. M.J. Yang, L.M. Zhang, L.Q. Han et al., Simple Fabrication of Mg_2Si Thermoelectric Generator by Spark Plasma Sintering, *Indian Journal of Engineering and Materials Sciences* **16**, 277 (2009).
10. T. Sakamoto, T. Iida, A. Matsumoto et al., Thermoelectric Characteristics of a Commercialized Mg_2Si Source Doped with *Al*, *Bi*, *Ag*, and *Cu*, *Journal of Electronic Materials* **39** (9), 1708 (2010).
11. T. Sakamoto, T. Iida, Sh. Kurosaki et al., Thermoelectric Behavior of *Sb*- and *Al*-Doped *n*-Type Mg_2Si Device Under Large Temperature Differences, *Journal of Electronic Materials* **40** (5), 629 (2011).
12. R. Song, Y. Liu, and T. Aizawa, Solid State Synthesis and Thermoelectric Properties of *Mg*-*Si*-*Ge* System, *Journal of Materials Science & Technology* **21** (5), 618 (2005).
13. L.I. Anatychuk, L.N. Vikhor, Generator Modules of Segmented Thermoelements, *Energy Conversion and Management* **50** (9), 2366 – 2372 (2009).

Submitted 20.12.2013.

L.I. Anatychuk[1], M.V. Havrylyuk[1], V.V. Lysko[1,2], Yu.I. Senyuk[2]

[1]Institute of Thermoelectricity of the NAS and MES Ukraine,
1, Nauky Str., Chernivtsi, 58029, Ukraine;
[2]Yu. Fedkovych Chernivtsi National University, 2, Kotsyubinsky Str.,
Chernivtsi, 58000, Ukraine

MEASUREMENT OF THERMOELECTRIC PROPERTIES OF MATERIALS AT HIGH TEMPERATURES

Results of research on the errors arising in the measurement of thermoelectric properties of materials by the absolute method in the temperature range of 30 – 900 °C are presented. It is established that the main measurement error is due to radiation from the surface of samples. It is also established that at temperatures of 600 – 900°C the use of gradient radiation screens becomes inefficient, namely the error of thermal conductivity measurement increases to 25 – 30 %. The efficiency of reducing the error of such measurements through use of powder thermally insulating materials is studied. It is established that their application combined with gradient thermal screens allows reducing the value of errors to 1.5 – 5.5 %. An experimental device that employs these methods of errors reduction is described.
Key words: measurements, absolute method, thermoelectric parameters, errors.

Introduction

General characterization of the problem. Creation of new thermoelectric materials, efficient at elevated temperatures, is one of important tasks in thermoelectricity [1-3]. Its solution requires methods and equipment to measure thermoelectric properties of materials with possibly high accuracy. In [4-6] it is shown that the acceptable measurement accuracy is efficiently provided by the absolute method using special gradient radiation screens. When measuring the figure of merit of material by this method, the error at temperatures up to 500 °C is not more than 4.7 %. At higher temperatures the use of radiation screens becomes inefficient and measurement errors are drastically increased.

The purpose of this work is research on physical factors causing the increase in errors at temperatures up to 900 °C, finding the ways for reduction of their impact on the accuracy of measurement, development of precise methods of measuring thermoelectric properties of materials and creation on their basis of corresponding measuring equipment.

Physical, mathematical and computer models

The model comprises a cylinder sample of length l and diameter d, a reference heater, a thermostat and a screen with a heater (Fig. 1).

The thermostat temperature is T_0, the reference heater and screen heater temperature is T_1; the thermal conductivity of sample material is κ_1, of the reference heater – κ_2, of the screen – κ_3, of the screen heater – κ_4; the emissivity factor of the sample is ε_1, of the reference heater – ε_2, of the screen – ε_3, of the screen heater – ε_4, of the thermostat – ε_5.

The model takes into account heat exchange due to radiation between the sample, screen,

sample heaters and thermostat surfaces; heat transfer along the sample and screen; heat exchange due to radiation between the screen and thermostat.

To find temperature distribution in the measuring device, a system of thermal conductivity equations should be solved for each of its elements

$$\nabla(-\kappa_i \nabla T) = Q_i, \tag{1}$$

where Q_i is power of internal heat sources.

To solve this problem, the COMSOL Multiphysics software package was used

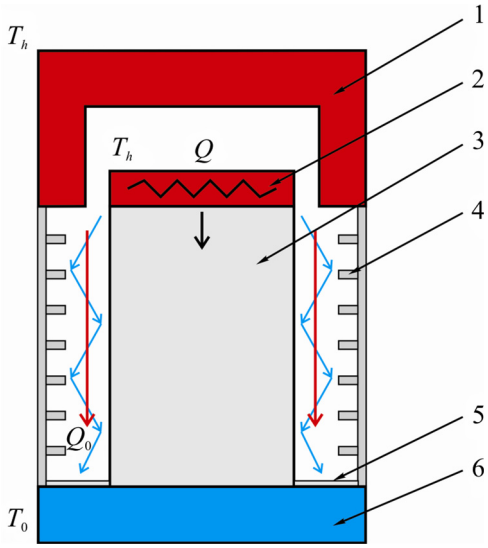

Fig. 1. Physical model of a device for measurement of thermoelectric material parameters by the absolute method: 1 – screen heater, 2 – reference heater, 3 – sample under test, 4 – screen with radiation rings, 5 – reflector, 6 – thermostat.

The boundary conditions that take into account heat exchange due to radiation between the measuring system members:

$$q = \varepsilon_i (G - \sigma T^4), \tag{2}$$

where σ is the Stephan-Boltzmann constant, G is heat flux due to radiation

$$G = G_m + F_{amb}\sigma T_{amb}^4, \tag{3}$$

G_m is heat flux from other device members, F_{amb} is viewing field factor equal to viewing field share that is not subject to other surfaces, T_{amb} is temperature at a distant point in the directions included to F_{amb}. Coefficient G_m which depends on mutual arrangement of surfaces is calculated by introducing into computer model of additional variable J assigned by equation

$$J = (1-\varepsilon)\left\{G_m(J) + F_{amb}\sigma T_{amb}^4\right\} + \varepsilon\sigma T^4. \tag{4}$$

Results of investigation of the effect of radiation on thermal conductivity measurement accuracy at high temperatures

With expansion of operating temperature range, the role of radiation will increase. Fig. 2 shows the values of errors δκ at determination of heat flux through the sample versus measurement

temperature for different values of absorption factors of the sample and reference heater surfaces. It is seen that even with the use of radiation rings on the screen and a reflector on the thermostat the errors reach 25 – 30 %.

The results obtained testify to the necessity of taking additional measures for the reduction of uncontrolled heat losses due to radiation from the surface of measured sample.

One such measure can be the use of powder heat insulating materials that fill the space between the sample and radiation screen. One of possible materials is perlite. Perlite thermal conductivity in the temperature range of 30 to 900 °C is given in Fig. 3.

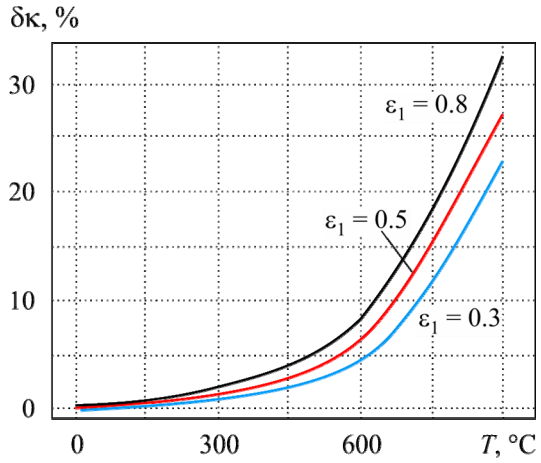

Fig. 2. Temperature dependences of errors in thermal conductivity measurement for different values of sample emissivity.

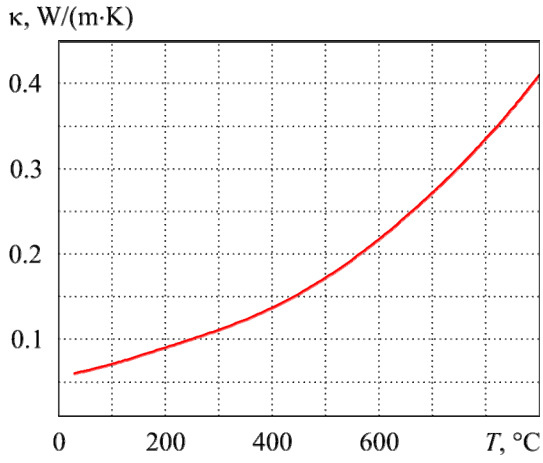

Fig. 3. Perlite thermal conductivity in the temperature range of 30 – 900 °C.

Computer simulation was used to investigate measurement errors for the model given in Fig. 4.

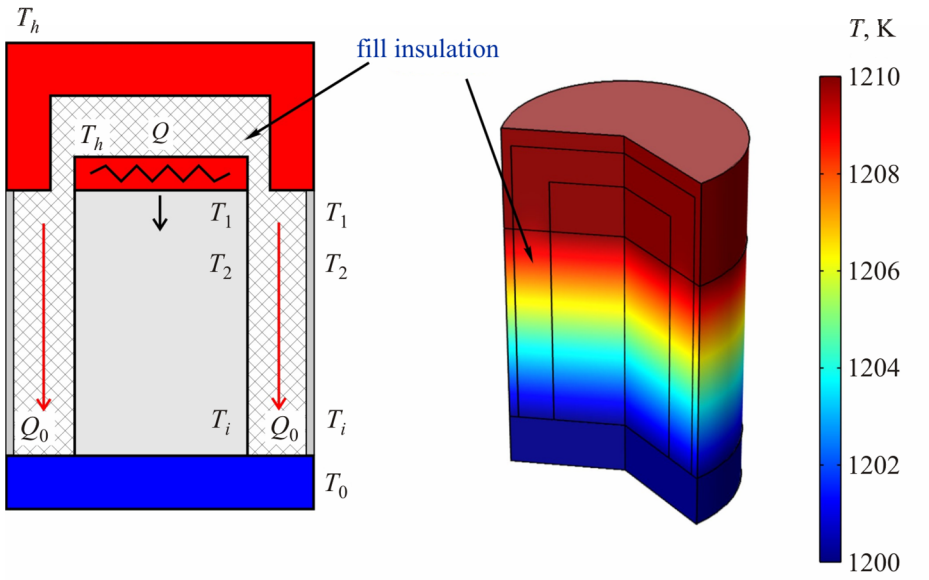

a) *b)*

Fig. 4. Use of perlite for the reduction of heat losses due to radiation a) physical model; b) temperature distribution obtained with the aid of COMSOL Multiphysics.

Simulation results are shown as temperature dependences of thermal conductivity measurement errors δκ for different values of sample thermal conductivity (Fig. 5).

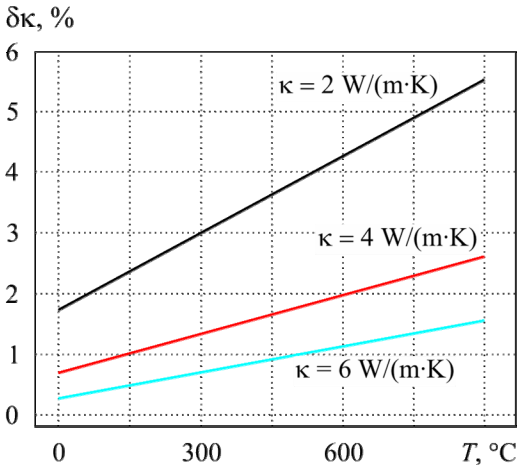

Fig. 5. Effect of fill insulation on thermal conductivity measurement errors.

As is evident, the use of thermal insulation allows reducing the measurement errors of κ to 1.5 – 5.5 %.

Description of measuring unit design

The results obtained were used to develop a measuring unit of installation for determination of thermoelectric properties of materials in the range of temperatures 30 to 900 °C (Fig. 6).

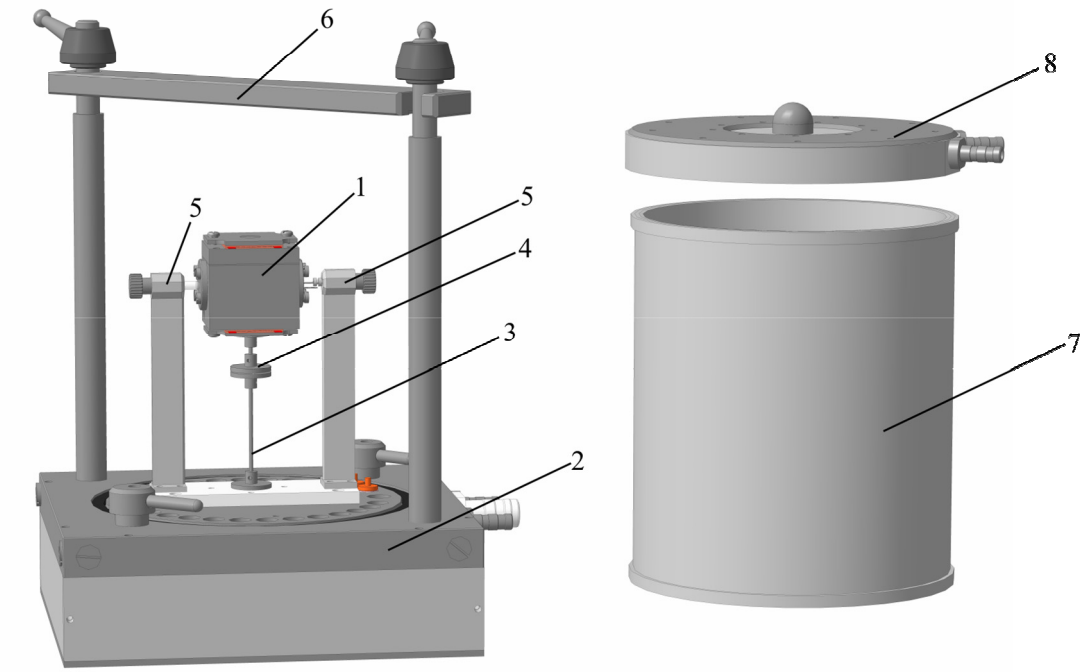

Fig. 6. Measuring unit of installation for determination of thermoelectric properties of materials.
1 – measuring device, 2 – water-cooled base of measuring unit,
3 – measuring thermostat post, 4 – thermostat locking heater, 5 – sample pressure device,
6 – bell jar pressure device, 7, 8 – lid of water-cooled bell jar.

Sample under test is placed inside the measuring device and pressed together with the heater to mounting platform (Fig. 7).

To reduce measurement errors, thermal switches are employed and powder heat insulating material is used to fill free space inside the measuring device.

To prevent the external surface of device from overheating, the measuring unit is also filled with heat insulating material.

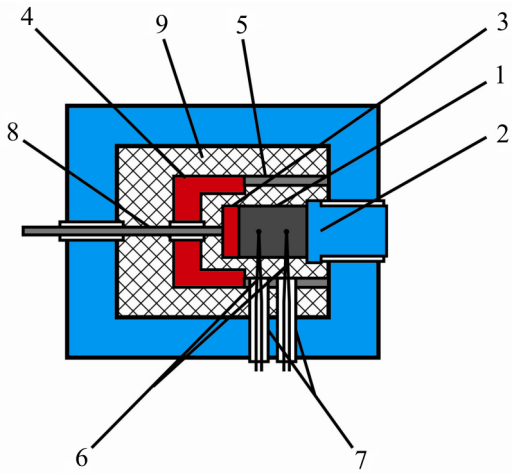

Fig. 7. Schematic of measuring device. 1 – sample under test, 2 – mounting platform, 3 – reference heater, 4 – protective heater, 5 – screen, 6 – thermocouples, 7 – sample pressure device, 8 – thermal switches, 9 – fill insulation.

Fig. 8 shows temperature distribution inside the measuring unit obtained by computer simulation. Computer studies allowed determining the necessary powers of background, reference and protective heaters and optimizing the unit design to achieve the isothermal conditions inside the measuring device where the sample is located. Moreover, the values of errors in the measurement of the other thermoelectric parameters were determined for the developed measuring unit, which are as follows: thermoEMF ~ 1.5 %, electric conductivity ~ 1.5 %, thermoelectric figure of merit ~ 10 %.

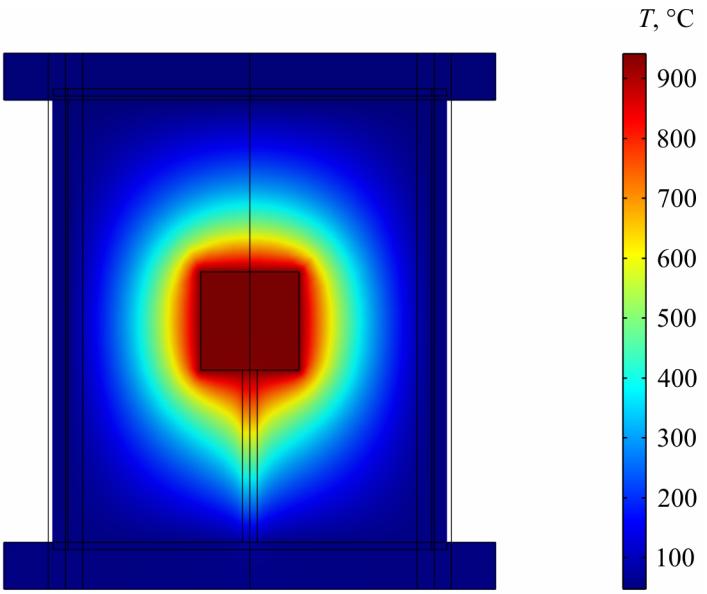

Fig. 8. Temperature distribution inside a passive thermostat.

Conclusions

1. The errors of thermal conductivity measurement by the absolute method at temperatures up to 900 °C have been studied. It has been established that the use of radiation screens alone for the minimization of heat losses from the sample surface results in the errors up to 25 – 30 %.
2. The values of errors in the measurement of thermal conductivity when using fill insulation have been calculated. For the model of measuring device in hand they make 1.5 to 5.5 %.
3. The measuring device has been developed and the values of its errors have been determined which at a temperature up to 900 °C are as follows: thermal conductivity ~ 5 %, thermoEMF ~ 1.5 %, electric conductivity ~ 1.5 %, thermoelectric figure of merit ~ 10 %.

References

1. T. Caillat, A. Borshchevsky, J.-P. Fleurial, Search for New High Temperature Thermoelectric Materials, *SAE Technical Paper* 929424 (1992).
2. Jin-Cheng Zheng, Recent Advances on Thermoelectric Materials, *Front. Phys. China* **3** (3), 269 – 279 (2008).
3. J.R. Sootsman, D.Y. Chung, and M.G. Kanatzidis, New and Old Concepts in Thermoelectric Materials, *Angewandte Chemie International Edition* **48** (46), 8616 – 8639(2009).
4. L.I. Anatychuk, M.V. Havrylyuk, and V.V. Lysko, Installation for Measurement of Semiconductor Thermoelectric Material Properties, *Journal of Thermoelectricity* **3**, 41 – 49 (2010).
5. L.I. Anatychuk, V.V. Lysko, *Patent of Ukraine № 71614*, Device for Measurement of Electric Conductivity, Thermal Conductivity and ThermoEMF of Thermoelectric Materials, Application № u 2011 13846 of 24.11.2011; Publ. 25.07.2012; Bul. № 14.
6. L.I. Anatychuk, V.V. Lysko, Investigation of the Effect of Radiation on the Precision of Thermal Conductivity Measurement by the Absolute Method, *Journal of Thermoelectricity* **1,** 65 – 73 (2012).

Submitted 20.12.2013.

L.I. Anatychuk[1], P.A. Barabash[2], V.G. Rifert[2], Yu.Yu. Rozver[1], V.I. Usenko[2], R.G. Cherkez[1]

[1]Institute of Thermoelectricity of the NAS and MES of Ukraine,
1, Nauky Str., Chernivtsi, 58029, Ukraine;
[2]National Technical University of Ukraine "Kyiv Polytechnic Institute",
37, Peremohy Ave., Kyiv 03056, Ukraine

THERMOELECTRIC HEAT PUMP AS A MEANS OF IMPROVING EFFICIENCY OF WATER PURIFICATION SYSTEMS ON SPACE MISSIONS

The paper presents the results of development and test of a modernized high-performance apparatus for water supply to cosmonauts during long-term missions. The basic structural units of the device include a centrifugal vacuum distiller (CD) and a thermoelectric heat pump (THP). The productivity is up to 5 l/hour, specific energy consumption is less than100 W·hour/l, the degree of water recovery from the source liquid is at least 92 %. The apparatus was created by the efforts of Thermodistillation Co. and Altec-M Ltd. The research was performed by the National Technical University of Ukraine "Kyiv Polytechnic Institute" and Institute of Thermoelectricity. Testing of the apparatus on the test facilities of Honeywell International and NASA has shown that the use of thermoelectric heat pump reduces energy expenditure by a factor of 1.6 as compared to closest competing device, i.e. vapor compression distiller (VCD). In so doing, CD and THP system work stably with concentration level to 77 %.

Key words: space flights, centrifugal distiller, thermoelectric heat pump, energy efficiency.

Introduction

Water supply to human crew on long-term space missions is a serious and relevant problem due to impossibility of its on board delivery during the flight. The problem was solved by water recovery from cosmonauts' liquid waste products – urine, sweat, service and sanitary water [1-3].

At the present time, there are several technologies of liquid waste purification. Depending on the degree of water contamination, use is made of ionic exchange, electrodialysis, a reverse osmosis and thermal distillation. Ionic exchange and electrodialysis are used at low concentrations of salts $5\cdot10^2 – 5\cdot10^3$ mg/l. To perform a reverse osmosis at desalination of highly mineralized water or urine, it is necessary to employ high pressure pumps (up to 70 bars) and make a pretreatment of the source liquid. The disadvantage of this method is a restricted service life of membranes. The technology of water purification through use of phase transition (distillation) offers the greatest promise, since it is free from the above disadvantages. The strong point of this method is independence of water purification quality of the degree of mineralization and contamination of the source liquid.

US specialists developed three systems of such water purification, namely AES system – liquid evaporation on wick modules using hot air, TIMES system – liquid evaporation on porous membranes using a thermoelectric heat pump and VCD system – centrifugal vapor compression distiller [4].

Since 1974 the National Technical University of Ukraine "Kyiv Polytechnic Institute" has developed distillers with a rotating surface on which evaporation occurs in a thin film [5-7]. During

1999 – 2005 Thermodistillation Co., Honeywell International Inc. (USA) and Institute of Thermoelectricity have jointly manufactured a new model of five-stage centrifugal distiller CD-5 with a thermopile as a heat pump (THP) [8-12]. The apparatus efficiency was tested on the NASA facilities during 2006 – 2009. The results of testing centrifugal distillation systems equipped with thermoelectric heat pumps are given below.

Multi-stage distillation apparatus with a thermoelectric heat pump

The method of improving the efficiency of distillation devices through use of multi-stage evaporation process is common nowadays. Its principle is that the secondary steam of one evaporation stage is used by the heating steam in the next stage. Pressure in each subsequent stage is maintained lower than in the previous one. *N*-stage distiller gives almost *n*-fold reduction of energy expenditures as compared to a single-stage distiller.

The cascade system is schematically shown in Fig. 1 [13]. Liquid to be purified is fed to a multi-stage vacuum rotor distiller (CD) where its evaporation and condensation take place. The necessary energy is transferred from the heat pump. Here the distilled water is cooled, and the purified liquid is heated. Both fluxes are directed by pumping with CD to heat pump circulation channels and come back to CD. The temperatures are from 35° to 45 °C.

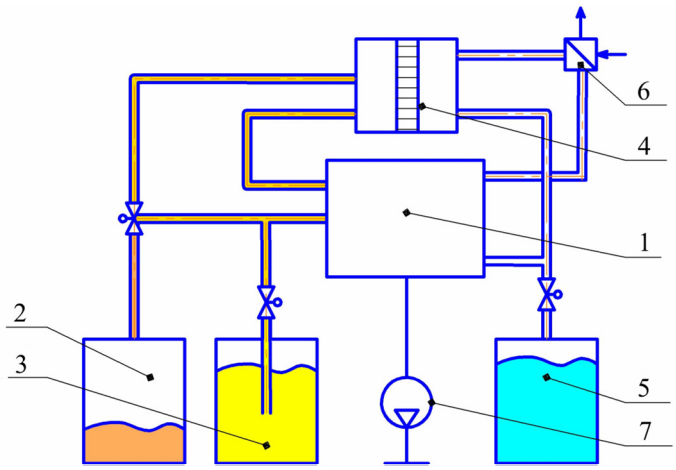

Fig. 1. Schematic of centrifugal distillation with a thermoelectric heat pump. 1 – cascade distiller CD, 2 – concentrate container, 3 – source liquid container, 4 – thermoelectric heat pump, 5 – purified water container, 6 – cooler, 7 – vacuum pump.

During a periodic cycle, 10 liters of the source liquid are processed. Purification yields 9 liters of purified water and one liter of brine.

Thermoelectric heat pump

"Altec-7001" thermopile based on the Peltier and Joule effects serves as a heat pump [10]. It assures heat removal from one object and transfer of this heat together with the Joule heat to another object. The outward appearance of "Altec-7001" thermopile is shown in Fig. 2. It comprises special liquid heat exchangers, thermoelectric modules and liquid collectors forming motion of liquids along the heat exchangers. The heat exchangers meet high technical requirements, namely they must possess low thermal resistance and, on the other hand, must be made of materials resistant to aggressive liquids. Such materials generally possess increased thermal resistance.

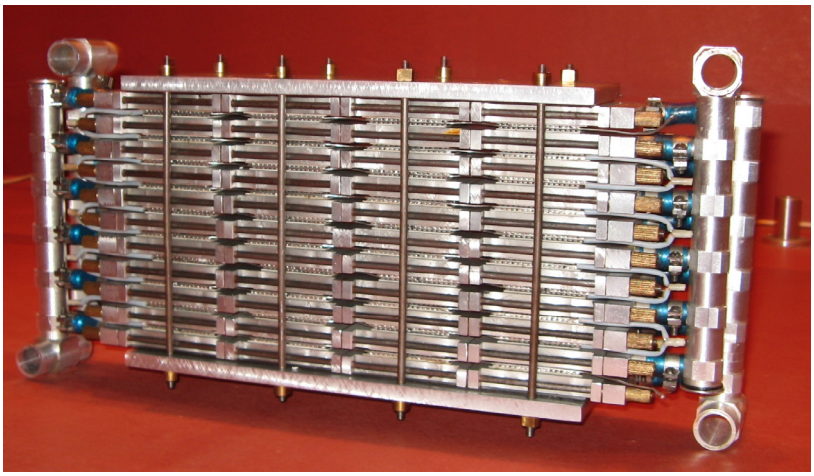

Fig. 2. Outward appearance of "Altec-7001" thermopile

Design optimization of heat exchangers was done by computer simulation. This resulted in heat exchanger designs consisting of titanium tubes and aluminum heat concentrators embracing them. To assure a turbulent mode of liquid motion, spiral titanium inserts are mounted into titanium tubes. Heavy demands are imposed on thermoelectric modules, especially as regards reliability. In order to increase the heat pump service life, the module components were connected into parallel-in-series circuits, increasing mean time between failures (MTBF) hundreds of times.

The basic technical characteristics of thermoelectric heat pump are given in Table 1.

Table 1

Basic technical characteristics of "Altec-7001" thermopile

Parameter	Value
Overall dimensions (length / width / height), mm	410/125/160
Mass, kg	6.1
DC electric voltage, V	12 – 30
Maximum electric power, W	500
Efficiency factor (max)	2.5
Hydraulic resistance in cooling circuits, bar in cooling circuit in heating circuit	 < 0.20 < 0.15
Operating mode	continuous
Processed liquids	urine, sewage water

Long-duration test of CD-5 centrifugal distiller with "Altec-7001" thermopile was performed on the NASA test facility for 2006 – 2009. The test was performed on two solutions (Table 2). Altogether, 1500 kg of sewage water were processed.

To estimate the quality of distillation, comparative rests were performed at two NASA centers. At Marshall Space Flight Center (MSFC), Wiped-Film Rotating Disk (WFRD) (also centrifugal distiller with a vapor compressor) and Vapor Compression Distillation (VCD) systems were tested; at Johnson Space Center (JSC) - Cascade Distillation Subsystem (CD-5).

Table 2

Results of testing CD-5 centrifugal distiller with "Altec-7001" thermopile

Parameter	Test on solution № 1	Test on solution № 2
Solution composition	56.6 % condensed water 43.3 % urine	18.3 % condensed water, 14.0 % urine 67.7 % water for sanitary needs
Amount of processed liquid, kg	381	1198
Productivity, kg/hour	4.1 ± 0.1	5.2 ± 0.1
Regeneration degree, %	93.4 ± 0.7	90.3 ± 0.5
Specific energy consumption, W·h/kg	99 ± 6	106 ± 2

Table 3 compares the basic characteristics of centrifugal distillation systems CD-5, VCD and WFRD. The CD-5 distiller has lower specific energy consumption as compared to VCD with a higher, up to threefold, productivity and a larger recovery degree (90 – 94 and 89 %, respectively).

Table 3

Specification figures of tested distillers at recovery of solution № 1

	CD-5	VCD	WFRD
Productivity, kg/hour	3.7	1.63	16.1
Specific energy consumption, W·h/kg	109	188	85
Average power, W	375	297	1252

Distillate obtained using CD-5 without any post treatment [15] confirmed excellent quality and full conformity to standards. The quality of distillate obtained from VCD and WFRD, is inferior to that from CD-5 by factor of 2 to 8 [14].

In the course of all tests on NASA, Honeywell and Thermodistillation test facilities (> 1000 hours), the thermoelectric heat pump has operated trouble-free, without deviations from the required parameters and characteristics.

Conclusion

The most promising systems of water recovery and purification for long-term manned space missions were analyzed. The developed and manufactured multi-stage centrifugal distillation system equipped with a thermoelectric heat pump was compared to closest analogs. In the most important figures, namely specific energy consumption, overall dimensions, weight and quality of distillate obtained, the CD-5 + THP system outperforms all known distillation and purification systems of space application.

References

1. L.I. Anatychuk, Rational Areas of Investigation and Application of Thermoelectricity, *Journal of Thermoelectricity* **1**, 3 – 14 (2001).
2. L.I. Anatychuk, Current Status and Some Prospects of Thermoelectricity, *Journal of Thermoelectricity* **2**, 7 – 20 (2007).

3. V.G. Rifert, V.I. Usenko, P.A. Barabash, L.I. Anatychuk, Yu.Yu. Rozver, A. Lubman, Development and Test of Water Regeneration System of Liquid Vital Activity Waste Aboard Manned Spacecrafts with the use of Thermoelectric Heat Pump, *Journal of Thermoelectricity* **2**, 59 – 68 (2011).
4. M.B. Gorensek, D. Baer-Peckham, Space Station Water Recovery Trade Study-Phase Change Technology, *18th International Conference on Environmental Systems, San Francisco, July 1988.*
5. V.G. Rifert, P.A. Barabash, and N.N. Goliyad, Methods and Processes of Thermal Distillation of Water Solution for Closet Water Supply Systems, SAE Paper 901294, *20th International Conference on Enviromental Systems, Williamsburg, July 1990.*
6. N.M. Samsonov, L.S. Bobe, V.M. Novikov, N.S. Farafonov, B.Ja. Pinsky, V.V. Rakov, V.G. Rifert, Ju.I. Grigoriev, V.V. Komolov, and N.N. Protasov, Development and Testing of a Vacuum Distillation Subsystem for Water Reclamation from Urine, SAE Paper 1999-01-1993, *29th International Conference on Environmental Systems, Denver, July 1999.*
7. V. Rifert, V. Usenko, I. Zolotukhin, A. MacKnight, and A. Lubman, Comparison of Secondary Water Processors Using Distillation For Space Applications, SAE Paper 1999-01-1991, *29th International Conference on Environmental Systems, Denver, July 1999.*
8. A. Lubman, A. MacKnight, V. Reddig, L.S. Bobe, B.Y. Pinsky, V.V. Rakov, and M. Edeen, Performance Evaluation of a Three-Stage Vacuum Rotary Distillation Processor, SAE Paper 2000-01-2386, *30th International Conference on Environmental Systems and 7th European Symposium on Space Environmental Control Systems, Toulouse, France, July 2000.*
9. V. Rifert, V. Usenko, I. Zolotukhin, A. MacKnight, and A. Lubman, Design Optimization of Cascade Rotary Distiller with the Heat Pump for Water Reclamation from Urine, SAE Paper 2001-01-2248, *31st International Conference on Environmental Systems, Orlando, July 2001.*
10. V.G. Rifert, V.I. Usenko, I.V. Zolotukhin, L.I. Anatychuk, A. MacKnight, and A. Lubman, Development and Test Cascade Centrifugal Distiller for Regeneration of Water from Urine, *Industrial Heat Engineering. International Scientific and Applied Journal. National Academy of Sciences of Ukraine* **23** (4-5) (2001).
11. V.G. Rifert, V.I. Usenko, I.V. Zolotukhin, A. MacKnight, and A. Lubman, Cascaded Distillation Technology for Water Processing in Space, SAE Paper 2003-01-2625, *34th International Conference on Environmental Systems, Orlando, July 2003.*
12. L.D. Noble, Jr., F.H. Schubert, R.E. Graves, and J.H. Miernik, An Assessment of the Readiness of Vapor Compression Distillation for Spacecraft Wastewater Processing, SAE Paper 911454, *21st International Conference on Environmental Systems, San Francisco, California, July 15-18, 1991.*
13. A. Lubman, A. MacKnight, V. Rifert, and P. Barabash, Cascade Distillation Subsystem Hardware Development for Verification Testing, SAE Paper 2007-01-3177, *37th International Conference on Environmental Systems, Chicago, Illinois, July 9-12, 2007.*
14. J. Mc Quillan, Karen D. Pickering, Molly Anderson, Layne Carter, Michael Flynn, Michael Callahan, Leticia Vega, Rama Allada, and Jannivine Yeh, Distillation Technology Down-selection for the Exploration Life Support (ELS) Water Recovery Systems Element, AIAA 2010-6125, *40th International Conference on Environmental Systems, 2010.*
15. M.R. Callahan, V. Patel, and K.D. Pickering, Cascade Distillation Subsystem Development: Early Results from the Exploration Life Support Distillation Technology Comparison Test, AIAA 2010-6149, *40th International Conference on Environmental Systems, 2010.*

Submitted 20.12.2013.

I.A. Moskalyk[1], O.M. Manyk[2]

I.A. Moskalyk

[1]Institute of Thermoelectricity of the NAS and MES Ukraine, 1, Nauky Str., Chernivtsi, 58029, Ukraine;
[2]Yu. Fedkovych Chernivtsi National University, 2, Kotsyubinsky Str., Chernivtsi, 58012, Ukraine

ON THE USE OF THERMOELECTRIC COOLING IN CRYODESTRUCTION PRACTICE

O.M. Manyk

In this paper, the current state of using cryodestruction in medical practice, cryodestruction mechanism and temperature modes are analyzed. The disadvantages of liquid nitrogen-based devices and perspectives for using thermoelectricity in cryodestruction practice are defined.
Key words: cryodestruction, liquid nitrogen cooling, thermoelectric cooling.

Introduction

General characterization of the problem. It is a matter of common knowledge in medical practice that temperature action is an important factor in the therapy of many human diseases [1]. One of promising lines is cryodestruction, i.e. a combination of surgical therapy methods based on local freezing of human body tissues. To perform cryodestruction, it is necessary to cool certain area of human body to temperature –50 °C. Today such cooling is implemented by means of special cryoinstruments with the application of nitrogen [1, 3-7]. However, the use of nitrogen has a number of disadvantages, namely nitrogen does not assure cooling with the required accuracy of temperature control, and there are risks of overcooling with negative consequences. Moreover, liquid nitrogen is a rather dangerous substance and must be used with proper care, while liquid nitrogen delivery is not always accessible, narrowing down possible application of such method. This opens up the prospects of using thermoelectric cooling for cryodestruction that can implement cooling to temperature (0 ÷ –80)°C. Thermoelectric devices of medical application can assign precisely the necessary temperature of working instrument, the time of thermal action on the respective area of human body and assure cyclic change of cooling and heating [2].

Therefore, *the purpose of this paper* is analysis of the present state of using cryodestruction and determination of promising lines of using thermoelectricity in cryodestruction practice.

Cryodestruction mechanism

The problem of cold action on the biological tissue should be considered in two different temperature ranges, namely above and below freezing temperature of tissue fluid [8-13].

In the former case it is the matter of physiological response of biological tissue to ambient temperature reduction, and in the latter case we are referring to the damage of cellular structures due to tissue fluid expansion on freezing (formation of ice crystals). In different types of cells, with a decrease in temperature, synthesis of the so-called cold shock proteins is sharply accelerated (several factors of ten), assuring adaptation of cells to new temperature conditions. During this adaptation,

many cellular processes that are practically stopped by cold shock are restored, and a cell starts normal functioning under new conditions.

Below freezing point, the process of freezing intercellular fluid starts, then intracellular frosting occurs with formation of ice crystals moving around crystallization centres. Cryonecrosis arises gradually, whereby the cells and intracellular membranes are damaged by ice crystals ("cut" in a submicroscopic fashion). Blood circulation, ingress of oxygen and nutritional substances, tissue respiration and all biochemical processes during freezing cease completely. As a result, cells in which all vital processes were paralyzed for a long term are perished. At an instant when ice crystals are formed in the tissues, the osmotic pressure in the cells is drastically increased, since extracellular fluid freezes faster and salt cations are directed through membranes inside the cells. Such osmotic shock cannot be survived by biological cells.

Cryodestruction is widely used for the destruction of pathogenic tissues, i.e. tumors. During the first hours after cryosurgical operation, a direct edema of the tumor and surrounding tissue occurs. The edema is of primary importance in assuring hemostatic characteristics of cryodestruction. In so doing, the surrounding tissue is compressed by the edema, as a result of which blood circulation of damaged tissue area is restricted. Therefore, the tumor is separated, metabolism is stopped and intracellular pressure is increased. That is why cryodestruction is a disseminating method for the destruction of malignant tumors [13-18].

Use of cryodestruction in medical practice

Cryodestruction is qualified as the most natural and physiological method for producing necrosis, i.e. destruction of biological tissue [5]. With cryodestruction, in the process of surgical operation a pathogenic tissue is not removed, however, destructed due to cryothermal effect, the tissue will remain on its place for a rather long time. In the destructed pathological tissue, cryonecrosis is gradually formed which is partially resolved and renewed by healthy tissues, and on the surface of human body it is rejected.

At the present time, cooling agent most commonly used for cryodestruction in medical practice is liquid nitrogen. It is a colorless and odorless liquid of which boiling temperature under atmospheric pressure is –195.81 °C [5, 6].

A variety of instruments, cryogenic plants and cryosurgical systems have been created that run on liquid nitrogen, nitrogen oxide and carbon dioxide. The overwhelming majority of them is cumbersome and requires periodic replacement of containers. Such instruments are characterized by the operating temperature range, time to operating mode, accuracy of temperature control, overall dimensions and continuous work time. Special methods for using such instruments have been developed that allow treatment a wide range of diseases in various areas of medicine (Table 1).

Cryodestruction temperature modes

Temperature reduction on the boundary of pathologic and healthy tissue should take place in the limits minimum required for cryogenic destruction of the entire abnormal focus [5, 19]. The values of temperature for cryogenic destruction of various kinds of tissues vary in the limits:

- 0 °C – brain;
- –20 ÷ –30 °C – skin;
- –50 °C – biological tissue.

Table 1

Areas of cryodestruction application in medical practice

Area of medicine	Domain of usage
Abdominal surgery (abdominal oncology)	• removal of malignant tumors and metastases in liver; • removal of benign and vascular tumors (cysts, adenomas, hemangiomas) in liver; • treatment of parasitic diseases; • treatment of chronic diffuse lesions of liver (hepatitis, cirrhosis); • treatment of acute pseudotumor and chronic pancreatitis; • removal of malignant, mostly unresectable tumors, benign tumors and kidney cysts; • removal of oncopathologies of lung tissues (squamous cell carcinoma of moderate and low differentiation degree, adenocarcinoma of different maturity degree,large cell carcinoma, small cell carcinoma); • lymph node cryodissection and lymph cryoectomy as the mandatory procedure at surgery of neoplasms of internal organs: mammary gland, stomach, liver, pancreatic gland, kidneys, rectum.
Gynecology	• cryodestruction of uterine cervix polyps and sharp-pointed condylomata; • cryodenervation of sacral-uterine ligaments; • laparoscopic ablation of uterine nerves; • therapy of menstrual disorders and premenstrual syndrome.
Dermatology	• removal of warts, skin formations, fibromas, keratoses, hemangiomas, condilomatas, koloids, basaliomas, sarcomas, solar and senile lentigo, birthmarks; • destruction of undesirable masses, including virus warts, dermafibroma, condyloma, molloscum contagiosum, actinic and seborrheic ketatoses; • therapy of seborrheia and acne, psoriasis, eczema, dermatitis, acneiform rash, as well as treatment of other skin defects.
General surgery	• bloodless painless removal of pathologically changed tissues, infiltrations and neoplasms using cryodestruction.
Burn surgery (combustiology)	• destruction of tissues at burns; • therapy of burn shock and pathologic states.
Oncology	• cryodestruction of malignant and benign neoplasms of head and neck; • cryodestruction of malignant, benign and tumor-like lesions of bones; • cryodestruction of mammary tumors; • destruction of skin tumors.
Otolaryngology	• cryosurgery of chronic rhinitis; • cryosurgery of chronic tonsillitis; • cryotherapy of atheromas at suppuration stage; • cryotherapy of papillomas of external ear canal; • cryotherapy of snoring patients with elongated and thickened uvula; • cryotherapy of auricle keloid scars; • cryotherapy of chronic pharyngitis; • cryosurgical therapy of patients with hemangiomas.
Ophthalmology	• removal of basalioma on the internal surface of eyelid; • removal of malignant epithelial tumors of lids of T1-T4 stages, basaliomas, papillomas, conjunctive melanomas.
Phlebology	• removal of varisose veins of lower limbs ("cryostripping").
Neurosurgery	• destructions of deeply seated brain structures, pathways in the central nervous system; • local cooling of certain cerebral cortex areas at epilepsy.

Temperature reduction of biological tissue to (–5 ÷ –10) °C starts the process of crystal formation in the extracellular space, and temperature reduction to (–15 ÷ –20) °C and lower starts the process of ice crystals formation inside the cells, leading to death of biological tissue. It is noteworthy that the mass of ice formed occupies the volume 10 % greater than the volume of liquid the ice crystals are formed of [18, 19, 21]. Maximum damaging effect is achieved on cooling biological tissue to –50 °C, and further temperature reduction does not increase the lethality of cells [5, 6, 18-28].

The intensity of cells destruction in freezing focus depends not only on the minimum temperature in the focus, but also on the biological tissue cooling rate. A relatively fast freezing (40 – 50) °C/min is optimal. The efficiency of cell cryodestruction is high, if it has no time to displace through membranes the intracellular fluid in the process of tissue cooling prior to freezing [18, 19, 22].

A slower freezing (3 – 5 °C/min) is not reasonable, since in this case no processes of intracellular ice formation take place. Also, it is not expedient to use superfast freezing (over 100 °C/min), since in this case amorphous ice is formed that does not damage the structure of biological tissue [18].

Cryodestruction reliability is largely dependent not only on cooling rate, but also on further heating rate, as long as the damaging action of low temperatures arises both in the process cells transformation to ice crystals, and during their thawing to normal temperature. Destruction of cells at thawing is no less intensive than at freezing, since thawing causes ice recrystallization, intensifying the destructive effect on living cells. With a slow heating, interacellular ice crystals go on growing for some time and damaging the intracellular formations. Thawing at a rate of (10 – 12) °C/min assures the most reliable destruction of cells [18-22].

Multiple freezing-thawing allows decreasing the temperature which is lethal for pathological tissue, finding a peculiar kind of compromise between a desire to freeze the neoplastic medium as much as possible and the necessity to preserve healthy surrounding tissues [18-28].

Nitrogen cooling and its disadvantages

Unfortunately, use of liquid nitrogen-based devices does not assure cooling with the necessary accuracy of temperature control. The highest precision of such devices is ±(5 – 10) °C. Moreover, liquid nitrogen is a substance dangerous enough and one must be careful using it. There are risks of overcooling with negative consequences. Also, storage and transportation of liquid nitrogen is problematic, which narrows down potentialities of using liquid nitrogen cooling method.

Thermoelectricity applicability for cryodestruction. Expected advantages

Investigations performed [5-7, 18-28] have confirmed the fact that to achieve the necessary curative effect at low temperatures, there is no need to use very low temperatures to the level of (–150 ÷ –200) °C, typical of liquid nitrogen. One can use much more moderate temperatures about (0 ÷ –50) °C, which opens up the prospects of using thermoelectric cooling down to temperature (0 ÷ -80) °C.

It should be noted that destruction takes place not only on cooling, but also on heating of cooled tissue, which is convenient to be realized by thermoelectric cooling devices via current reversal through them. It creates potential advantage of thermoelectric devices over the nitrogen ones. Destruction efficiency increases essentially during cyclic cooling and heating which is also easily realized by thermoelectric devices.

Existing cryodestruction devices that employ thermoelectric cooling

Recent years have seen rather active use of thermoelectricity in medicine, in particular, in cryodestruction. A variety of thermoelectric medical devices has been developed that include thermoelectric devices and cryoextractors for cooling biological tissue, destruction of malignant tumors, that are used in various cryosurgical operations in ophthalmology, gynecology, urology, otolaryngology, etc.

To reduce blood loss and pain syndrome during surgical operations, thermoelectrically cooled surgical instruments shaped as lancets are used [29-32] (Fig. 1).

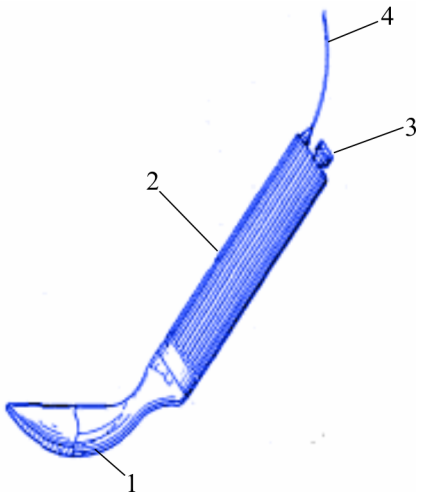

Fig. 1. Cold lancet. 1 – thermocouple unit; 2 – case; 3 – coolant container; 4 – electric cable.

During recent years, in the Institute of Thermoelectricity of the National Academy of Sciences and Ministry of Education and Science of Ukraine research on the use of thermoelectric cooling in medicine has been pursued [33]. Samples of medical equipment for cryodestruction, such as thermoelectric cryoextractor (Fig. 2) [34], thermoelectric hypotherm for oncology (Fig. 3) [35, 36] have been created. Wide application has been found by thermoelectric devices for the destruction of soft tissues (cryoprobes and cryoextractors) (Fig. 4) intended for therapy of oncologic diseases, removal of malignant neoplasms and arrest of propagation of metastases [37-43].

Fig. 2. Thermoelectric cryoextractor.

Fig. 3. Thermoelectric hypotherm for oncology.

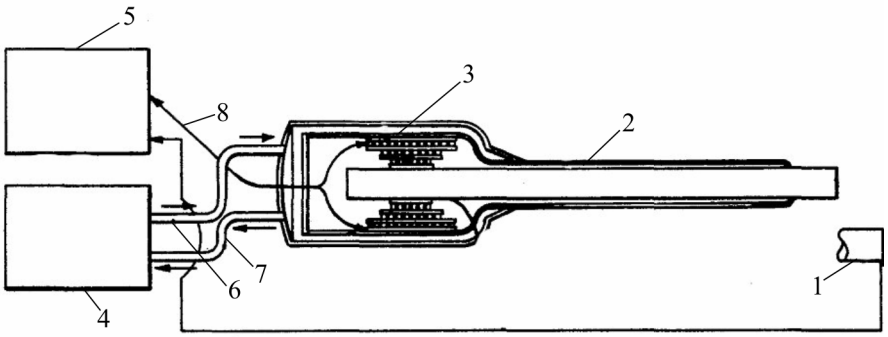

Fig. 4. Thermoelectric cryoprobe. 1 – disposable tip; 2 – heat pipe; 3 – thermoelectric modules; 4 – heat exchanger; 5 – control unit; 6, 7 – liquid coolant circulating tubes; 8 – control unit connection to thermoelectric modules.

There is also a good outlook for using cooling thermoelectric devices in dermatology and cosmetology. Such devices allow treatment of skin diseases and cryodestruction for the purpose of removing papillomas, condylomata, warts, hemangiomas, pigmental and vascular nevi, hypertrophic scars. When used in cosmetology, such devices offer the advantage of a good cosmetic effect, since their application leaves no scars, unlike surgical intervention [44-49].

Conclusions

1. It is established that liquid nitrogen is in most common use for cryodestruction. For implementation of cryodestruction about 40 such devices have been created.
2. From the practice of using cryodestruction it is found that the temperature of –50 °C is optimal for the destruction of biological tissue. In so doing, cooling rate must be in the range of – (40 – 50) °C/min. Destruction efficiency increases with cyclic cooling and heating.
3. For the implementation of optimal cryodestruction conditions thermoelectric cooling offers a number of advantages over nitrogen cooling. The existing thermoelectric devices for cryodestruction confirm their efficient use in medicine.

References

1. E.A. Kolenko, *Thermoelectric Cooling Devices, 2nd ed.* (Leningrad: Nauka, 1967), 283 p.
2. L.I. Anatychuk, *Thermoelements and Thermoelectric Devices: Handbook* (Kyiv: Naukova Dumka, 1979), 768 p.
3. V. Denkov, *On the Edge of Life*, Transl. from Bulgarian by I.M. Saburova (Moscow: Znaniye,1988), 192 p.
4. S. Maruyama, K. Nakagawa, and H. Takeda, The Flexible Cryoprobe Using Peltier Effect for Heat Transfer Control, *Journal of Biomechanical Science and Engineering* **3** (**2**), 138 – 150 (2008).
5. V.I. Kochenov, *Cryosurgical Preventive Oncology* (Nizhniy Novgorod, 2000), 56 p.
6. V.I. Kochenov, *Cryological Preventive Oncology: Concise Study Guide for Doctors and Students*, 2nd revised ed. (Nizhniy Novgorod, 2003), 92p.
7. V.I. Kochenov, Adhesive Effect in Cryosurgery, *International Abstract Journa*l **8**, IV (1982).
8. S.A. Vasilyev, S.B. Pesnya-Prasolov, Use of Cryosurgical Method in Neurosurgery, *Neurosurgery* **4**, 63 – 70 (2009).
9. A.N. Zinkin, N.G. Zingilevskaya, and B.B. Muselyan, *Cryotherapy in Otholaryngology*

(Guidelines) (Krasnodar, 1997), p. 16.
10. V.V. Shafranov, E.N. Borkhunova, M.A. Kostylev, D.I. Tsyganov, A.M. Torba, A.V. Taganov, L.P. Mezhov, Z.V. Kalmykova, Mechanism of Destruction of Biological Tissues at Local Cryodestruction, *Herald of the Russian Academy of Natural Sciences* **1**, 68 – 77 (2012).
11. B.I. Kalperovich, T.B. Komkova, N.V. Merzlikin, et al., *Fundamentals of Liver and Pancreatic Gland Cryosurgery* (Tomsk: Pechatnaya Manufactura Publ., 2006), 232 p.
12. S.A. Shalimov, et al. Cryosurgical Methods for Treatment of Inoperable Tumors of Abdominal Cavity, *Zdorovye Ukrainy* (newspaper), **74** (2003).
13. E.I. Kandel, *Cryosurgery* (Moscow: Medicine, 1974), p. 303.
14. K.C. Xu, Nikolai Korpar, and L.Z. Niu, *Modern Cryosurgery for Cancer* (World Scientific Publisher, 2012).
15. V.V. Budrik, *Physical Fundamentals of Cryomethods in Medicine, Training Manual*, Transl. from Russian (2010), 140 p.
16. S.M. Cooper, The History of Cryosurgery, *J. R. Soc. Med*. **94**, 196 – 201 (2001).
17. D.K. Whittaker, Mechanisms of Tissue Destruction Following Cryosurgery, *Annals of the Royal College of Surgeons of England* **66**, 313 – 318 (1984).
18. W. Yiu, M.T. Basco, J.E. Aruny, and B.E. Sumpio, Cryosurgery: A review, *Int. J. Angiol*. **16** (1), 1 – 6 (2007).
19. T.A. Ismailov, Use of Semiconductor Thermoelectric Modules for Local Effect on Individual Parts of Human Organism, *Interacademic Collection of Articles* (Makhachkala: Dagestan State Medical Institute, 1991), p. 8 – 12.
20. A.I. Paches, V.V. Shental, P.T. Ptukha, et al., *Cryogenic Method for Treatment of Head and Neck Tumors* (Moscow, 1978), p. 168.
21. V.Yu. Shakhov, On the Most Rational Methods for Cryodestruction of Malignant Neoplasms, *Voprosy Onkologii* **9**, 31 – 37 (1983).
22. V.I. Kochenov, Yu.V. Korolev, Simplest Cryoinstruments for Clinical Practice of Cryologist, *Medical Cryology*, Issue 4 (Nizhniy Novgorod, 2003), p. 157 – 160.
23. I.I. Potapov, et al. *Cryosurgery in Otolaryngology* (Moscow: 1975).
24. V.D. Dragomiretskii, Cryosurgicaql Methods for Treatment of Ear, Nose and Throat Diseases, *Practical Cryomedicine*, Ed. by V.I. Grischenko and B.P. Sandomirskii (Kyiv: Zdorovye, 1987), p. 91 – 118.
25. N.I. Nikolayev, V.I. Kochenov, S.N. Tsybusov, et al., Use of Regeneration Effects of Cryotreatment in Surgery and Plastics of Drum Membrane, *Medical Cryology*, Issue 4 (Nizhniy Novgorod, 2003), p. 176 – 188.
26. B.I. Alperovich, L.M. Paramonova, and N.V. Merzlikin, *Cryosurgery of Liver and Pancreatic Gland* (Tomsk, 1985).
27. B.I. Verkin, V.I. Grischenko, B.N. Murinets-Markevich, L.M. Lyashevich, and O.A. Grishina, Cryogenic Equipment in Gynecological Practice, *Biomedical Engineering* **2** (1978).
28. V.I. Grischenko, *Gypothermia and Cryosurgery in Obstetrics and Gynecology* (Moscow: Medicine, 1974).
29. Max L. Hirschhorn, *Patent US 3093135*, Cooled Surgical Instrument (1963).
30. Max L. Hirschhorn, *Patent US 3502080*, Thermoelectrically Cooled Surgical Instrument (1970).
31. Baumgarten Frederic, *Patent FR 2613611(A1),* Thermoelectric Effect Device and its Control and Regulating Members for Treating Cancers and other Tumours by the Method of Iterative Cryogenic Applications (1988).

32. Eidus William, *Patent US 3133539*, Thermoelectric Medical Instrument (1964).
33. L.I. Anatychuk, Current Status and Some Prospects of Thermoelectricity, *Journal of Thermoelectricity* **2**, 7 – 20 (2007).
34. L.Ya. Kushneryk, Yu.R. Starodub, *Patent UA 53914*, Thermoelectric Cryoextractor (2003).
35. L.Ya. Kushneryk, R.V. Senyutovych, A.E. Ivansky, Thermoelectric Instrument for Surgery of Oncodiseases, *Journal of Thermoelectricity* **2**, 78 – 82 (2003).
36. L.I. Anatychuk, O.J. Luste, L.Ya. Kushneryk, Computer Control of Temperature Distribution in Tissues at Cryosurgery and Cryotherapy, *Journal of Thermoelectricity* **4**, 75 – 79 (2006).
37. L.I. Anatychuk, L.Ya. Kushneryk, R.V. Senyutovich, *Patent UA 84970*, Thermoelectric Hypotherm for Proctology and Oncology (2008).
38. Archie C. Hamilton, *Patent US 5207674*, Electronic Cryogenic Surgical Probe Apparatus and Method (1993).
39. Wayne F. Lisenbee, *Patent US 3993075*, Disposable, Defrostable Cryosurgical Probe Surfaces (1976).
40. Timofei S. Gudkin, *Patent US 4519389*, Thermoelectric Cryoprobe (1985).
41. Yehoshua B. Nun, *Patent US 6623479*, Cryosurgical Instrument (2003).
42. Michael Haas, *Patent US 6629417*, Hand-Held Heat Sink Cryoprobe, System for Heat Extraction Thereof, and Method Therefore (2003).
43. Yu.V. Korolev, *Patent RU 2293538*, Cryogenic Apparatus (2007).
44. M. Elfving, *Patent US 3088288*, Thermoelectric Refrigeration System (1960).
45. M.R. Holman, S.J. Rowland, Design and Development of a New Cryosurgical Instrument Utilizing the Peltier Thermoelectric Effect, *J Med Eng Technol*., 1997.
46. H. Takeda, S. Maruyama, and J. Okajima, Development and Estimation of a Novel Cryoprobe Utilizing the Peltier Effect for Precise and Safe Cryosurgery, *Cryobiology*, 2009.
47. B. Hantash, B. Renton, and R. Berkowitz, Pilot Clinical Study of a Novel Minimally Invasive Bipolar Microneedle Radiofrequency Device, *Laser Surg. Med*, 2009.
48. Stephen J. Rowland, *Patent US 6096032*, Medical Cryo-Surgical Device (2000).
49. L.I. Anatychuk, R.R. Kobylianskyi, Yu.M. Mocherniuk, Thermoelectric Device for Skin Treatment, *Journal of Thermoelectricity* **4**, 86 – 92 (2009).

Submitted 20.12.2013.

NEWS

INTERNATIONAL THERMOELECTRIC ACADEMY

JEFF SNYDER

(DEDICATED TO 45-th ANNIVERSARY)

On December 27, 2013 Dr. Jeff Snyder, a well-known specialist in thermoelectric materials and devices, academician and vice-president of the International Thermoelectric Academy, celebrated his 45-th jubilee.

Jeff Snyder received his B.S. in physics, chemistry and mathematics at Cornell University and his Ph.D in applied physics from Stanford University (1997) where he was a Hertz Fellow.

Jeff Snyder's scientific interests include colossal magnetoresistance materials and metallic ferromagnets which involved thin film deposition, and design, automation and analysis of electronic and magnetic measurements. At the Max Planck Institut für Festkörperforschung, Stuttgart, Germany (1992 – 93) he studied intermetallic, sub-nitride and C_{60} intercalation solid state chemistry. At Cornell University (1990 – 91) he studied chalcogenides.

He was a senior member of the technical staff at the Jet Propulsion Laboratory, California Institute of Technology, for 9 years (1997 – 2006).

Since joining JPL in 1997, Dr. Snyder has been investigating novel thermoelectric materials focusing recently on complex Zintl phases and nanometer scale structures. He has developed the concept of thermoelectric compatibility for design and optimization of segmented generators, and he has developed empirical and analytical models for calculating thermoelectric performance. He is especially interested in thermoelectric properties of materials above room temperature. The scientist has developed capabilities for measurements of Seebeck coefficient (thermoelectric power), electrical resistivity, Hall effect, thermal diffusivity and thermal conductivity up to 1000 degrees C.

Using electrochemistry and low-cost microfabrication techniques, he has developed the fabrication process and testing of thermoelectric microdevices. He has also designed and tested portable power sources for terrestrial and space applications.

Dr. Snyder's current teaching as well as research focuses on thermoelectric materials and devices. He has participated in several short courses teaching the engineering, chemistry and physics of thermal and electrical transport of thermoelectrics and has been lecturer for a similar course at California State Polytechnic University (Pomona).

International Thermoelectric Academy, Institute of Thermoelectricity of the National Academy of Sciences and Ministry of Education and Science of Ukraine, "Journal of Thermoelectricity" Publishers cordially congratulate the respected Jeff Snyder on his jubilee and wish him sound health, creative inspiration, happiness and new advances in science.

RAYMOND MARLOW

On October 11, 2013, after a short severe illness, Raymond Marlow, the founder of Marlow Industries, a famous company in thermoelectricity, passed away.

Raymond Marlow was born on September 24, 1931 in Waco, Texas. He graduated from Waco High School and studied mechanical engineering at Texas A&M University. After graduation, he moved to Pirmasens, Germany, where he fulfilled his military duty in the Gun Battalion. Upon returning to the United States, he obtained a Master in Mechanical Engineering at the University of Texas and went to work for Chance Vought aviation company, and then for Texas Instruments (1957), where he was involved in a new semiconductor technology known as thermoelectric cooling.

When Texas Instruments decided to exit the thermoelectric business, Raymond Marlow acquired Texas Instruments' interest and started his first company, International Energy Conversion. Later this company merged with two other companies to become Nuclear Systems.

Marlow Industries was established by Raymond Marlow in 1973.

In 1991 Raymond Marlow and his employees won the Malcolm Baldrige National Quality Award. According to Industry Week Magazine, Marlow Industries entered the list of "America's 10 Best Plants" in 1993 and "Top 25 Growing Companies" in 1999.

Raymond Marlow's professional achievements include receiving the Dallas Fort Worth Region 1992 Ernst & Young Entrepreneur of the Year in Technology Award. At Texas A&M University he was recognized as a Distinguished Graduate of the Mechanical Engineering School and was awarded the Dwight Look College Outstanding Alumni Award.

The name of Raymond Marlow will remain in the memory of his friends and colleagues forever.

ARTICLE PREPARATION RULES

The article shall conform to the journal profile. The article content shall be legible, concise and have no repetitions.

The article shall be submitted to the editorial board in electronic version.

The text shall be typed in text editor not lower than MS Word 6.0/7.0.

Page setup: "mirror margins"- top margin – 2.5 cm, bottom margin – 2.0 cm, inside – 2.0 cm, outside– 3.0 cm, from the edge to page header – 1.27 cm, page footer – 1.27 cm.

Graphic materials, pictures shall be submitted in color or, as an exception, black and white, in .opj or .cdr formats, .jpg or .tif formats being also permissible. According to author's choice, the tables and partially the text can be also in color.

The article shall be submitted in English on A4 paper sheets; the number of pages shall not exceed 12. By agreement with the editorial board, the number of pages can be increased.

To accelerate publication of the article, please adhere to the following rules:

- the authors' initials and names are arranged in the centre of the first page at the distance of 1 cm from the page header, font Times New Roman, size 12 pt, line spacing 1.2;
- the name of organization, address (street, city, postal code, country) – indent 1 cm below the authors' initials and names, font Times New Roman, size 11 pt, line spacing 1.2, center alignment;
- the title of the article is arranged 1 cm below the name of organization, in capital letters, semi-bold, font New Roman, size 12 pt, line spacing 1.2, center alignment. The title of the article shall be concrete and possibly concise;
- the abstract is arranged 1 cm below the title of the article, font Times New Roman, size 10 pt, in italics, line spacing 1.2 ,center alignment;
- key words are arranged below the abstract, font Times New Roman, size 10 pt, line spacing 1.2, justified alignment. The title "Key words" – font Times New Roman, size 10 pt, semi-bold;
- the main text of the article is arranged 1 cm below the abstract, indent 1 cm, font Times New Roman. size 11 pt, line spacing 1.2, justified alignment;
- formulae are typed in formula editor, fonts Symbol, Times New Roman. Font size is "normal" – 12 pt, "large index" – 7 pt, "small index" – 5 pt, "large symbol" – 18 pt, "small symbol" – 12 pt). The formula is arranged in the text, centre aligned and shall not occupy more than 5/6 of the line width, formulae are numbered in round brackets right;
- dimensions of all quantities used in the article are represented in the International System of Units (SI) with the explication of the symbols employed;
- figures are arranged in the text. The figures and pictures shall be clear and contrast; the plot axes – parallel to sheet edges, thus eliminating possible displacement of angles in scaling;
- tables are arranged in the text. The width of the table shall be 1 cm less than the line width. Above the table its ordinary number is indicated, right alignment. Continuous table numbering throughout the text. The title of the table is arranged below its number, center alignment;
- references should appear at the end of the manuscript. References within the text should be enclosed in square brackets. References should be numbered in order of first appearance in the text. Examples of various reference types are given below.

– L.I. Anatychuk, *Thermoelements and Thermoelectric Devices: Handbook* (Kyiv: Naukova Dumka, 1979), p.766. (Book)
– T.M. Tritt, Thermoelectric Phenomena, Materials, and Applications, *Annual Review of Materials Research* **41**, 433 (2011). (Journal paper)
– U. Ghoshal, *Proceedings of the XXI International Conference on Thermoelectrics* (N.Y., USA, 2002), p. 540. (Proceedings Conference)

The article should be supplemented by:

• letter from the organization where the work was performed or from the authors of the work applying for the publication of the article;

• information on the author (authors): last name and initials; full name and postal address of the institution where the author works; academic degree; position; telephone number; E-mail;

• author's (authors') photo in color or, as an exception, in black and white. With the number of authors more than two their photos are not given;

• author's application to the following effect:

We, the undersigned authors, … transfer to the founders and editors of "Journal of Thermoelectricity" the right to publish the article…in Ukrainian, Russian and English. This is to confirm that the present publication does not violate the copyright of other persons or organizations.

Date Signatures

Below is given an example of article preparation.

Author's photo 3 × 4 cm

A.I. Casian[1], B.M. Gorelov[2]

[1]Technical University of Moldova,
168, Stefan cel Mare Ave.,
Chisinau, MD-2004, Moldova;
[2]Institute of Surface Chemistry of National Academy
of Sciences of Ukraine, 17, Gen. Naumov Str.,
Kyiv, 03164, Ukraine

Author's photo 3 × 4 cm

STATE OF THE ART AND PROSPECTS OF THERMOELECTRICITY ON ORGANIC MATERIALS

The aim of the paper is to analyze the expected thermoelectric opportunities of organic materials, including some highly conducting quasi-one-dimensional crystals. It is shown that interest of investigators in these materials has been growing recently. Quasi-one-dimensional organic crystals have high prospects for thermoelectric applications. These materials combine the properties of multi-component systems with more diverse internal interactions and of quasi-one-dimensional quantum wires with increased density of electronic states. It is shown that the values of the thermoelectric figure of merit ZT ~ 1.3 – 1.6 at room temperature are expected in really existing organic crystals of tetrathiotetracene-iodide, TTT_2I_3, if the crystal parameters are approaching the optimal ones.

Key words: thermoelectricity, tetrathiotetracene-iodide, polarizability.

Introduction

It is known that conducting organic materials usually have much lower thermal conductivity than the inorganic materials. Moreover, the organic materials can be fabricated by simpler chemical methods, and it is expected that such materials will be less expensive in comparison with the inorganic ones. Exactly these properties attracted attention to such materials for the use in thermoelectric (TE) applications long time ago [1, 2]. In spite of relatively high value of the thermoelectric figure of merit $ZT = 0.15$ at room temperature observed in polycopper phthalocyanine [2] as early as 1980, the thermoelectric properties of organic materials are still weakly investigated. This situation has the only explanation that thermoelectricians are still weakly interested in organic materials, and organic chemists are also weakly interested in thermoelectric materials. Moreover, in order to seek good organic thermoelectrics, it is necessary to organize multidisciplinary consortiums of physicists, organic chemists and engineers in the field of thermoelectricity. …

The aim of this paper is to present briefly the state-of-the-art of investigations in the area of new organic thermoelectric materials and to describe the nearest expected results for really existing quasi-one-dimensional organic crystals of tetrathiotetracene-iodide, TTT_2I_3.

Quasi-one-dimensional organic crystals of TTT_2I_3

The structure of quasi-one-dimensional organic crystals of tetrathiotetracene-iodide, TTT_2I_3, has been briefly described in [34]. These needle-like crystals are formed of segregate chains or stacks of planar molecules of tetrathiotetracene *TTT*, and iodine ions. The chemical compound TTT_2I_3 is of mixed-valence: two molecules of *TTT* give one electron to the iodine chain which is formed from I_3^- ions. The

conductivity of iodine chains is negligibly small, so that only *TTT* chains are electrically conductive and holes serve as carriers. The electrical conductivity σ along *TTT* chains at room temperature varies between 10^3 and $10^4\ \Omega^{-1}\text{cm}^{-1}$ for crystals grown by gas phase method [35], and between 800 and $1800\ \Omega^{-1}\text{cm}^{-1}$ for crystals grown from solution [36]. Thus, the conductivity is very sensitive to crystal impurity and perfection which depends on growth method. In the direction perpendicular to chains σ is by three orders of magnitude smaller than in the longitudinal direction and is neglected. …

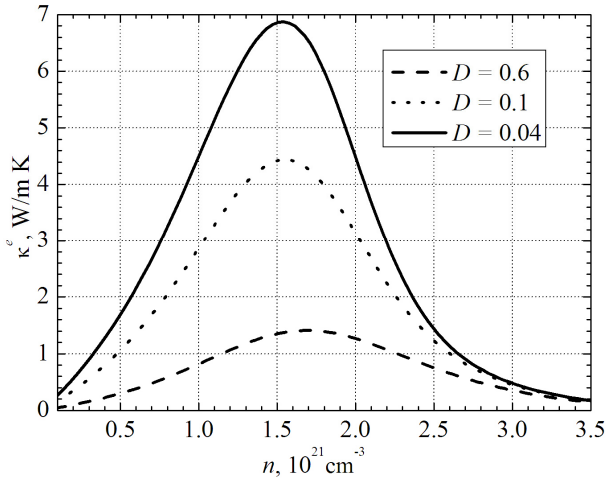

Fig. 1. Dependences of electron thermal conductivity κ^e on n.

$$\sigma = R_0,\ S = R_1 / eTR_0,\ \kappa^e = \left(e^2T\right)^{-1}\left(R_2 - R_1^2 / R_0\right), \tag{1}$$

Thermoelectric properties

Expressions (2) – (3) have been calculated in order to determine the thermoelectric properties of quasi-one-dimensional organic crystals of TTT_2I_3 with different degrees of purity….

Conclusions

The state-of-the-art of research on new organic materials for thermoelectric applications is analyzed. It is shown that the interest of investigators in these materials has been growing in recent years. The highest value of $ZT \sim 0.38$ at room temperature has been measured in doped acetylene, with the only problem that this material is not stable. Accurate control of the oxidation level in poly (3, 4-ethylenedioxythiophene) (PEDOT) gave the power factor $324\ \mu\text{W}\cdot\text{m}^{-1}\text{K}^{-2}$ and in combination with its low intrinsic thermal conductivity ($\kappa = 0.37\ \text{W}\cdot\text{m}^{-1}\text{K}^{-1}$) yielded $ZT = 0.25$ at room temperature, and this material is air-stable….

References

1. Ali Shakouri, Recent Developments in Semiconductor Thermoelectric Physics and Materials, *Annu.Rev.Mater.Res*.**41**, 399-431 (2011).
2. L.I. Anatychuk, *Thermoelectricity, Vol.2, Thermoelectric Power Converters* (Kyiv, Chernivtsi: Institute of Thermoelectricity, 2003), 376p.
3. M.E. Bengen, *German Patent Appl*. OZ 123, 438, 1940; *German Patent* 869,070, 1953, Tech. Oil Mission Reel, 143,135, 1946.